

Durham E-Theses

Enhanced Lifetime of Organic Photovoltaics based on P3HT: PCBM

AL-BUSAIDI, ZAKIYA,NASSER,KHALFAN

How to cite:

AL-BUSAIDI, ZAKIYA,NASSER,KHALFAN (2017) *Enhanced Lifetime of Organic Photovoltaics based on P3HT: PCBM* , Durham theses, Durham University. Available at Durham E-Theses Online:
<http://etheses.dur.ac.uk/12435/>

Use policy



This work is licensed under a [Creative Commons Attribution No Derivatives 3.0 \(CC BY-ND\)](https://creativecommons.org/licenses/by-nd/3.0/)



**Enhanced Lifetime of Organic
Photovoltaics based on
P3HT: PCBM**

Zakiya Nasser AL-Busaidi

Ustinov College

A Thesis presented for the degree of
Doctor of Philosophy

Centre for Molecular and Nanoscale Electronics

Department of Engineering

Durham University

August 2017

ABSTRACT

Enhanced Lifetime of Organic Photovoltaics based on P3HT: PCBM

Zakiya AL-Busaidi

The short lifetime of organic photovoltaics (OPVs) is a key factor that limits the commercialization of this flexible, low-cost PV technology. The sensitivity of OPVs to water and oxygen in the ambient environment has been found to be the major reason for their degradation. Therefore, techniques to protect the devices from water and oxygen are needed. This thesis introduces new methods designed to reduce the impact of water and oxygen on the lifetime of OPV devices.

Two different methods were developed, both using insulating polymers. The first was the addition of an insulating polymer, such as poly (methyl methacrylate) (PMMA), or poly (ethylene glycol) (PEG), to a poly (3-hexylthiophene): [6, 6]-phenyl-C₆₁-butyric acid methyl ester (P3HT: PCBM) OPV blend (ternary approach). It was found that this technique increased the lifetime of the OPVs, due to the ability of the insulating polymers to work as gettering agents for water.

The second method that was used is laminating OPVs with an insulating polymer. It was found that this lamination technique enhanced the device lifetime more than the ternary approach due to the creation of a barrier to the ingress of both oxygen and water.

TABLE OF CONTENTS

ABSTRACT	I
TABLE OF CONTENTS	II
LIST OF FIGURES	IX
LIST OF TABLES.....	XIX
DECLARATION	XXI
STATEMENT OF COPYRIGHT.....	XXII
PUBLICATIONS	XXIII
ACKNOWLEDGEMENTS.....	XXV
DEDICATION	XXVII
1. INTRODUCTION, OBJECTIVE AND ORGANIZATION.....	1
1.1.....Introduction	
.....	1
1.2 Thesis Objective.....	3
1.3 Thesis Organization	3
1.3 References	7
2. BACKGROUND	9
2.1 Introduction	9
2.2 The history of photovoltaic technology	10
2.2.1 First generation PV technology	10
2.2.2 Second generation PV technology	11

2.2.3	Third generation PV technology	12
2.3	Why organic photovoltaics?	13
2.4	Organic semiconductors	14
2.5	Energy conversion in photovoltaic technologies	16
2.6	Operating principles of OPVs	17
2.7	Device architectures	19
2.7.1	Single layer OPVs	19
2.7.2	Bilayer OPV.....	20
2.7.3	Bulk heterojunction OPV BHJ.....	21
2.8	Electrical characterization of OPVs	22
2.8.1	Short-circuit current	23
2.8.2	Open-circuit voltage.....	23
2.8.3	Fill Factor	24
2.8.4	Power conversion efficiency	25
2.9	Recombination mechanisms in OPVs	26
2.9.1	Geminate recombination.....	26
2.9.2	Non-geminate recombination	27
2.10	Device lifetime	32
2.11	References	33
3.	DEGRADATION OF ORGANIC PHOTOVOLTAICS	44
3.1	Introduction	44
3.2	Oxygen-induced degradation	45

3.3	Water-induced degradation.....	49
3.4	Light-induced degradation	53
3.5	Degradation induced by diffusion of metal electrodes.....	56
3.6	Metastable morphology induced degradation	60
3.7	Degradation mechanisms in P3HT: PCBM	62
3.7.1	Photochemical mechanisms in P3HT.....	62
3.7.2	Photochemical degradation of PCBM.....	65
3.8	Conclusion.....	66
3.8	References	68
4.	EXPERIMENTAL TECHNIQUES	76
4.1	Introduction.....	76
4.2	Materials and device structure	76
4.2.1	Active layer	77
4.2.2	Insulating polymers	79
4.2.3	Electrodes	82
4.2.4	The interfacial layer	82
4.3	Deposition techniques.....	83
4.3.1	Thermal evaporation	84
4.3.2	Spin coating.....	85
4.4	Fabrication process.....	86
4.4.1	Substrate preparation	87
4.4.2	PEDOT: PSS layer.....	87

4.4.3 Blend solution	88
4.4.4 Active layer	88
4.4.5 Al evaporation.....	89
4.4.6 Lamination process.....	89
4.5 Device Characterization.....	90
4.5.1 Current-voltage characteristics.....	90
4.5.2 Space charge limited current for hole mobility measurements	93
4.5.3 Ultraviolet-visible spectroscopy	94
4.5.4 Atomic force microscopy.....	96
4.5.5 Fourier transform infrared spectroscopy	101
4.5.6 Scanning electron microscopy	102
4.6 Lifetime measurements.....	103
4.7 Aging test environment.....	103
4.8 References	107
5. THE DEGRADATION OF P3HT: PCBM DEVICES STORED UNDER DIFFERENT ATMOSPHERIC CONDITIONS	114
5.1 Introduction	114
5.2 The effect of ambient environment on the device lifetime	114
5.3 Degradation of standard devices in different environments	116
5.3.1 Variation in lifetime of standard devices	116
5.3.2 Changes in electrical parameters	117

5.3.3 UV-vis absorption	119
5.4 Fourier transform infrared spectroscopy	120
5.4.1 FTIR spectra of as – deposited P3HT: PCBM	120
5.4.2 FTIR spectra of degraded P3HT: PCBM	122
5.5 Conclusion.....	125
5.6 References	126
6. TERNARY OPVs BASED ON P3HT: PCBM: PMMA	128
6.1 Introduction	128
6.2 Effect of PMMA on the performance of P3HT: PCBM devices	129
6.2.1 Electrical characteristics of ternary devices	130
6.2.2 The morphology of ternary blend films	133
6.2.3 Phase separation in ternary blend film.....	136
6.2.4 Absorption spectra of P3HT: PCBM: PMMA	139
6.3 The effect of PMMA on the lifetime of P3HT: PCBM devices	140
6.3.1 Lifetime measurements	141
6.3.2 Electrical Characteristics.....	143
6.3.3 UV-Vis absorption.....	146
6.3.4 C-AFM of binary and ternary blend films.....	148
6.4 Conclusion.....	153
6.5 References	155
7. TERNARY OPVs USING OTHER INSULATING POLYMERS	159
7.1 Introduction	159

7.2	The degradation of ternary devices incorporating a-PS.....	159
7.3	The degradation of ternary devices incorporating PEG.....	161
7.4	Comparison between ternary devices incorporating PMMA, PS, and PEG.....	163
7.5	The performance of ternary devices incorporating PEG.....	164
7.6	UV-vis absorption spectra of P3HT: PCBM: PEG.....	165
7.7	Morphology of ternary blend film incorporating PEG.....	165
7.8	Proposed morphology of ternary blend films incorporating PEG .	170
7.9	Degradation of multilayer devices.....	172
7.9.1	Lifetime measurements	174
7.9.2	Film morphology of multilayer devices.....	176
7.10	Degradation of ternary devices using nitrobenzene as a solvent for PEG.....	177
7.10.1	Lifetime measurements	178
7.10.2	Film morphology.....	179
7.11	Conclusion.....	180
7.12	References	181
8.	PRELIMINARY INVESTIGATION IN THE HOLE TRANSPORT IN BINARY AND TERNARY DEVICES.....	182
8.1	Introduction	182
8.2	Space charge limited current in hole-only devices.....	183
8.3	Conductivity in binary and ternary devices at different humidity levels	186

8.4 Hole mobility in binary and ternary devices with fixed film thickness	188
8.5 The effect of the environment	191
8.6 The effect of the metal contact on the hole current	194
8.6 Conclusion	196
8.7 References	197
9. OPVs LAMINATED WITH INSULATING POLYMERS	200
9.1 Introduction	200
9.2 The effect of the lamination process on device performance	201
9.3 Film morphology of the cathode	204
9.4 Effect of lamination on device lifetime	206
9.5 Comparison between ternary blend and laminated devices	207
9.6 The effect of humidity on the electrical parameters of the ternary and laminated devices	209
9.7 The effect of humidity on the cathode	211
9.8 Conclusion	214
9.9 References	216
10. CONCLUSIONS AND SUGGESTIONS FOR FURTHER WORK	218
10.1 Conclusions	218
10.2 Suggestions for further work	221
10.3 References	223

LIST OF FIGURES

Figure 2.1	(a) The chemical structure of the simplest conjugated organic material: ethylene, (b) σ and π bonds of ethylene, and (c) Formation of HOMO and LUMO orbitals in ethylene. Redrawn from [15].	15
Figure 2.2	The energy level diagram for a p-n junction photodiode. Redrawn from [20].	17
Figure 2.3	Working mechanisms of OPVs. Redrawn from [8].	18
Figure 2.4	Schematic illustration of different OPV architectures a) single layer, b) bilayer and c) bulk heterojunction (BHJ). Purple lines represent electron-donor organic material and orange circles represent electron-acceptor organic material.	19
Figure 2.5	J-V characteristics of an OPV device under illumination (red) and in the dark (blue).	22
Figure 2.6	Energy diagram of a P3HT-PCBM solar cell [42][43].	24
Figure 2.7	Different recombination mechanisms in OPVs. The exciton formed after light absorption (gray arrow). The geminate mechanisms: (a) exciton decay after excitation, (b) recombination at the D/A interface through the charge transfer state (CT). Nongeminate mechanisms: (c) band to band recombination, (d) trap-assisted recombination.	27
Figure 3.1	Different factors that cause degradation in an OPV device.	45
Figure 3.2	The mechanism for the formation of singlet oxygen.	48
Figure 3.3	Schematic diagram illustrating the different pathways for the ingress of oxygen and water molecules into an OPV device.	51

Figure 3.4	Schematic diagram showing metal diffusion and its impact on the active layer.	58
Figure 4.1	Schematic structure of devices based on (a) a binary blend film, (b) a ternary blend film.....	77
Figure 4.2	Chemical structures of P3HT (left) and PCBM (right).	78
Figure 4.3	Energy level diagram showing the component in a standard device. Ref [7][8][9][10].	79
Figure 4.4	Chemical structures of the different insulating polymers used in this study.	80
Figure 4.5	The chemical structure of PEDOT: PSS. The dots linking the SO ₃ and thiophene rings represent ionic bonds resulting in a complex structure of PEDOT with PSS.	83
Figure 4.6	Schematic diagram of a thermal evaporation system.	84
Figure 4.7	Schematic diagram showing the spin coating process.....	85
Figure 4.8	Fabrication of an OPV device.....	87
Figure 4.9	The test chamber.	91
Figure 4.10	J-V curve in the dark for a standard device (P3HT: PCBM).	92
Figure 4.11	Schematic diagram of a hole-only device based on P3HT: PCBM. Ref [8][9][33].....	93
Figure 4.12	Typical absorption spectrum of a P3HT: PCBM blend film... ..	95
Figure 4.13	Schematic diagram of a spectrophotometer.	96
Figure 4.14	Schematic diagram showing the basic components of an AFM system.....	97
Figure 4.15	C-AFM image of a ternary blend film showing the effect of repeated rescanning on the image quality.	100

Figure 4.16 Schematic diagram showing the basic components of an FTIR instrument. Redrawn from [41].	101
Figure 4.17 Low humidity environment in the desiccator.	105
Figure 5.1 J-V curves, under illumination, for devices stored in laboratory conditions (black squares) and a controlled environment (red circles). Closed symbols represent the initial measurements, and open symbols represent devices after aging for 96 h.	115
Figure 5.2 J-V curves, under illumination, for devices stored in an ambient environment (black squares) and an inert environment (red circles). Closed symbols represent the initial measurements, and open symbols after aging for 190 hours.	118
Figure 5.3 UV-vis absorption spectra for standard devices stored in an ambient environment (black squares), and in an inert environment (red circles). Closed symbols represent the spectra as-deposited and open symbols after aging for 192 h.	119
Figure 5.4 FTIR spectrum for an as-deposited film of P3HT: PCBM.	120
Figure 5.5 FTIR spectra of a P3HT: PCBM film stored in an ambient environment. (a) full range of measurement and the expanded regions of: (b) aromatic groups, (c) thiophene rings, and (d) alkyl groups. The black line represents the spectra as deposited, and the red line was recorded after 840 h.	123

Figure 6.1	J-V curves under illumination for devices with different PMMA content.	130
Figure 6.2	Dark J-V curves for a binary device, P3HT: PCBM (50:50), (black line), and a ternary device, 86 wt% (50:50 P3HT: PCBM):14 wt% PMMA (red dashed line).	132
Figure 6.3	AFM topography images of P3HT: PCBM: PMMA ternary films with different percentage by mass of PMMA (a) 0 wt%, (b) 2 wt%, (c) 5 wt%, (d) 8 wt%, (e) 10 wt%, (f) 14 wt%, and (g) 16 wt%.	134
Figure 6.4	(a) Typical profiles for islands chosen from films containing 5 wt% (red), and 14 wt% of PMMA (black); (b) the surface area of the islands as a function of PMMA content (black).	135
Figure 6.5	AFM topography images of a P3HT: PCBM: PMMA film taken from (a) front (b) back.	137
Figure 6.6	Cross-section SEM image of 86 wt% (50: 50 P3HT: PCBM) :14 wt% PMMA blend film.	138
Figure 6.7	Schematic diagram of the morphology of a ternary film.	138
Figure 6.8	UV-vis absorption spectra of ternary blend films (a) containing different amounts of PMMA, (b) P3HT: PCBM (50:50) (black squares) and 86 wt% (50:50 P3HT: PCBM): 14 wt% PMMA films (red triangles) with the same thickness.	139
Figure 6.9	Power conversion efficiency as a function of time for P3HT: PCBM (50:50) binary blend, (open black squares), and 86 wt% (50: 50 P3HT: PCBM): 14 wt% PMMA, ternary blend	

(closed red squares) stored in environments with different humidity levels.....	142
Figure 6.10 J-V curves under AM 1.5 (a & b) and in the dark (c & d) for typical binary P3HT: PCBM (50:50) (red triangles) and ternary 86 wt% (50: 50 P3HT: PCBM): 14wt% PMMA (black squares) OPVs. (a & c) devices stored in 1 % RH. Filled symbols for initial measurements, open symbols for aged devices (after 800 h). (b & d) devices stored in 50 % RH, devices aged for 260 h.....	144
Figure 6.11 UV-visible absorbance spectra of P3HT: PCBM: PMMA and P3HT: PCBM blend films at different humidity levels. Red squares, as-deposited films; green circles, after T_{80} ; blue triangles, after T_{20} . The values of T_{80} and T_{20} are listed in Table 6.3.....	147
Figure 6.12 AFM topography images of (a) as-deposited (1:1) P3HT: PCBM film and (c) 86 wt%(50:50 P3HT: PCBM): 14 wt% PMMA film. (b & d) C-AFM images of the same areas, taken at 1 V bias.....	149
Figure 6.13 C-AFM images of aged P3HT: PCBM (a and b) and P3HT: PCBM: PMMA (c and d) films stored in 1% RH (a and c) and 50% RH (b and d). All images were taken at 1 V bias after 500 h.....	150
Figure 6.14 Histograms of the current probability distribution for P3HT: PCBM films (open symbols) and P3HT: PCBM: PMMA films (closed symbols) measured as-deposited and after storage for 500 h in 1% RH and 50% RH environments. The	

	measurements were performed on typical small areas (1.7 μm x 0.6 μm) of each device.	152
Figure 7.1	Power conversion efficiency as a function of time for binary (black squares) and ternary (red circles) devices containing 14 wt% a-PS stored in 50% and 1% RH.....	160
Figure 7.2	J-V curves under illumination for typical binary P3HT: PCBM (1:1) (black squares) and 86 wt% (50: 50 P3HT: PCBM): 14 wt% a-PS (red circles) OPVs.	161
Figure 7.3	Power conversion efficiency as a function of time for binary devices (black squares), and ternary devices containing 14 wt% PEG (red circles) stored at (a) 50% RH and (b) 1% RH.	162
Figure 7.4	The absorption spectra of P3HT: PCBM (black squares), and P3HT: PCBM: PEG films (red circles).	165
Figure 7.5	AFM topography images of (a) P3HT: PCBM, (b) P3HT: PCBM: PEG films.	166
Figure 7.6	Surface profiles (right) showing the depths of holes chosen from the AFM image (left). The numbers on the profiles indicate the positions of line scans on the topography image.	167
Figure 7.7	AFM images for a P3HT:PCBM:PEG film, (a) topography, (b) the C-AFM current map of the area in (a), (c) topography image of one hole, and (d) the current map of the area in (c), (scan area 2x2 μm) taken at 1 V.	168
Figure 7.8	Schematic diagram showing how the profile of the tip can affect the AFM image of features.	169

Figure 7.9	AFM images of the PEDOT: PSS layers from devices containing (a) a binary blend film and (b) a ternary blend film. (c) Phase image recorded at the same time as (b). The size of the scale bar is 10 μm	170
Figure 7.10	A typical line profile (right) taken from an AFM image (left) showing a hole in the active layer and a raised spot on the PEDOT: PSS layer. (x-axis is the distance (μm), and y-axis is the height (nm)).	171
Figure 7.11	Schematic structure of the ternary film morphology.....	171
Figure 7.12	Typical J-V curves, under illumination, taken directly after spin-casting for binary devices (black squares) and ternary devices (red circles).....	172
Figure 7.13	The structures of the four sets of devices.	174
Figure 7.14	PCE as a function of time for devices containing: a binary film (black squares), a ternary film (green diamonds), multilayer-unannealed film (red circles), and multilayer- annealed film (blue triangles).	175
Figure 7.15	AFM topography of (a) multilayer-unannealed film (set 3), and (b) multilayer-annealed film (set 4).....	176
Figure 7.16	AFM images of the PEDOT: PSS layer in (a) multilayer-unannealed film, (b) multilayer-annealed film.	177
Figure 7.17	The PCE as a function of time for devices based on P3HT: PCBM binary blend film (black squares), and P3HT: PCBM: PEG ternary blend film using mixed solvent (PEG dissolved in NB) (red circles).....	178

Figure 7.18	AFM topography images of (a) P3HT: PCBM film, (b) P3HT: PCBM: PEG film, spin-coated from mixed solvent.....	179
Figure 8.1	Log-log plot of J-V curve for expected single-carrier space charge limited current in a device containing a single set of traps, showing Ohmic (I), trap-filling (II), and trap free SCLC (III) regions.	185
Figure 8.2	Dark J-V curve on log-log scales for the hole-only binary device (red squares) and ternary device (black triangles), stored in 50% RH and 1% RH as-deposited (closed symbols) and after 360 h (open symbols).	186
Figure 8.3	Typical dark J-V curves on log-log scales for hole-only binary device (red squares) and ternary device (black triangles), stored in 1% RH at different aging times, as-deposited (closed symbols), after 336 h (crossed symbols), and after 1392 h (open symbols).	188
Figure 8.4	Dark current density as a function of internal voltage for typical hole-only devices based on P3HT (closed red diamonds), P3HT: PMMA (closed green circles), P3HT: PCBM (closed black squares), and P3HT: PCBM: PMMA (closed blue triangles). The open symbols relate to devices aged for 216 h. The solid lines represent the fits according to the equation of the SCLC (equation 8-1). The dotted line indicates that the slope of the plot for aged devices is ~ 1 , which represents the Ohmic region.....	190
Figure 8.5	J-V curves of aged hole-only devices after storage in 50% RH for 216 h. Devices based on P3HT (closed red diamonds),	

	P3HT: PMMA (closed green circles), P3HT: PCBM (closed black squares), and P3HT: PCBM: PMMA (closed blue triangles). The open symbols relate to aged devices after storage in 1% RH for 336 h.	192
Figure 8.6	Dark J-V curves for typical hole-only devices based on P3HT (closed red diamonds), P3HT: PMMA (closed green circles), P3HT: PCBM (closed black squares), and P3HT: PCBM: PMMA (closed blue triangles) as-deposited. The open symbols relate to devices aged for 216 h in a 50% RH environment.	194
Figure 8.7	SEM cross-sectional view of a P3HT: PCBM device with an Au top contact.	195
Figure 9.1	Schematic diagram illustrating the structure of laminated device.	202
Figure 9.2	AFM topography (left column) and phase images (right column), showing the morphology of the top surface of the device for: ((a) and (b)) a non-laminated device, ((c) and (d)) a device laminated with PMMA, and ((e) and (f)) a device laminated with PEG.	205
Figure 9.3	Power conversion efficiency as a function of time for control devices (black squares), devices laminated with PMMA (red circles) and devices laminated with PEG (blue triangles) ...	206
Figure 9.4	The electrical parameters, V_{oc} , FF, J_{sc} and PCE, as a function of time, for binary devices (black squares), ternary devices (red circles), laminated devices (green triangles), and ternary - laminated devices (blue diamonds).	208

Figure 9.5 Normalized average values of the fill factor, open circuit voltage, and short circuit current for a binary device (black squares), a ternary device (red circles), and a laminated device (blue triangles). (a) Devices stored in 50% RH, and (b) stored in 1% RH.210

Figure 9.6 Bubbles on the surface of the Al cathode of: (a) a binary device, and (b) a ternary device, as a result of storage in a high humidity environment for 1 hour.212

Figure 9.7 Schematic diagram illustrating the effect of gas bubble formation in (a) a binary device, (b) a ternary device, and (c) a dual device.214

LIST OF TABLES

Table 5.1	Assignments of the main features in pristine P3HT and PCBM	121
Table 5.2	Degradation products and their indication of appearance in the FTIR spectra as mentioned in references [4].	122
Table 6.1	Summary of the average values of basic device parameters of binary and ternary devices with different PMMA content.....	131
Table 6.2	The (r.m.s.) roughness and thickness of P3HT: PCBM: PMMA films containing different amounts of PMMA.....	136
Table 6.3	The lifetime of devices based on binary and ternary blends stored in environments with different humidity levels.....	142
Table 6.4	The average performance parameters of binary and ternary devices stored in 1% and 50% RH as-deposited and after 144 hours.....	145
Table 6.5	Series resistance values for typical ternary and binary devices stored in 1% RH and 50% RH, for different aging times.....	146
Table 6.6	The average values of the current, standard deviation and the coefficient of variation calculated from different areas chosen between spots on the binary and ternary blend film.....	151
Table 7.1	The T_{20} lifetime for devices including different insulating polymers stored in 50% RH.....	163

Table 7.2	The performance of as-deposited binary and ternary devices stored in 50% RH.	164
Table 8.1	The initial hole mobility values of a typical device in different blend films.....	191
Table 9.1	The average PCE obtained using various methods for lamination with PEG polymer.....	203
Table 9.2	The average performance of laminated devices.	204

DECLARATION

I hereby declare that the work carried out in this thesis has not been previously submitted for any degree and is not currently being submitted in candidature for any other degree.

Zakiya Al-Busaidi

July 2017

STATEMENT OF COPYRIGHT

Copyright © 2017 by Zakiya Nasser AL-Busaidi.

“The copyright of this thesis rests with the author. No quotations from it should be published without the author's prior written consent and information derived from it should be acknowledged.”

PUBLICATIONS

Papers

- Z. AL-Busaidi, C. Pearson, C. Groves, M.C. Petty, 'Enhanced lifetime of organic photovoltaic diodes utilizing a ternary blend including an insulating polymer,' Sol. Energy Mater. Sol. Cells. 160 (2017) 101–106.
- Highlighted in Renewable Energy Global Innovations, <https://reginnovations.org>, July 2017.

Conferences

- Z. AL-Busaidi, C. Pearson, C. Groves, M.C. Petty, 'Stability enhancement of organic photovoltaic devices using an insulating polymer,' Structured Soft and Biological Matter Conference, Durham University, June 2015.
- Z. AL-Busaidi, C. Pearson, C. Groves, M.C. Petty, 'Enhanced lifetime of organic photovoltaic devices using an insulating polymer,' North East Energy Materials Symposium, Durham University, April 2017

In preparation

- Enhanced lifetime of organic photovoltaic devices through lamination with an insulating polymer, for submission in Solar Energy Materials and Solar Cells.

ACKNOWLEDGEMENTS

After the praise and thanks to ALLAH, I believe that this thesis would not be possible without the endless support from my supervisors. First of all, my deep appreciation to Professor Michael C. Petty for his advice, unique ideas, support and his words of wisdom on the research and life, which I will never forget. Great thanks to Dr. Christopher Groves for his support, advice, great ideas, and for fast, clever and tough feedback that made my research more strong and accurate. Special thanks to Dr. Christopher Pearson for his teaching and helping me in different laboratory techniques, and for his patience when taking a large number of AFM images, which became a bit cumbersome. Thank you very much for all your useful discussions, special comments, and encouragement during the years of my study. I believe that the skills and knowledge that I learned from all of you will help me to become a better researcher.

I thank the Ministry of Higher Education in Oman for giving me the opportunity to study at Durham University and providing me all the financial support during the four years of study.

I would like to thank Dr. Michael Cooke and Mr. John Gibson for their help in my understanding about how the laboratory works. I thank everyone who helped me in the clean room. I would also like to thank all colleagues who I knew during my study. My thanks are also to Ms. Janet Berry and Dr. Sharon Cooper from Chemistry Department for training me to use the FTIR technique.

I thank Dr. Harith Al-Busaidi, Dr. Ashraf Al-Hinai and Iman Al-Hasani for helpful discussions concerning the chemistry of polymers and statistical concepts. My gratitude also goes to all my friends who supported and stood with me in the difficult days I had faced during my study.

Finally, no words are enough for the support of my family. My gratitude is to my Mother, Father, Brothers, and my Sisters. Finally, Great thanks go to my husband Mahmood AL-Salmi for his patience, love, understanding, and supporting me in every moment during my study. I also would like to thank my kids for encouraging and helping me especially in the final year.

DEDICATION

To those who showed me the endless of love and support:

my great parents.

To those who showed me the meaning of love and sacrifice:

my husband, Mahmood.

To those who made my life more colorful and beautiful: my

lovely daughters Deena, Mesan, Areen, and Rodina, my

wonderful sons, Mohammed and Tariq.

CHAPTER 1

INTRODUCTION, OBJECTIVE AND ORGANIZATION

1.1 Introduction

The greatest challenge facing humanity in the 21st century is a transition in the consumption of energy resources. A switch from non-renewable (oil, coal, and gas) to renewable, natural, abundant resources (the sun, wind, water, geothermal and biomass) is possible, but is problematic due to the complex and expensive technology required when using this type of energy. Non-renewable resources still provide most of the world's energy needs [1]. In 2001, 86% of the total global energy consumption was obtained from fossil fuels [2], and is predicted to account for 78%, in 2040 [1]. These non-renewable resources are already showing signs of depletion and their use is causing severe damage to the environment due to the emission of greenhouse gases. Concerns about the negative environmental impact of using fossil fuels make the switch to clean resources essential.

Renewables are the world's fastest growing source of energy, increasing at an average rate of 2.6%/year [1]. This is due to notable progress in the technologies that exploit renewable energy resources. According to the renewables global status report, they provided approximately 19.1% of global energy in 2013 [2], increasing to 19.3% at the end of 2015. Their growth in capacity and generation continues to expand [2].

The highest renewable energy growth has occurred in the power sector [3][4]. One of the reasons that led to this significant progress is the development of solar photovoltaic (PV) technologies. For example, solar PV represented about 47% of newly installed renewable power capacity in 2016, while wind and hydropower account for most of the remainder, contributing 34% and 15.5%, respectively [4].

Improvements in PV technology are basically driven by its increasing cost-competitiveness. For example, the most common PV technology is based on inorganic semiconductors, notably silicon. Because of their high initial cost and consequent long payback times, considerable efforts have been made to find cheaper alternatives. Organic photovoltaic (OPV) technology, based on polymer thin films, has been shown to provide a promising alternative to its silicon based counterpart. This is because of the low-cost solution processing techniques which are compatible with large area production as well as to mechanically flexible and light weight nature of devices [5]. OPVs usually consist of a blend of two materials; the first might be a conjugated polymer, which acts as an electron donor, while the second is usually a fullerene derivative working as an electron acceptor.

Enormous progress has been made in the efficiency of OPVs. An efficiency of around 11.3 % is the world record efficiency for OPVs at time of writing [6]. However, one major obstacle that prevents the commercialization of OPVs is their relatively short lifetimes [7]. Traditional inorganic photovoltaics have lifetimes of around 25 years [8]. In contrast, the lifetime of OPVs under illumination (1000 W/m^2), without

using any encapsulation techniques, is in the order of 1 or 2 weeks [8]. Therefore, an improvement in the lifetime of OPV is required before they can become a competitive alternative to inorganic PVs.

The degradation of OPVs is complex and cannot be described by a single process. Different factors such as light, water, oxygen, and the metal electrodes can lead to various degradation mechanisms inside the device [9].

1.2 Thesis Objective

The core objective of this study is to understand the degradation behavior of OPVs based on poly (3-hexylthiophene) (P3HT) and [6, 6]-phenyl-C₆₁-butyric acid methyl ester (PCBM) in an ambient environment and to find novel methods to enhance this lifetime. This study uses different insulating polymers to increase the lifetime of devices by blending them with the P3HT: PCBM active layer or by laminating the devices with these inert polymers.

1.3 Thesis Organization

The thesis is organized in the following way:

Chapter 2

This chapter discusses the history of PV technology and different types of OPVs. The basic working principle of energy conversion in OPVs and the electrical parameters used to analyze the performance of OPVs

are explained. The phenomenon of recombination processes occurring in the semiconductor materials is also described.

Chapter 3

The third chapter provides a literature review of the different factors that cause degradation in OPVs. This includes an illustration of various mechanisms that occur inside the OPV devices, such as the diffusion of water and oxygen and the consequent chemical degradation of the P3HT and PCBM materials.

Chapter 4

This chapter provides details of the experimental techniques that have been used in this thesis. A short description of the materials used in this study is also included. The fabrication processes, such as the preparation of the substrates and active layers are described. The lamination process is illustrated. The characterization techniques used to study the degradation processes are described. Finally, lifetime measurements and the aging tests in different environments are also explained.

Chapter 5

This chapter is the first results chapter. It compares the degradation of OPVs in ambient and inert environments. The chemical degradation mechanisms that may occur in the active layer of P3HT:

PCBM are investigated using Fourier Transform Infrared Spectroscopy (FTIR).

Chapter 6

In this chapter, ternary devices including PMMA are fabricated in an attempt to improve lifetime in an ambient environment. The effect of PMMA on device performance and lifetime is investigated. Different techniques are used to understand how PMMA affects the device lifetime and performance.

Chapter 7

This chapter deals with ternary devices using two different insulating polymers, polystyrene (PS) and polyethylene glycol (PEG), to study their impact on the lifetime of OPV devices. A comparison of ternary devices using PMMA, PS or PEG is discussed.

Chapter 8

This chapter analyzes binary and ternary OPVs based on PMMA, using the space charge limited current (SCLC) model. The dark J-V curves are analyzed in an attempt to understand the behavior of hole transport with degradation time and to calculate the hole mobility. The impact of humidity and the effect of changes in the metal contact on the conductivity are also investigated.

Chapter 9

This chapter introduces a new processing method, the lamination with an insulating polymer, to reduce the degradation in OPVs. The effect of this process on the performance and lifetime of the devices is investigated. A comparison between ternary and laminated devices is provided.

Chapter 10

This chapter concludes the findings in this study and provides suggestions for future work.

1.3 References

- [1] E. Information, "Analysis of the impacts of the clean power plan," 2015. [Online]. Available: <https://www.eia.gov/analysis/requests/powerplants/cleanplan/pdf/powerplant.pdf>. [Accessed: 12-Jul-2017].

- [2] N. Lewis and D. Nocera, "Powering the planet: chemical challenges in solar energy utilization," *Proc. Natl. Acad. Sci.*, vol. 103, no. 43, pp. 15729–15735, 2006.

- [3] G. S. Report, "Renewables 2015: global status report," 2015. [Online]. Available: <http://www.ren21.net>. [Accessed: 14-Oct-2016].

- [4] G. S. Report, "Renewables 2017: global status report," 2017. [Online]. Available: http://www.ren21.net/wp-content/uploads/2017/06/17-8399_GSR_2017_Full_Report_0621_Opt.pdf. [Accessed: 12-Jul-2017].

- [5] I. Report, "Renewable energy technologies: cost analysis series," 2012. [Online]. Available: https://www.irena.org/DocumentDownloads/Publications/RE_Technologies_Cost_Analysis-SOLAR_PV.pdf. [Accessed: 07-Jul-2017].

- [6] J. Yuan, J. Gu, G. Shi, J. Sun, H. Wang, and W. Ma, "High efficiency all-polymer tandem solar cells," *Sci. Rep.*, vol. 6, 26459, 2016.

- [7] D. Wöhrle and D. Meissner, "Organic solar cells," *Adv. Mater.*, vol. 3, no. 3, pp. 129–138, 1991.
- [8] K. Norrman and F. C. Krebs, "Lifetimes of organic photovoltaics: Using TOF-SIMS and $^{18}\text{O}_2$ isotopic labelling to characterise chemical degradation mechanisms," *Sol. Energy Mater. Sol. Cells*, vol. 90, no. 2, pp. 213–227, 2006.
- [9] Mikkel Jørgensen, K. Norrman, and F. C. Krebs, "Stability/degradation of polymer solar cells," *Sol. Energy Mater. Sol. Cells*, vol. 92, no. 7, pp. 686–714, 2008.

CHAPTER 2

BACKGROUND

2.1 Introduction

Solar energy is the most abundant energy resource and widely distributed so that, in every place in the world, has access to some degree. Solar energy can be captured and converted into electricity using photovoltaic (PV) technology. Developing this technology may partially solve the problems that the world is facing that are caused by the use of non-renewable, expensive, and polluting sources of energy and may subsequently help to meet the global demand for electricity.

The most common commercial PV technology is based on inorganic semiconductors. The efficiencies of these devices can reach 46% [1]. However, they also have high costs. They need around \$ 0.35 /kWh to cover the initial cost, whereas electricity derived from fossil fuels, costs only \$(0.02-0.05)/kWh, including the cost of storage and distribution [2]. Considerable efforts have been made to lower the price of photovoltaics, as is noticeable when studying the history of this technology.

In this chapter, the history of PV technologies is briefly discussed. The basic working principle of energy conversion and the physical parameters used to analyze the performance of photovoltaic devices are discussed.

2.2 The history of photovoltaic technology

Photovoltaics are electronic devices that convert light energy into electrical energy using semiconductor materials, which are intermediate between metals and insulators. PV technologies can be categorized into wafer-based and thin film cells [1]. Wafer-based cells are fabricated on semiconducting wafers which also serve as a substrate, while thin film cells are semiconducting materials deposited as films on glass, plastic, or metal [1]. Today there are different PV technologies on the market, using variety of materials which are classified into three generations, as described below.

2.2.1 First generation PV technology

The earliest PV technology is based on crystalline silicon wafers [3]. It dates back to 1954, when Chapin, Fuller, and Pearson used a crystalline silicon p-n junction to produce the first solar cell with a power conversion efficiency of 6% [4]. These devices were primarily used for the space industry and started to be commercialized in the 1970s [5]. Today, this generation is commercially available, and has a 90% share of the solar market [6], with a peak power conversion efficiencies of 25% in the laboratory [5] and 22.4% when manufactured for a large area of up to 7 m² [7].

This generation of solar cells is physically rigid because they are produced on a wafer [8]. Also, the manufacturing cost of crystalline silicon is high [8], and the pure silicon itself is costly [4]. The cost of panels per unit area is even greater than the expense of the vast area of

land needed [6]. Therefore, the need for cost reduction has encouraged researchers to search for a replacement for silicon.

2.2.2 Second generation PV technology

Second generation PV technology has lower production cost than that of the first generation, although is not necessarily higher performance. Second generation solar cells include materials such as amorphous silicon, cadmium telluride, gallium arsenide, copper indium selenide and copper indium gallium diselenide [3]. Such materials are deposited as thin films rather than using wafer based technology. Thin film devices are based on one or more thin layers each less than a micron thick of semiconductor material on a substrate [7]. This means that the deposited layer is 100-1000 times thinner than a silicon wafer [4]. Using less material leads to a reduction in the cost of fabrication, which is a key advantage. This technology can also be used to fabricate devices on flexible substrates, and therefore it becomes more versatile [3].

Despite the lower costs, each thin film material has its own disadvantages. For example, amorphous silicon PVs are not stable and their performance degrades when exposed to the sunlight by 15% to 35% [3], while their power conversion efficiency is low (8%-12%) compared to the efficiency of the first generation of PVs [7]. Cadmium telluride is a toxic material and harmful to the environment [4]. Gallium arsenide, copper indium selenide, and copper indium gallium diselenide are the most efficient 2nd generation devices to date (28%) [1], but they are more expensive than silicon solar cells [3].

2.2.3 Third generation PV technology

This generation includes various novel technologies that are still under development and need more understanding and investigation. These technologies include concentrated PV (CPV), dye-sensitized, perovskite, quantum dot, and OPV [3]. Commercially, this generation of PVs is not widely available, with some types just beginning to be commercialized [3]. The aim of these technologies is to provide low cost and high performance compared with previous generations. However, they have many disadvantages that need to be addressed. For example, CPV technology uses III-V semiconductors [3] and depends on focusing a large area of solar radiation onto a small area of multijunction solar cells [3]. The requirement for a complicated optical system could make this technology far from commercially viable [1]. Dye-sensitized solar cells are based on dye molecules [1], but their low efficiency, poor stability, and limited absorption have led to the development of another type of PV which is perovskite solar cells [3]. This technology has a power conversion efficiency of 20% in the laboratory [9], but it suffers from low stability [1]. Quantum dot PV technology uses nanoparticles of compound semiconductors which are stronger light absorbers [3]. However, the low efficiency and an incomplete understanding of this technology [1], reduces its ability to compete with other PV technologies.

Organic PV is another promising technology which utilizes carbon-based semiconducting polymers or small molecules [7]. These materials are synthesized using Earth-abundant elements and can be easily processed as plastic [1]. Although this technology suffers from low

stability, it is attractive and may compete with other PV technologies [3]. The reasons for this will be illustrated in the following section.

2.3 Why organic photovoltaics?

Organic PVs are made from organic semiconducting materials such as polymers and small molecules [7]. The idea for this technology stems from the photosynthetic processes in plants, where sunlight is converted into chemical energy [7]. The era of organic electronics began in the 1970s, when Heeger, Shirakawa, and MacDiarmid, discovered that polymers can have conductive properties, for which they received the Nobel prize in 2000 [9]. The low cost of organic materials and the ability to use spray coating, inkjet printing, and roll-to-roll coating techniques have allowed the manufacture of large area OPVs on flexible substrates [8] [7]. This offers a route to very low cost mass production of OPVs [8].

The performance of OPVs has steadily increased from <1% [7] to 11.3% [10] and, in the future, their efficiency may challenge that of inorganic PV technology. However, a major disadvantage that still restricts the commercial use of OPVs is low stability. OPVs are highly sensitive to the atmosphere and light, which results in short lifetimes [11]. The required lifetime for commercialization is 5-20 years [12]. However, the typical lifetime without encapsulation techniques is in order of one or two weeks [13]. This means that considerable improvements are required.

2.4 Organic semiconductors

The conductivity in organic semiconductors originates from the presence of sp^2 -hybridized carbon atoms [8]. This can result in single (σ) and double (π) bonds between carbon atoms along the polymer backbone [8]; known as conjugation [14]. If a carbon in the conjugated polymer has three electrons in sp^2 orbitals forming three σ bonds, one (π) electron will be contained in the p-orbitals. These p-orbitals overlap with adjacent atoms creating an arrangement which allows π electrons to delocalize along the polymer backbone, forming a π -bond. [7]. Figure 2.1 (b) shows the σ and π bonds of the simplest conjugated organic molecule: ethylene

The π -bond splits into two energy states: π and π^* orbitals. In the lower energy state, electrons occupy the π -orbital, so it is referred as the Highest Occupied Molecular Orbital (HOMO). The π^* -orbital is known as the Lowest Unoccupied Molecular Orbital (LUMO). HOMO-LUMO orbitals are similar to valence-conduction bands in inorganic semiconductors. Figure 2.1 (c) shows the HOMO and LUMO orbitals of ethylene ($CH_2=CH_2$).

The difference between the HOMO and LUMO orbitals is known as the band gap. The band gap determines the energy required to excite an electron from the HOMO to the LUMO and therefore the absorption of the polymer. Typically, the value of the band gap in conductive polymers is around 1.5-3 eV [7].

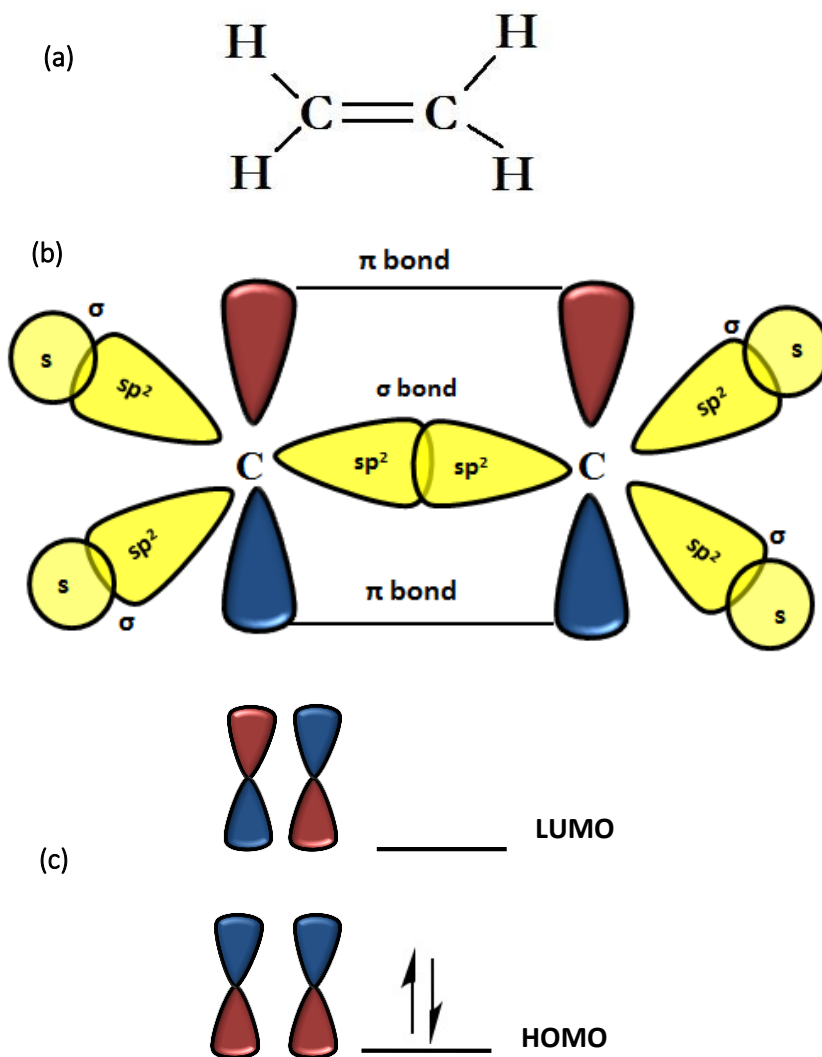


Figure 2.1. (a) The chemical structure of the simplest conjugated organic material: ethylene, (b) σ and π bonds of ethylene, and (c) Formation of HOMO and LUMO orbitals in ethylene. Redrawn from [15].

However, in insulating polymers, carbon atoms often have four single bonds (σ bonds), so that all electrons are localized and used for bonding, and no delocalization of electrons occurs [16].

2.5 Energy conversion in photovoltaic technologies

The basic physics of PVs is similar to that of a p-n junction diode [17]. The energy band diagram of a simple p-n junction diode is illustrated in Figure 2.2. When a photon of sufficient energy is absorbed, an electron-hole pair is generated. The hole and electron are not tightly bound in an inorganic semiconductor. They may separate from each other by the built-in electric field in a depletion region. Then, the separated charges travel to the electrodes [8].

Three important physical processes are required to create a photoelectric effect in any material. These are charge generation, charge separation, and finally, charge transport to their respective electrodes. In OPVs, the low dielectric constant results in a strong Coulomb force of attraction between charges [18]. Therefore, the absorption of photons in the organic materials forms excitons rather than free charge carriers. The strong bound hole-electron pairs must be dissociated into free holes and electrons. The energy required to dissociate the exciton (binding energy) is large (0.1–1eV) compared to inorganic semiconductors $\sim 0.01\text{eV}$ [8], [19]. Therefore, the dissociation process in OPVs is not easy, and a special strategy is required to achieve free holes and electrons.

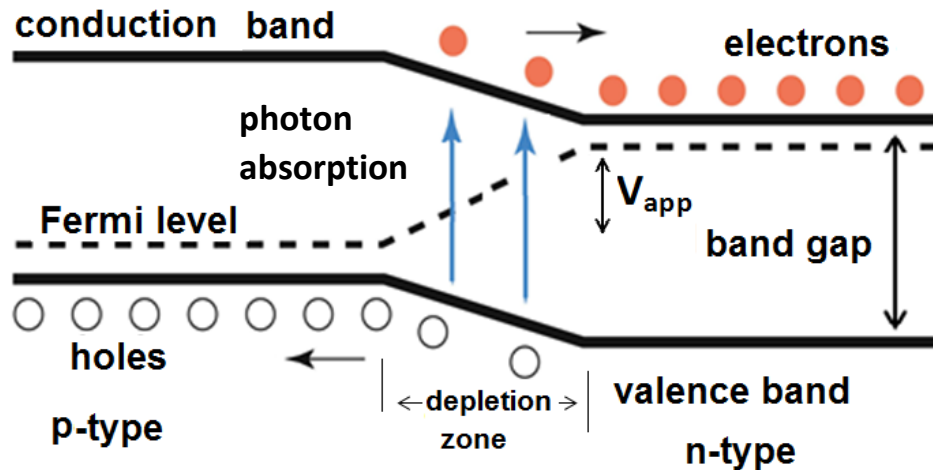


Figure 2.2. The energy level diagram for a p-n junction photodiode. Redrawn from [20]

2.6 Operating principles of OPVs

Similar to p-n junction diodes, OPVs should be comprised of p-type and n-type materials. Therefore, two different materials are used, one works as an electron donor and the other one as an electron acceptor. The most studied donor-acceptor blend used in OPVs is based on poly(3-hexylthiophene) (P3HT) and the fullerene derivative [6,6]-phenyl-C₆₁-butyric acid methyl ester (PCBM) [21], which are the materials used in this thesis.

The conversion process in OPVs involves four crucial steps [21]: 1) exciton generation, 2) exciton diffusion, 3) exciton dissociation, and 4) charge transport and collection at the electrodes. Figure 2.3 summarizes these conversion processes.

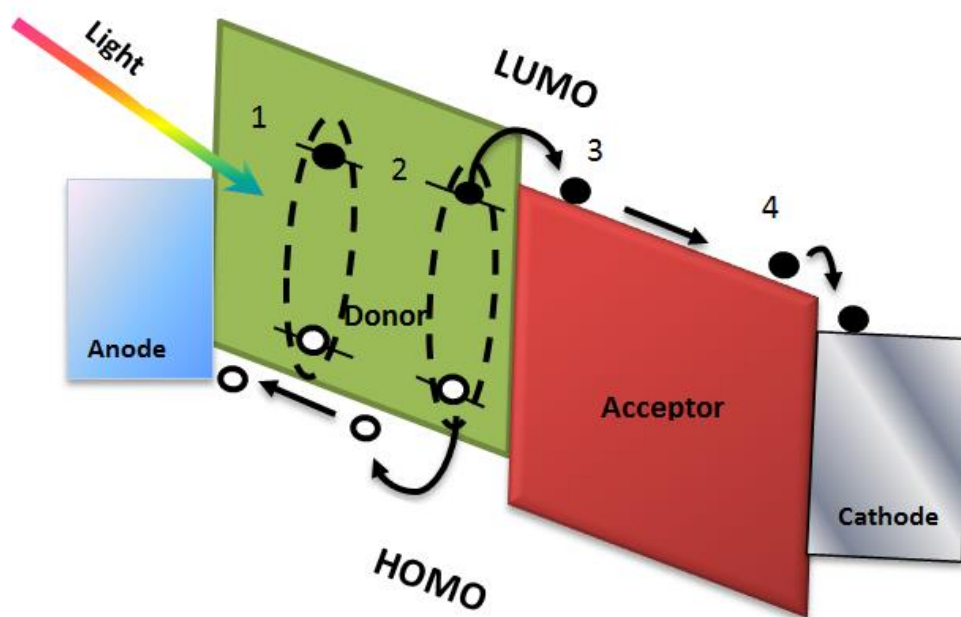


Figure 2.3. Working mechanisms of OPVs. Redrawn from [8].

In step 1, a photon with sufficient energy is absorbed by the donor. An electron is excited from HOMO to LUMO, creating an exciton. During its short lifetime ($\sim 100 \text{ ps} - 1 \text{ ns}$) [22], excitons can diffuse within the material, with a diffusion length of approximately 10 nm [23]. The exciton may diffuse to the interface between an acceptor and donor, as shown in step 2. Here, the difference in electron affinities and ionization potentials between donor and acceptor dissociates the exciton [24], as shown in step 3. Therefore, if the excitons reach the donor /acceptor interface, dissociation can occur in which electrons transfer to the LUMO of the acceptor whereas holes remain on the donor HOMO orbital or vice versa. If the excitons do not reach an interface, they will recombine, and the absorbed energy will be lost [25]. The difference in work function between electrodes produces an internal potential (V_{bi}) which helps charge carriers to transport to the respective electrodes [19], as in step

4. The same process happens if the exciton is generated in the acceptor. At the donor/acceptor interface, dissociation occurs in which holes transfer to the HOMO of the donor and then to the anode, while electrons remain in the LUMO of the acceptor and then transfer toward the cathode.

2.7 Device architectures

During the development of OPVs, different architectures of active layers have been investigated, as shown in Figure 2.4.

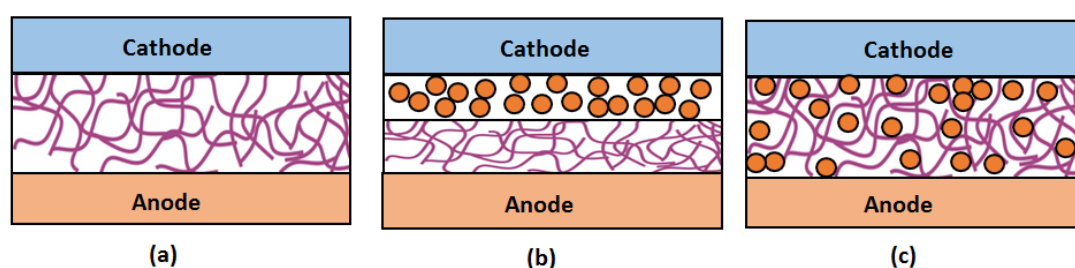


Figure 2.4. Schematic illustration of different OPV architectures a) single layer, b) bilayer and c) bulk heterojunction (BHJ). Purple lines represent electron-donor organic material and orange circles represent electron-acceptor organic material.

2.7.1 Single layer OPVs

The first OPVs manufactured in 1958 and were based on a single layer that was sandwiched between two metals with a large work function difference [26]. The organic materials were based on bio-organic dyes such as porphyrins [26]. This type of material was chosen because it is similar to chlorophyll, a green pigment absorbing light for the photosynthetic process in plants [8]. The devices showed very low efficiency ($< 0.1\%$) because of inefficient exciton separation [27]. The

different work functions of the electrode produce a built-in voltage across the semiconductor, but this was not strong enough to dissociate the excitons into free carriers [7].

2.7.2 Bilayer OPV

In 1986, Tang was the first to discover that using two different materials can improve exciton dissociation [8]. He made bilayer devices consisting of an electron donor having a low ionization potential and an acceptor material, which has high electron affinity [28]. The bilayer structure showed an efficiency of 1% [24]. The improvement in the efficiency was due to an improvement in the efficiency of exciton dissociation. The difference in electron affinity between the two organic materials increases the efficiency of dissociation.

Although this structure improves the performance of OPVs, another problem still exists which limits the performance. The distance that excitons can diffuse without recombination (diffusion length) is very small (~ 10 nm) [25] compared to the thickness of the photoactive layer. Therefore, most of the excitons recombine, and only the excitons at the interface are separated into free carriers [19]. Therefore, the major reason for low efficiency in bilayer devices is the small interfacial area between the donor and acceptor materials. The challenge was to find a way to maximize the interface area and organize the donors and acceptors so that the phase separations are within the exciton diffusion length [25].

2.7.3 Bulk heterojunction OPV BHJ

A breakthrough in the architecture of OPVs happened in 1995 when Heeger et al. discovered that mixing the donor and acceptor into a single layer increased the device efficiency to 1.5% [19]. This new architecture, which is called a bulk heterojunction (BHJ) OPV, allows the heterojunction to occur throughout the active layer and increases the interfacial area between the donor and acceptor phases (Figure 2.6 (c)) [19]. Today, most OPVs are based on this structure. However, dissociated charges need continuous pathways to allow electrons and holes to travel to their electrodes. This means that the donor and acceptor have to form a nanoscale network [17]. If the pathways are not continuous (forming dead ends), the efficiency of hole and electron transport to the electrodes is low [25]. To produce the required nanoscale morphology and improve charge transport, it is necessary to optimize the morphology of the donor and acceptor phases [25].

Obtaining the desired nanoscale morphology is very complex, because it strongly depends on the chemical structures of the donor and acceptor [17], and on the fabrication process [19], [29]. It was found that the chemical structures of donor and acceptor have an influence on their miscibility as well as their crystallinity [30]. Fabrication processes, also have a strong effect on morphology [29]. Many studies showed that the nature of the solvent, thermal annealing [31], solvent annealing [32], and blending ratio of donor and acceptor materials [30] have a strong effect on the crystallinity of donor material in the blend [33]. Enhanced

crystallinity can improve optical absorption, [33], charge separation [34] and charge transport [33], [34].

2.8 Electrical characterization of OPVs

It is important to define the physical parameters that are used to analyze the performance of OPVs, such as short-circuit current density (J_{sc}), open circuit voltage (V_{oc}), fill factor (FF) and power conversion efficiency (PCE). These parameters can be extracted from the J-V curve which is generated when a voltage sweep is applied to the device illuminated by light. A standard illumination is used to characterize PVs, known as AM 1.5 G. This implies a particular spectrum and intensity of 100 mW/cm^2 . In the dark, the J-V curve passes through the origin with no current generation but, when the device is exposed to light, a photocurrent is generated, and the device operates in the forward bias regime, causing the J-V curve to shift downward, as shown in Figure 2.5.

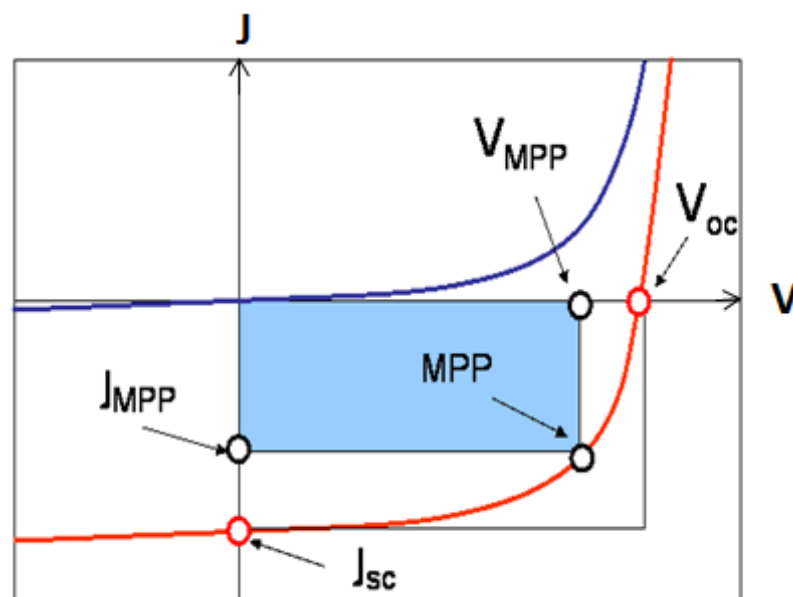


Figure 2.5. J-V characteristics of an OPV device under illumination (red) and in the dark (blue).

2.8.1 Short-circuit current

Short-circuit current density (J_{sc}) is the photocurrent density that is produced when no voltage is applied across the illuminated device. It is approximately proportional to the amount of light absorbed by the active layer [19]. The absorption spectrum of BHJ OPVs materials does not perfectly match the solar spectrum, and thus limits their efficiency [35]. To absorb a major part of the solar spectrum, the thickness of the active layer should be large [36], but within certain limits, to prevent series resistance or recombination from increasing [37]. Increasing the series resistance in OPVs can reduce the efficiency of charge collection and charge transport [38], which in turn causes a rapid decrease in J_{sc} . Li et al. suggested that a thickness of 210-230 nm is optimal in a P3HT: PCBM film to absorb incident light efficiently [39], although others have noted that this thickness is not favorable due to a significant increase in series resistance [38].

2.8.2 Open-circuit voltage

The open-circuit voltage (V_{oc}) is the maximum voltage across the device at zero current [40]. The origin of V_{oc} has been studied widely, and it is found that V_{oc} is related to the energy difference between the LUMO of the acceptor and HOMO of the donor [7], [41], [42]. For example, the P3HT-PCBM system has an open circuit voltage of about 0.6 V due to the relatively large difference in acceptor LUMO and donor HOMO [35]. The band gap in OPVs is influenced by the morphology because the crystallinity of a polymer like P3HT can result in a change in

the HOMO level, causing a change in the band gap of the polymer [42]. Thus, the difference between the HOMO of the donor and the LUMO of the acceptor will vary, resulting in a change in the value of V_{oc} [41]. Figure 2.6 shows the energy diagram of a P3HT: PCBM OPV.

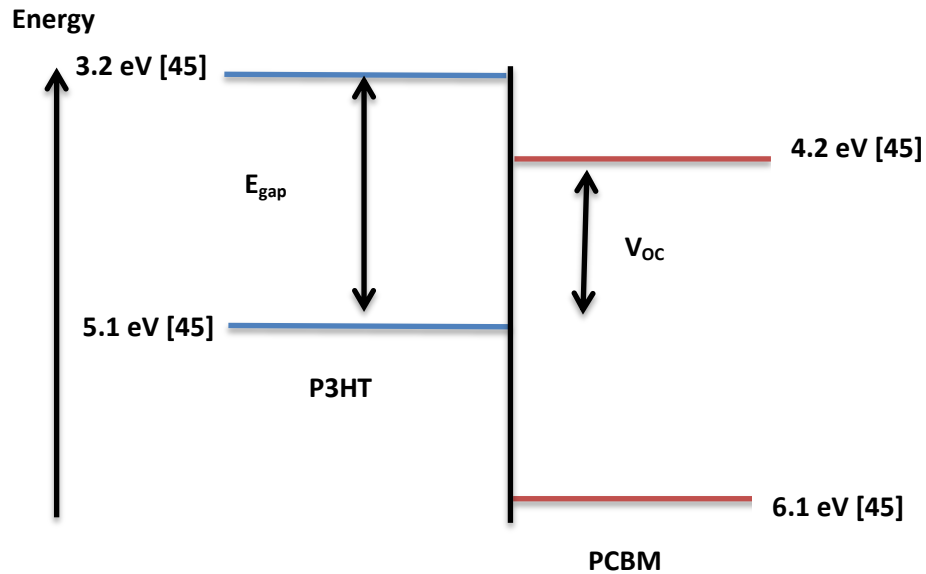


Figure 2.6. Energy diagram of a P3HT-PCBM solar cell [42][43].

2.8.3 Fill Factor

The fill factor is defined as the ratio between the maximum obtainable output power and the product of J_{sc} and V_{oc} . The formula for FF is given by [8]:

$$FF = \frac{J_{mpp} V_{mpp}}{J_{sc} V_{oc}} \quad (2.1)$$

The maximum power point (mpp) represents the output power under normal operation. It can be represented in the J-V curve by the

largest area of the resulting rectangle [27], which is illustrated as a shaded rectangle in Figure 2.5. The area of the larger rectangle represents the product of J_{sc} and V_{oc} . The FF is an important parameter and is related to the shape of the J-V characteristics under illumination [19].

The FF depends on transportation and recombination processes in the OPV [42]. If the hole and electron transport is unbalanced, space charge builds up, which reduces the built-in potential across the device [44] and decreases the FF [42]. It is also affected by the series resistance. A high series resistance reduces the FF and thus lowers the efficiency [45]. A high FF can be due to an increase in the interpenetration network in the film, interface transfer, and transport through the contacts [8]. Film morphology is a major factor that can affect the FF. Different studies have reported that a high order of donor and acceptor materials leads to high carrier mobility, leading to an increase in the FF [17].

2.8.4 Power conversion efficiency

Power Conversion Efficiency (PCE) is the ratio of maximum power generated by the device ($J_{mpp} V_{mpp}$) to the power of the incident light (P_{in}) [27]. The PCE reflects how efficient the device is converting the light into electricity. It can be calculated from [8]:

$$PCE = \frac{P_{out}}{P_{in}} = \frac{J_{mpp} V_{mpp}}{P_{in}} = \frac{J_{sc} V_{oc} FF}{P_{in}} \quad (2.2)$$

2.9 Recombination mechanisms in OPVs

Recombination is considered to be a major loss mechanism in OPVs because it results in a decrease in the short circuit current, the fill factor and the open-circuit voltage [46]. Recombination is a natural phenomenon that occurs in all semiconductor materials. There are two main types of recombination mechanisms in OPVs, geminate and non-geminate recombination [47].

2.9.1 Geminate recombination

Geminate recombination is illustrated in Figure 2.7 (a) and (b), and occurs before the generation of a free carrier. When a photon is absorbed, a photoexcited electron-hole pair (exciton) is formed, which is bound by the Coulomb interaction [46]. The Coulomb binding energy must be overcome in order to separate this exciton into free charges. Otherwise, the pair will undergo relaxation. [48].

However, for most bulk heterojunction OPVs, excitons efficiently find a donor/acceptor interface for dissociation. When the exciton reaches the interface, it dissociates into an electron in the acceptor and a hole in the donor, forming a bound geminate electron-hole pair, which means that the electron-hole pair is bound across the interface in the charge transfer state (CT) [47].

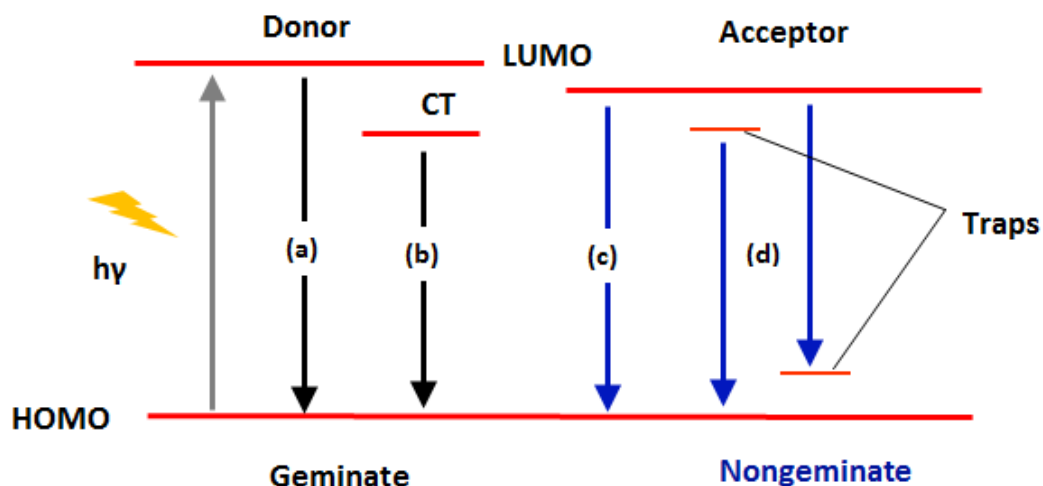


Figure 2.7. Different recombination mechanisms in OPVs. The exciton formed after light absorption (gray arrow). The geminate mechanisms: (a) exciton decay after excitation, (b) recombination at the D/A interface through the charge transfer state (CT). Nongeminate mechanisms: (c) band to band recombination, (d) trap-assisted recombination.

At this stage, the electron may recombine to the ground state or via triplet states. Triplet states are electronic states with a net spin of one [49]. If the triplet state has energy lower than that of the CT state, geminate recombination occurs, and the CT states are deactivated.

There has been a large discussion on whether a geminate pair will recombine, or dissociate into free carriers [50]. Recently, several studies have shown that this type of recombination is not a major loss mechanism [46]. Therefore, it is possible that the charge transfers from donor to acceptor directly, giving a free charge carrier without undergoing geminate recombination.

2.9.2 Non-geminate recombination

After the electron-hole pair is dissociated successfully into free carriers, the electrons and holes must transfer to their electrodes.

However, their pathway is not easy because they hop from one molecule to another and recombination is possible. The recombination of free electrons and holes is known as non-geminate recombination [47]. It was found that in OPV devices a decrease in charge extraction occurred when a forward bias was applied, due to a reduction in the driving force for charge extraction [46]. All photogenerated free carriers will recombine when the forward bias is equal to V_{oc} . Hence the recombination of free carriers occurs in OPV devices, whatever their performance [47]. Many studies have reported that non-geminate recombination is a major loss mechanism that reduces device performance [46], [51]. Heeger et al. [46] indicated that recombination is bias-dependent. They found that at the short circuit current condition, small non-geminate recombination occurred. The reduction in J_{sc} occurred due to the increase in recombination with applied bias [46]. Non-geminate recombination arises from three different mechanisms: trap-assisted, band to band, and recombination at the contacts [47]. These different recombination mechanisms are illustrated in Figure 2.7.

(a) Band to band recombination

In inorganic semiconductors, band to band recombination occurs when a free electron from the conduction band recombines with a hole in the valence band. In organic semiconductors, the structure is disordered and causes localized charge carriers [52]. Therefore, the rate of recombination of free carriers depends on the charge carrier mobility [47]. A faster carrier has a higher probability of finding another carrier with which to recombine.

This type of recombination can be described by the Langevin equation, which can be written as [53]:

$$R_{Langevin} = \frac{q}{\varepsilon}(\mu_n + \mu_p)(np - n_i p_i) \quad (2.3)$$

where q is the elementary charge, ε the dielectric constant, μ_n the mobility of electrons through the LUMO of the acceptor, μ_p the mobility of holes through the HOMO of the donor, n and p represent the electron and hole charge carrier density respectively, and $n_i p_i$ is the intrinsic carrier concentration.

However, the first part of the Langevin equation is known as the Langevin recombination rate coefficient and is represented by:

$$\gamma = \frac{q}{\varepsilon}(\mu_n + \mu_p) \quad (2.4)$$

From this equation, it is understood that the rate of recombination should increase with mobility. However, it has been shown by different studies that this type of recombination in OPVs is less strong than predicted by the Langevin equation [54], [55]. Therefore it seems that Langevin recombination is an incomplete description of non-geminate recombination in OPVs [47]. For instance, Neher et al. found that there is a relationship between the morphology and Langevin recombination [56]. They observed that an increase in phase separation between donor and acceptor could reduce this type of recombination.

(b) Trap-assisted recombination

Trap-assisted recombination occurs when a mobile carrier (hole or electron) recombines with a trapped carrier [46], as illustrated in Figure 2.7 (d). This means that the recombination rate depends on the number of traps. Traps originate from the disordered structure of an organic semiconductor, due to existing chemical defects [46], [57], vacancies [58], impurities [59], and kinks in the polymer backbone, causing conjugation breaks [52]. This structure leads to the formation of traps with different energy levels, known as shallow and deep traps [57]. Graupner et al. found that shallow traps result from variations in the electronic band due to aggregation and crystallization of the organic molecules, while deep traps result from chemical defects in the polymer backbone or impurities which break the conjugation of the polymer [57]. In addition, it was found that deep traps may cause polarization effects that result from the diffusion of water and oxygen into the OPV device [60]. However, in another study, it was reported that structural defects lead to shallow trap formation [60]. It seems that the formation of carrier traps in OPVs is still not fully understood [61].

Trap assisted recombination is also known as Shockley-Read-Hall (SRH) recombination and can be described through the SRH equation [47], [52]:

$$R_{SRH} = \frac{C_n C_p N_t (np - n_i^2)}{[C_n (n + n_1) C_p (p - p_1)]} \quad (2.5)$$

C_n is the probability per unit time that an electron in the conduction band will be captured when a trap is empty. C_p indicates the probability per unit time that a hole will be captured when a trap is filled. N_t is the density of electron traps. n and p are the electron density in the conduction band, and the hole density in the valence band, respectively and n_i is the intrinsic carrier concentration in the sample.

It was reported that most trap-assisted recombination processes occur in the donor material while the acceptor material is known to be trap free. [47]. However, Street et al. showed that the dominant recombination occurred through interface states between the polymer and fullerene domains [51]. They proposed that those trap states in the interface or near the interface lead to trapping of electrons or holes and hence caused recombination [51]. Therefore, the recombination rate is proportional to the trap density [46].

(c) Recombination at the contacts

Another recombination mechanism that may occur is at a metal contact. This happens when minority free carriers diffuse toward the contacts and then recombine there [51]. This mechanism becomes very significant when the free carriers are created close to the contact [51]. Electrons in the anode can recombine with holes, and holes in the cathode can recombine with electrons reducing the efficiency of charge collection and lowering device performance [47]. However, Street et al. reported that this is not a major loss mechanism [51].

2.10 Device lifetime

Lifetime is the problem facing all devices based on organic materials. It has been found that all of the layers in OPVs are susceptible to physical or chemical degradation with different processes occurring at different aging times [62].

The typical lifetime of an OPV without encapsulation is of the order of a few days to a few weeks [44]. Many reports have shown that the degradation mechanisms in OPVs are complex and not fully understood [30]. The device performance decreases rapidly when the devices are exposed to the ambient environment, as well as to light [13], [63]. Most studies noted that oxygen and moisture are the major reasons for degradation [11], [13], [63]. They can react with the organic materials and form oxidation products which lead to instability [63]. These degradation mechanisms will be explained in more detail in Chapter 3.

2.11 References

- [1] J. Jean, P. R. Brown, R. L. Jaffe, T. Buonassisi, and V. Bulović, "Pathways for solar photovoltaics," *Energy Environ. Sci.*, no. 8, pp. 1200–1219, 2015.
- [2] N. Lewis and D. Nocera, "Powering the planet: chemical challenges in solar energy utilization," *Proc. Natl. Acad. Sci.*, vol. 103, no. 43, pp. 15729–15735, 2006.
- [3] IRENA, "Renewable energy technologies: cost analysis series," 2012. [Online]. Available: https://www.irena.org/DocumentDownloads/Publications/RE_Technologies_Cost_Analysis-SOLAR_PV.pdf. [Accessed: 07-Jul-2017].
- [4] M. A. Green, "Photovoltaics: technology overview," *Energy Policy*, vol. 28, pp. 989–998, 2000.
- [5] M. Bilgili, A. Ozbek, B. Sahin, and A. Kahraman, "An overview of renewable electric power capacity and progress in new technologies in the world," *Renew. Sustain. Energy Rev.*, vol. 49, pp. 323–334, 2015.
- [6] Solar cell central.com, "Solar markets," 2011. [Online]. Available: http://solarcellcentral.com/markets_page.html. [Accessed: 15-Oct-2016].

- [7] E. Glowacki, N. Sariciftci, and C. Tang, "Organic solar cells," *Sol. Energy*, pp. 97–128, 2013.
- [8] H. Hoppe and N. S. Sariciftci, "Organic solar cells: An overview," *J. Mater. Res.*, vol. 19, no. 7, pp. 1924–1945, 2004.
- [9] A. Chilvery, K. Xiao, R. Lal, J. Currie, and B. Penn, "Perovskites : transforming photovoltaics , a mini-review," *J.P Energy*, vol. 5, p. 057402, 2015.
- [10] J. Yuan, J. Gu, G. Shi, J. Sun, H. Wang, and W. Ma, "High efficiency all-polymer tandem solar cells," *Sci. Rep.*, vol. 6, 26459 , 2016.
- [11] H. Cao, W. He, Y. Mao, X. Lin, K. Ishikawa, J. Dickerson, and W. Hess, "Recent progress in degradation and stabilization of organic solar cells," *J. Power Sources*, vol. 264, pp. 168–183, 2014.
- [12] E. Voroshazi, B. Verreet, T. Aernouts, and P. Heremans, "Long-term operational lifetime and degradation analysis of P3HT:PCBM photovoltaic cells," *Sol. Energy Mater. Sol. Cells*, vol. 95, no. 5, pp. 1303–1307, 2011.
- [13] C. H. Peters, I. T. Sachs-Quintana, J. P. Kastrop, S. Beaupré, M. Leclerc, and M. D. McGehee, "High efficiency polymer solar cells with long operating lifetimes," *Adv. Energy Mater.*, vol. 1, no. 4, pp. 491–494, 2011.

- [14] Y. Tasi, W. Chu, F. Juang, R. Tang, T. Hsieh, and M. Liu, "Efficiency improvement of organic solar cells by slow growth and changing spin-coating parameters for active layers," *Jpn. J. Appl. Phys.*, vol. 50, 022301–022304, 2011.
- [15] L. Chemistry, "Advanced theories of covalent bonding: multiple bonds," *Open Stax College*. [Online]. Available: <https://courses.lumenlearning.com/chemistryformajorsxmaster/chapter/multiple-bonds-2/>. [Accessed: 06-Oct-2016].
- [16] M. Syed, K. Iqbal, W. Younis, and K. Karimov, "Space charge-limited current model for polymers," in *Conducting Polymers*, F. Yilmaz, Ed. InTech, 2016, pp. 91–117.
- [17] S. Gunes, N. Helmut, and N. Sariciftci, "Conjugated polymer-based organic solar cells," *Chem. Rev.*, vol. 107, no. 4, pp. 1324–1338, 2007.
- [18] A. Köhler and H. Bässler, "Triplet states in organic semiconductors," *Mater. Sci. Eng. R*, vol. 66, no. 4–6, pp. 71–109, 2009.
- [19] P. Kumar and S. Chand, "Recent progress and future aspects of organic solar cells," *Prog. photovoltaics Res. Appl.*, vol. 20, pp. 377–415, 2012.
- [20] T. Ive and Å. Haglund, "The Nobel prize in physics 2014," *Faculty of Science*, 2014. [Online]. Available: <http://science faculty magazine.com/natural-sciences-en/physics/the-nobel-prize-in-physics/>.

[Accessed: 15-Nov-2016].

- [21] B. Thompson and J. Fre'chet, "Polymer-fullerene composite solar cells," *Angew. Chem. Int. Ed.*, vol. 47, no. 1, pp. 58–77, 2008.
- [22] T. Clarke and J. Durrant, "Charge photogeneration in organic solar cells," *Chem. Rev.*, vol. 110, pp. 6736–6767, 2010.
- [23] G. Dennler, M. C. Scharber, and C. J. Brabec, "Polymer-fullerene bulk-heterojunction solar cells," *Adv. Mater.*, vol. 21, no. 13, pp. 1323–1338, 2009.
- [24] P. Blom, V. Mihailetschi, J. A. Koster, and D. Markov, "Device physics of polymer:fullerene bulk heterojunction solar cells," *Adv. Mater.*, vol. 19, no. 12, pp. 1551–1566, 2007.
- [25] X. Yang, J. Loos, S. Veenstra, W. Verhees, M. Wienk, J. M. Kroon, M. Michels, and R. Janssen, "Nanoscale morphology of high-performance polymer solar cells," *Nano Lett.*, vol. 5, no. 4, pp. 579–583, 2005.
- [26] D. Wöhrle and D. Meissner, "Organic solar cells," *Adv. Mater.*, vol. 3, no. 3, pp. 129–138, 1991.
- [27] T. Benanti and D. Venkataraman, "Organic solar cells : an overview focusing on active layer morphology," *Photosynth. Res.*, vol. 87, pp. 73–81, 2006.
- [28] G. Horowitz, "Organic thin film transistors: from theory to real

- devices," *J. Mater. Res.*, vol. 19, no. 7, pp. 1946–1962, 2004.
- [29] B. Gholamkhash and S. Holdcroft, "Toward stabilization of domains in polymer bulk heterojunction films," *Chem. Mater.*, vol. 22, pp. 5371–5376, 2010.
- [30] W.-H. Baek, T.-S. Yoon, H. H. Lee, and Y.-S. Kim, "Composition-dependent phase separation of P3HT:PCBM composites for high performance organic solar cells," *Org. Electron.*, vol. 11, no. 5, pp. 933–937, 2010.
- [31] M. Dang, L. Hirsch, G. Wantz, and J. Wuest, "Controlling the morphology and performance of bulk heterojunctions in solar cells. Lessons learned from the benchmark poly(3-hexylthiophene):[6,6]-phenyl-C₆₁-butyric acid methyl ester system," *Chem. Rev.*, vol. 113, pp. 3734–3765, 2013.
- [32] L. Chang, H. Lademann, J.-B. Bonekamp, K. Meerholz, and A. Moulé, "Effect of trace solvent on the morphology of P3HT:PCBM bulk heterojunction solar cells," *Adv. Funct. Mater.*, vol. 21, no. 10, pp. 1779–1787, 2011.
- [33] M. Tessarolo, A. Guerrero, D. Gedefaw, M. Bolognesi, M. Prosa, X. Xu, M. Mansour, E. Wang, M. Seri, M. Andersson, M. Muccini, and G. Garcia-Belmonte, "Predicting thermal stability of organic solar cells through an easy and fast capacitance measurement," *Sol. Energy Mater. Sol. Cells*, vol. 141, pp. 240–247, 2015.

- [34] L. Motiei, Y. Yao, J. Choudhury, H. Yan, T. J. Marks, and M. E. Van Der Boom, "Self-propagating molecular assemblies as interlayers for efficient inverted bulk-heterojunction solar cells," *J. Am. Chem. Soc.*, vol. 132, pp. 12528–12530, 2010.
- [35] L.-M. Chen, Z. Hong, G. Li, and Y. Yang, "Recent progress in polymer solar cells: manipulation of polymer: fullerene morphology and the formation of efficient inverted polymer solar cells," *Adv. Mater.*, vol. 21, no. 14–15, pp. 1434–1449, 2009.
- [36] S. H. Park, A. Roy, S. Beaupre, S. Cho, N. Coates, J. S. Moon, D. Moses, M. Leclerc, K. Lee, and A. J. Heeger, "Bulk heterojunction solar cells with internal quantum efficiency approaching 100%," *Nat. Photonics*, vol. 3, no. 5, pp. 297–303, 2009.
- [37] K. O. Sylvester-Hvid, T. Ziegler, M. K. Riede, N. Keegan, M. Niggemann, and A. Gombert, "Analyzing poly(3-hexylthiophene):1-(3-methoxy-carbonyl)propyl-1-phenyl- (6,6) C₆₁ bulk-heterojunction solar cells by UV-visible spectroscopy and optical simulations," *J. Appl. Phys.*, vol. 102, no. 5, pp. 1–9, 2007.
- [38] Y. Shen, K. Li, N. Majumdar, J. C. Campbell, and M. C. Gupta, "Bulk and contact resistance in P3HT: PCBM heterojunction solar cells," *Sol. Energy Mater. Sol. Cells*, vol. 95, no. 8, pp. 2314–2317, 2011.
- [39] G. Li, V. Shrotriya, J. Huang, Y. Yao, T. Moriarty, K. Emery, and Y. Yang, "High-efficiency solution processable polymer photovoltaic cells by self-organization of polymer blends," *Nat. Mater.*, vol. 4,

no. 11, pp. 864–868, 2005.

- [40] A. F. Eftaiha, J. Sun, G. Hill, and G. C. Welch, "Recent advances of non-fullerene, small molecular acceptors for solution processed bulk heterojunction solar cells," *Mater. Chem. A*, vol. 2, pp. 1201–1213, 2014.
- [41] C. Brabec, A. Cravino, D. Meissner, S. Sariciftci, T. Fromherz, M. Rispens, L. Sanchez, J. Hummelen, S. Serdar, T. Fromherz, M. Rispens, L. Sanchez, and J. Hummelen, "Origin of the open circuit voltage of plastic solar cells," *Funct. Mater.*, vol. 11, no. 5, pp. 374–380, 2001.
- [42] R. Kroon, M. Lenes, J. Hummelen, P. Blom, and B. de Boer, *Small bandgap polymers for organic solar cells (polymer material development in the last 5 years)*, *Polymer. Rev.*, vol. 48, no. 3, pp. 531-582, 2008.
- [43] D. Veldman, S. Meskers, and R. Janssen, "The energy of charge-transfer states in electron donor-acceptor blends: insight into the energy losses in organic solar cells," *Adv. Funct. Mater.*, vol. 19, no. 12, pp. 1939–1948, 2009.
- [44] H. Yip and A. K. Jen, "Recent advances in solution-processed interfacial materials for efficient and stable polymer solar cells," *Energy Environ. Sci.*, vol. 5, pp. 5994–6011, 2012.
- [45] L. Wu, H. Zang, Y. C. Hsiao, X. Zhang, and B. Hu, "Origin of the fill

- factor loss in bulk-heterojunction organic solar cells," *Appl. Phys. Lett.*, vol. 104, no. 15, 153902, 2014.
- [46] S. Cowan, N. Banerji, W. Leong, and A. Heeger, "Charge formation, recombination, and sweep-out dynamics in organic solar cells," *Adv. Funct. Mater.*, vol. 22, no. 6, pp. 1116–1128, 2012.
- [47] C. Proctor, M. Kuik, and T. Nguyen, "Charge carrier recombination in organic solar cells," *Prog. Polym. Sci.*, vol. 38, no. 12, pp. 1941–1960, 2013.
- [48] M. L. Jones, R. Dyer, N. Clarke, and C. Groves, "Are hot charge transfer states the primary cause of efficient free-charge generation in polymer:fullerene organic photovoltaic devices? A kinetic Monte Carlo study.," *Phys. Chem. Chem. Phys.*, vol. 16, no. 38, pp. 20310–20320, 2014.
- [49] B. Kippelen and J.-L. Brédas, "Organic photovoltaics," *Energy Environ. Sci.*, vol. 2, no. 3, pp. 241–332, 2009.
- [50] A. J. Ferguson, N. Kopidakis, S. E. Shaheen, and G. Rumbles, "Dark carriers, trapping, and activation control of carrier recombination in neat P3HT and P3HT:PCBM blends," *J. Phys. Chem. C*, vol. 115, no. 46, pp. 23134–23148, 2011.
- [51] R. A. Street and M. Schoendorf, "Interface state recombination in organic solar cells," *Phys. Rev. B*, vol. 81, 205307, 2010.

- [52] M. Kuik, G.-J. Wetzelaer, H. Nicolai, N. I. Craciun, D. De Leeuw, and P. Blom, "25th Anniversary article: charge transport and recombination in polymer light-emitting diodes.," *Adv. Mater.*, vol. 26, no. 4, pp. 512–31, 2014.
- [53] J. Wang and B. Qi, "Fill factor in organic solar cells," *Phys. Chem. Chem. Phys.*, vol. 15, no. 23, pp. 8972–8982, 2013.
- [54] A. Wagenpfahl, C. Deibel, and V. Dyakonov, "Organic solar cell efficiencies under the aspect of reduced surface recombination velocities," *IEEE J. Sel. Top. Quantum Electron.*, vol. 16, no. 6, pp. 1759–1763, 2010.
- [55] C. Deibel, A. Wagenpfahl, and V. Dyakonov, "Influence of charge carrier mobility on the performance of organic solar cells," *Phys. Status Solidi - Rapid Res. Lett.*, vol. 2, no. 4, pp. 175–177, 2008.
- [56] S. Albrecht, S. Janietz, W. Schindler, J. Frisch, J. Kurpiers, J. Kniepert, S. Inal, P. Pingel, K. Fostiropoulos, N. Koch, and D. Neher, "Fluorinated copolymer PCPDTBT with enhanced open-circuit voltage and reduced recombination for highly efficient polymer solar cells," *J. Am. Chem. Soc.*, vol. 134, no. 36, pp. 14932–14944, 2012.
- [57] W. Graupner, G. Leditzky, G. Leising, and U. Scherf, "Shallow and deep traps in conjugated polymers of high intrachain order," *Phys. Rev. B*, vol. 54, no. 11, p. 7610, 1996.

- [58] H. Cheng, W. Lin, and F. Wu, "Effects of solvents and vacancies on the electrical hysteresis characteristics in regioregular poly (3-hexylthiophene) organic thin-film transistors," *Appl. Phys. Lett.*, vol. 94, no. 22, 223302, 2009.
- [59] F. Laquai, D. Andrienko, R. Mauer, and P. Blom, "Charge carrier transport and photogeneration in P3HT: PCBM photovoltaic blends," *Macromol. Rapid Commun*, vol. 36, pp. 1001–1025, 2015.
- [60] J. Simon and J. Andre, *Molecular Semiconductors: Photoelectrical Properties and Solar Cells*. Berlin: Springer-Verlag Berlin Heidelberg, 2011.
- [61] O. Reid, G. Rayermann, D. Coffey, and D. Ginger, "Imaging local trap formation in conjugated polymer solar cells: a comparison of time-resolved electrostatic force microscopy and scanning kelvin probe imaging," *J. Phys. Chem. C*, vol. 114, no. 48, pp. 20672–20677, 2010.
- [62] W. Ma, C. Yang, X. Gong, K. Lee, and A. J. Heeger, "Thermally stable, efficient polymer solar cells with nanoscale control of the interpenetrating network morphology," *Adv. Funct. Mater.*, vol. 15, no. 10, pp. 1617–1622, 2005.
- [63] A. Tournebize, P.-O. Bussière, A. Rivaton, J.-L. Gardette, H. Medlej, R. C. Hiorns, C. Dagon-Lartigau, F. C. Krebs, and K. Norrman, "New insights into the mechanisms of photodegradation/stabilization of P3HT: PCBM active layers using

poly(3-hexyl-d13-thiophene)," *Chem. Mater.*, vol. 25, no. 22, pp. 4522–4528, 2013.

CHAPTER 3

DEGRADATION OF ORGANIC PHOTOVOLTAICS

3.1 Introduction

Degradation in OPVs leads to a reduction in device performance [1]. Degradation can occur in the active layer [2], at the electrodes [1], or the electrode-organic [1], [3] and organic-organic interfaces [3].

Degradation is a complex process [4], [5] as several mechanisms can occur simultaneously, in different parts of the device, at different rates. Some of the processes are fast, and some are slow, making it very difficult to track all of the mechanisms during the lifetime of the device. The challenge is to isolate the main effects that limits device lifetime.

The key factors that can induce different degradation mechanisms in OPVs are illustrated in Figure 3.1. This chapter briefly explains these processes, such as diffusion of molecular oxygen, water, and chemical degradation that reduce the device performance.

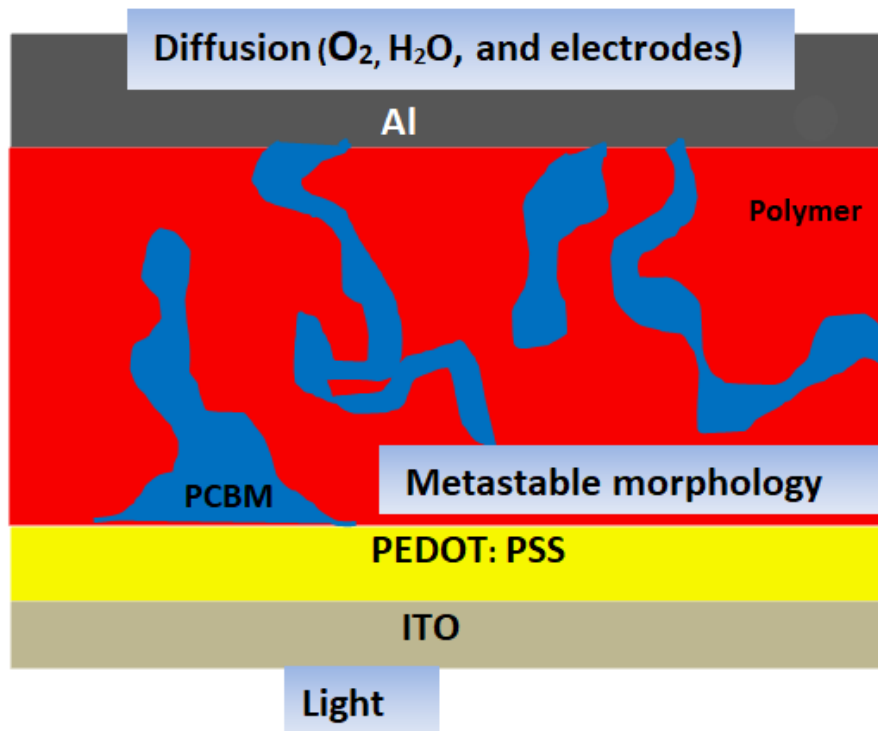


Figure 3.1. Different factors that cause degradation in an OPV device.

3.2 Oxygen-induced degradation

Many studies have found that oxygen is a source of performance degradation in OPVs [6][8]. Norrman et al. [9] demonstrated that oxygen molecules could diffuse into a device through microscopic pinholes in the Al electrode. In their study, they used materials that do not contain oxygen in the active layer (Al/C₆₀/C₁₂-PSV/PEDOT: PSS/ITO), and demonstrated that pinholes appeared in the center of protrusions that were formed on the outer surface of the Al electrode. They found that oxygen could diffuse through these holes so that, under illumination of simulated sunlight (1000 W/m²), photo-oxidation of the C₆₀ occurred. This reaction caused the material to expand in all directions, leading to degradation [9]. The holes and protrusions were observed using Scanning Electron Microscopy (SEM). Hermenau et al. also supported the

idea that oxygen diffuses through pinholes in the aluminium electrode when studying ITO/MeOTPD: C₆₀F₃₆/ZnPc: C₆₀/C₆₀/BPhen/Al devices using time-of-flight secondary ion mass spectrometry (TOF-SIMS) with isotopic labeling H₂¹⁸O and ¹⁸O₂ [10].

Many studies show that oxygen causes degradation of the organic materials in OPVs [11], [12]. One of the research groups who were interested in the impact of oxygen on the degradation of solar devices, and published many papers in this field, is Kerbs et al. For one of their experiments, they made encapsulated and non-encapsulated devices with structures of ITO/ZnO/PCBM: P3HT/PEDOT: PSS/Ag. They placed the devices in a dry atmosphere consisting of ¹⁸O₂: N₂ (1 atm, 0% RH), and a humid atmosphere composed of H₂¹⁸O (1 atm N₂, 65% RH) [12]. They found that the performance of encapsulated devices was degraded significantly by oxygen (T₂₀ ~ 360 h and 68 h in water and oxygen respectively), while both oxygen and water caused considerable degradation in non-encapsulated devices (T₂₀ ~ 1.9 h and 0.1 h in water and oxygen respectively). T₂₀ here represents the time taken for performance to fall to 80% of its initial value [12]. In another study, the same authors found that oxygen reacts with the Al electrode, forming Al oxide (Al₂O₃) which acts as an insulating layer at the Al/organic layer interface [7]. This insulating layer causes a barrier to carrier injection [13], leading to an S-shaped J–V curve and degraded device performance [7]. Furthermore, the penetration of oxygen occurs whether the device is illuminated or kept in the dark [7]. Norrman and Krebs observed that, when kept in the dark, high levels of oxygen molecules and aluminium

oxide were found near the Al/organic layer interface [7], [8]. This was known by measuring the $^{18}\text{O}_2$ isotope content to the ^{16}O ($^{18}\text{O}^-/^{16}\text{O}^-$ ratio) which was found to be ~ 2.5 , a value higher than the expected theoretical ratio of 0.2%. In the same study, authors found the presence of oxygen and oxygen-containing species such as (C_2O^- , C_2HO^- , C_4O^- and C_4HO^-) in the organic layer when the devices were illuminated (1000Wm^{-2}) [8]. This supported the idea that photo-oxidation of conjugated materials is induced under illumination. Photo-oxidation is a process where the photogenerated excited state of the polymer transfers energy to oxygen, forming highly reactive superoxides or hydrogen peroxides that attack the polymer [14].

Photo-oxidation has been widely studied in PPV-type polymers [4]. It was found that these materials are sensitive to photo-oxidation, causing fast degradation of device performance [4]. Many studies have attempted to explain how oxygen reacts with organic materials. One explanation proposed the formation of singlet oxygen ($^1\text{O}_2$) in the polymer. This produces reactive oxygen species that are the mechanism by which the OPVs degrade [4]. This process is illustrated in Figure 3.2. The absorption of a photon excites the electron from the lowest energy singlet state (S_0) to the first excited singlet state (S_1) followed by a transition to a triplet state T_1 [15]. Singlet and triplet states are excited states with a net spin of all electrons in the LUMO and the HOMO orbitals of zero or one, respectively [16]. In the presence of oxygen, the energy transfers from the T_1 state to the adsorbed ground triplet state (T_0) of

the molecular oxygen. This leads to the formation of singlet oxygen ($^1\text{O}_2$) which reacts with the vinylene groups and causes chain scission [4].

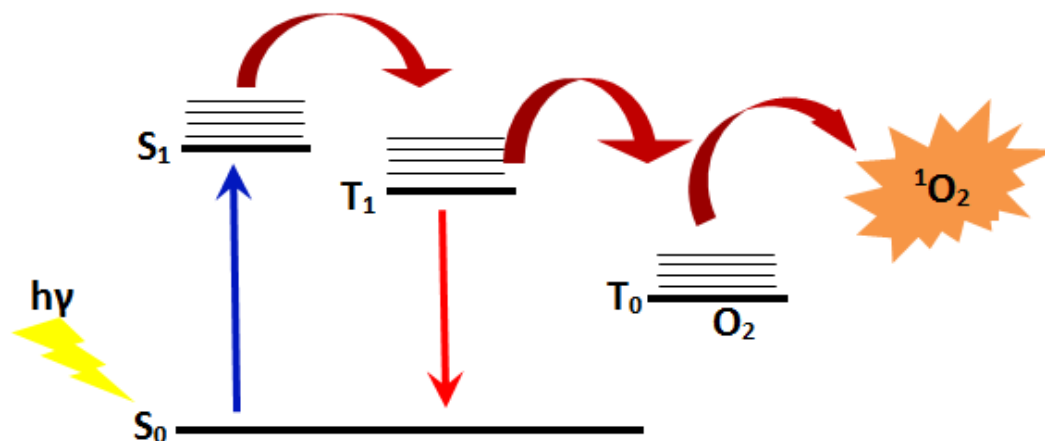


Figure 3.2. The mechanism for the formation of singlet oxygen.

In P3HT, it seems that singlet oxygen is not formed as in PVs because the probability of the formation of a triplet state is low and this state is a necessary condition for forming singlet oxygen [4]. Also, P3HT does not contain vinylene groups, which means that there is another mechanism for forming singlet oxygen in P3HT polymers. However, it was proposed that P3HT tends to form charge-transfer complexes with oxygen instead of singlet oxygen, creating cation and anion radicals ($\text{P3HT}^+ : \text{O}_2^-$) [17]. This weak complex can initiate a chemical reaction in the polymer, causing device degradation. The mechanism of this chemical degradation will be explained in section 3.7. Matthieu et al. found that singlet oxygen $^1\text{O}_2$ was not the main reason for photo-oxidation in P3HT [18]. In addition, it was reported that photo-oxidation of P3HT in the presence of oxygen and under irradiation might cause a disappearance of the alkyl groups and thiophene rings, leading to the formation of

numerous oxidized species [2]. Indeed, many studies investigated the effect of oxygen in devices based on P3HT: PCBM. For example, Guerrero et al. investigated the degradation induced by oxygen in the structure ITO/PEDOT: PSS/P3HT: PCBM/Ca/Ag [19]. They used oxygen treatment by passing dry air passed through the film for two hours before and after cathode deposition. They found that chemical degradation was induced after the cathode was deposited and the cell had been completed. They observed that, due to oxygen exposure, a $\text{P3HT}^+ : \text{O}^{2-}$ complex and a calcium oxide layer (CaO) were formed simultaneously in the complete devices [19]. Formation of the $\text{P3HT}^+ : \text{O}^{2-}$ complex reduced the concentration of P3HT, causing a reduction in light absorption. It was also found that the oxidation of P3HT reduced both J_{sc} and V_{oc} [19]. In addition, the formation of calcium oxide is an entirely irreversible process and leads to a significant drop in the FF [19]. In another study, Rees et al. reported that PCBM also reacts with oxygen and forms species with up to eight oxygen atoms, leading to increasing electron traps and decreasing electron mobilities [20]. Supporting this result, Schafferhans et al. concluded that oxygen generated trap states in P3HT: PCBM devices caused by exposure to oxygen in the dark resulted in a low J_{sc} [21].

3.3 Water-induced degradation

Water is another important cause of degradation in OPVs [9], [22]. It can penetrate the device through the Al electrode whether the device is illuminated or stored in darkness [6]. Kerbs et al. found that water penetrated all the way from the aluminium electrode to the indium tin

oxide (ITO) electrode, causing homogeneous degradation in all the interfacial layers between the Al and the active layer, while oxygen was found to induce inhomogeneous degradation [6]. Diffusion of oxygen and water into the device is an important issue because identifying the main route for their ingress will help device lifetime to be increased by removing or reducing that pathway.

Different studies have shown that diffusion of water was through grain boundaries in the Al cathode instead of through pinholes or at the edges of the device [1], [10]. Norrman et al. showed that oxygen molecules diffuse through microscopic pinholes in the Al electrode [9]. Hermenau et al. also concluded that oxygen and water diffuse through pinholes in the aluminium, thus causing oxidation of the organic materials [10].

Various suggestions have emerged about the main route for water to enter the device. When considering the Norrman et al. suggestion that the main entrance of water is through pinholes on the surface of the Al [9], the Al thickness used for these studies is around 22 nm [9]. This is small compared with common electrode thicknesses of 80- 150 nm. This means that the formation of pinholes may not be the main entrance for water. Voroshazi et al. [23] found that the main entrance route for water is, in fact, the edges of the device. However, a recent study showed that the major reason for degradation is the diffusion of water into the device through large defects (radius > 0.3 μm) which appeared on the Al electrode and it did not ingress through aluminium grain boundaries [24]. In addition, it was suggested that the diffusion of oxygen is much slower

than the diffusion of water and, therefore, water might be the principal reason for degradation [24]. Figure 3.3 illustrates the different mechanisms for the diffusion of oxygen and water molecules into OPV devices.

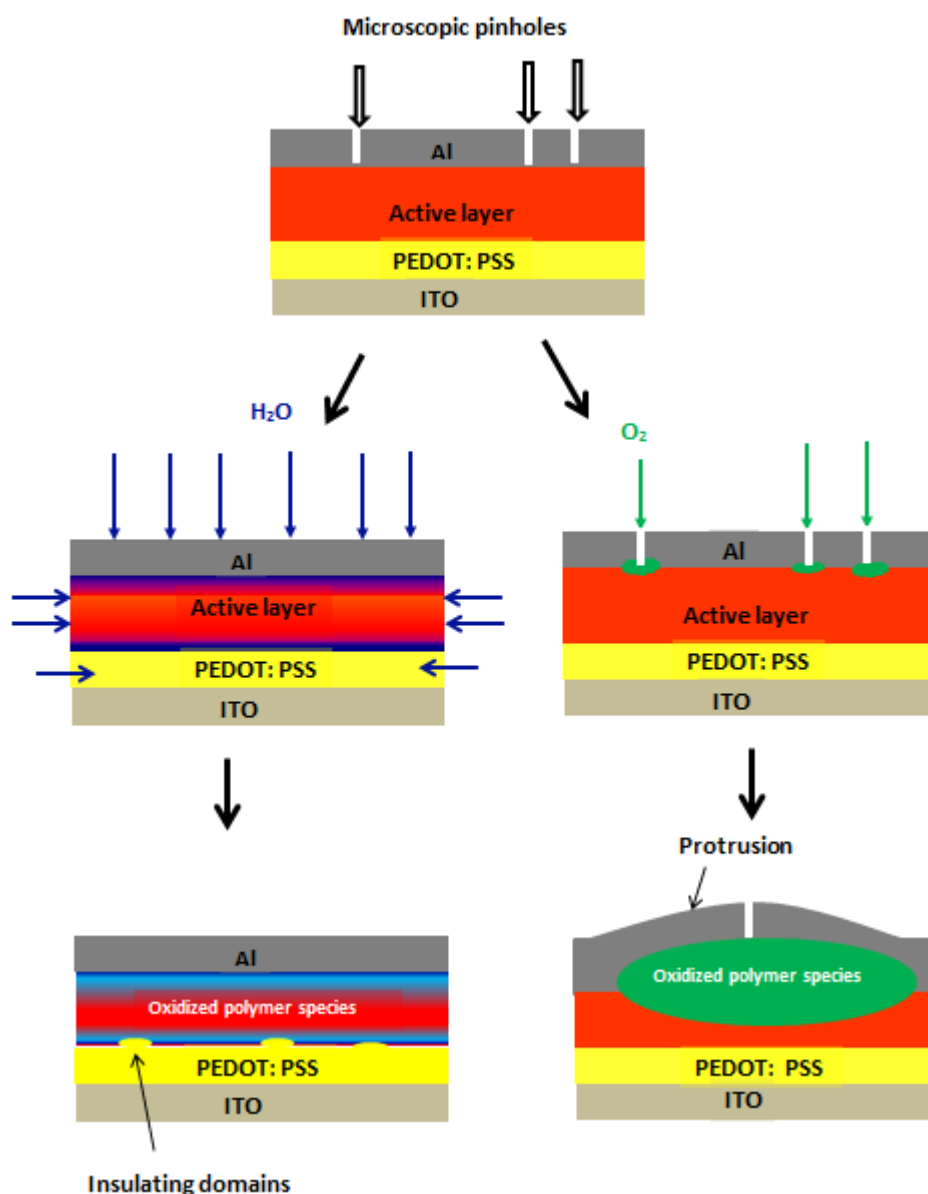


Figure 3.3. Schematic diagram illustrating the different pathways for the ingress of oxygen and water molecules into an OPV device.

The impact of water diffusion into OPV devices has been studied. Kawano et al. found that the hole transporting layer Poly(3,4-ethylene

dioxythiophene)-poly(styrene sulfonate) PEDOT: PSS is the main channel for water-induced degradation [25]. It is known that PEDOT: PSS is a hygroscopic material [23], therefore it is sensitive to water. In the Kawano et al. experiment, poly[2-methoxy-5-(30,70-dimethyloctyloxy)-1,4-phenylenevinylene] (MDMO-PPV: PC₆₁BM) devices were made on ITO glass, with and without a PEDOT: PSS layer, and were exposed to a humid atmosphere. Fast degradation was observed in devices with PEDOT: PSS and no significant degradation was seen in devices without PEDOT: PSS during the duration of the experiment (10 hours) [25]. It was concluded that degradation was associated with water absorption into the PEDOT: PSS layer leading to inhomogeneous degradation at the PEDOT: PSS/active layer interface and an increase in the series resistance with time [25]. These workers concluded that absorption of water by PEDOT: PSS causes the formation of insulating domains at the PEDOT: PSS/active layer interface (Figure 3.3) which increase the injection barrier, resulting in a rapid drop in J_{sc} and FF [25]. In addition, Voroshazi et al. reported that water could diffuse from the PEDOT: PSS layer towards the Al electrode, causing rapid oxidation of the aluminium metal and leading to fast degradation of the device performance [23].

Norrman et al. used isotopic labeling ($H_2^{18}O$ and $^{18}O_2$) to map the effect of water and oxygen on devices based on a bulk heterojunction of zinc phthalocyanine (ZnPc) and C_{60} [10]. They observed that water is significantly more harmful than oxygen [10]. Other studies have supported this suggestion [1], [25]. Furthermore, the presence of light was observed to accelerate water induced degradation [10].

It has been observed that the diffusion of water into the active layer increases recombination, which lowers the charge carrier density [26]. Bauld et al. studied the degradation of P3HT: PCBM devices in a humid environment of 70% at 70° C for times of up to 70 hours using techniques, such as Rutherford backscattering (RBS) and electron spin resonance (ESR) [27]. In their experiment, they did not notice any increase in oxygen and water content in the devices during the experiment; however, they did observe a strong change in the surface roughness. They found that water increases the defects in P3HT and PCBM, and at the interface between P3HT and PCBM. These defects can act as traps and increase the electron-hole recombination rate [27].

Encapsulation may be appropriate to protect devices from the diffusion of water and oxygen. However, it was found that even if devices were encapsulated and kept away from water and oxygen, they still degraded when illuminated [28].

3.4 Light-induced degradation

Light is another significant factor that can accelerate the degradation of OPVs [10]. As mentioned in previous sections, exposure to water and oxygen in the presence of light induces faster degradation than in the absence of light. Light exposure can induce photochemical and photophysical deterioration [26]. Photochemical degradation is a result of chemical changes in the active layer due to irradiation [11], which occurs whether the device is in an inert or ambient environment. A chemical reaction in the presence of light and oxygen is called a photo-oxidation

reaction. Photo-physical reactions lead to changes in the electronic and mechanical properties of the active layer due to photo-degradation [26].

Photo-degradation has been widely studied in order to understand the effect of light on the lifetime of OPVs. Rivaton et al. [11] studied the effect of light on thin films of MDMO-PPV, P3HT and their blends with PCBM in the presence of oxygen. A noticeable decrease in the absorption band of MDMO-PPV during irradiation for 120 minutes was found. These workers proposed a reduction in conjugation length resulting in photo-bleaching (decrease of light absorption) of the polymer. The authors also used IR spectra (as discussed in Chapter 4), and observed a loss of several functional groups in the polymers, such as ether groups and vinylene. At the same time, new absorption bands in the carbonyl and hydroxyl regions appeared. These changes in the IR spectra resulted from oxidation of the polymers. The authors also carried out an experiment in the absence of oxygen and found that the degradation process was slowed by a factor 1000 [11]. It was proposed that exposure to light in the absence of oxygen could cause a photochemical reaction in the polymer causing a change in the structure and chain scission [11]. It was also observed that irradiation of P3HT and P3HT: PCBM in ambient air lead to a decrease in the intensity of the visible absorption band and a noticeable change in the IR spectrum of P3HT. Carbonyl and hydroxyl groups were also found [11]. The oxidation of a sulfur atom in the thiophene ring leads to the loss of π -conjugation, and bleaching of the polymer. However, in the absence of oxygen, no significant changes were observed in the IR spectra even after long irradiation times. This

indicates that the P3HT: PCBM blend is more stable than MDMO-PPV: PCBM [11]. In other work, it was reported that films of P3HT are photo-oxidized rapidly with complete bleaching after 700 h [29], and adding PCBM slows down this degradation process [11]. In addition, it was found that the rate of degradation, when exposed to blue light, was faster than that in red light, and a further increase in degradation occurred when the intensity of the blue light was increased [10]. On the other hand, it was found that UV radiation may enhance the photo-degradation of P3HT more than visible light exposure [30]. Rivaton et al. proposed that the degradation mechanism under UV radiation is different than under visible light [30].

In P3HT: PCBM devices, the rate of degradation in an inert environment under illumination was significantly higher than for devices measured in an inert, dark environment [3]. Manceau et al. found that the absorbance of P3HT reduced to nearly zero after 100 h of UV-visible light irradiation ($295 < \lambda < 800$ nm) [2]. Although most studies found that light exposure accelerated the degradation, Karak et al. found that light illumination caused a change in the chemical and electrical properties of pentacene and CuPc-based OPVs [31]. After exposure to solar radiation for several hours, pentacene was found to be more stable than CuPc. The devices showed short lifetime because UV radiation caused a quick degradation in J_{sc} and induced a change in the shape of the J-V curve under positive bias [31]. The authors have suggested that photo-degradation is due to the formation of a large number of defect states in the active layer which can increase the rate of recombination and so

decrease the performance of the device. A significant change in the film morphology was also observed after a few hours of UV radiation [31].

Most studies found that photo-oxidation occurs in the donor while very few studies showed that the acceptor PCBM can oxidize in the presence of light and oxygen [20]. Oxidization of PCBM creates deeper trap states which reduce the electron mobility [20]. Street et al [32] studied the effect of X-ray illumination on poly (carbazole-dithienyl-benzothiadiazole): phenyl C₇₀-butyric acid methyl ester (PCDTBT:PC₇₀BM) and P3HT: PCBM cells. They found that defect states in the active layer result from the breaking of the C-H bonds in the alkyl chains or thiophene rings, and that the released H atoms transfer to a C atom in the conjugated polymer backbone. They found that light in the absence of oxygen and water causes significant damage to the device performance due to the increased numbers of traps acting as recombination centers [32].

3.5 Degradation induced by diffusion of metal electrodes

The electrodes are another important factor that contributes to the rapid degradation in OPVs. There are two electrodes with different work functions used in OPV devices: the cathode and the anode. In the cathode, a low work function metal such as Al, Ca or Ag is used, while for the anode, a transparent, high work function material such as ITO is usually used [33]. Device lifetime was found to strongly depend on the cathode/organic layer interface [25].

Different studies have reported that low work function metals are sensitive to water and oxygen and are easily oxidized in ambient conditions [4], [7], [33], [34]. The diffusion of water and oxygen into the metal forms a thin insulating metal oxide barriers at the interface [4], [34]. This layer reduces the efficiency of charge carrier collection [7], [33]. In other work, it has also been shown that the thickness of the metal oxide layer plays a significant role in the degradation [1]. If the metal oxide layer is too thin (2-3 nm), the transport of electrons may not be blocked and the device lifetime may not decrease. However, if the thickness of oxide layer doubles, it might prevent electron transport and hence degrade the device performance [1].

Diffusion of metal into the active layer is another pathway for degradation. It was found that the metal can react with the organic material forming organic-metal compounds sufficient to cause degradation [4]. Lögdlund et al. proposed that there is a direct reaction between PPV type polymers and aluminium, which results in the formation of Al-C bonds at the interface [4]. The organo-aluminium compounds are highly reactive species that react with any water and oxygen present. The result is a reduction of the vinylene groups and a loss of conjugation in the polymer [4]. A calcium electrode may also diffuse through and react with the organic material, forming C-Ca bonds which then react with oxygen and degrade the device [4]. In addition, materials with a high electron affinity, such as PCBM, may also react with the metal electrode. It was found that C_{60} reacts with alkali metals and forms compounds like K_3C_{60} [4], and it has been proposed that similar reaction could occur with Al [5]. Nishinaga et al. [35] found that Al- C_{60}

interactions and Al-C₆₀ bonding caused a reduction in J_{sc}. The effect of electrode diffusion on device operation is shown schematically in Figure 3.4.

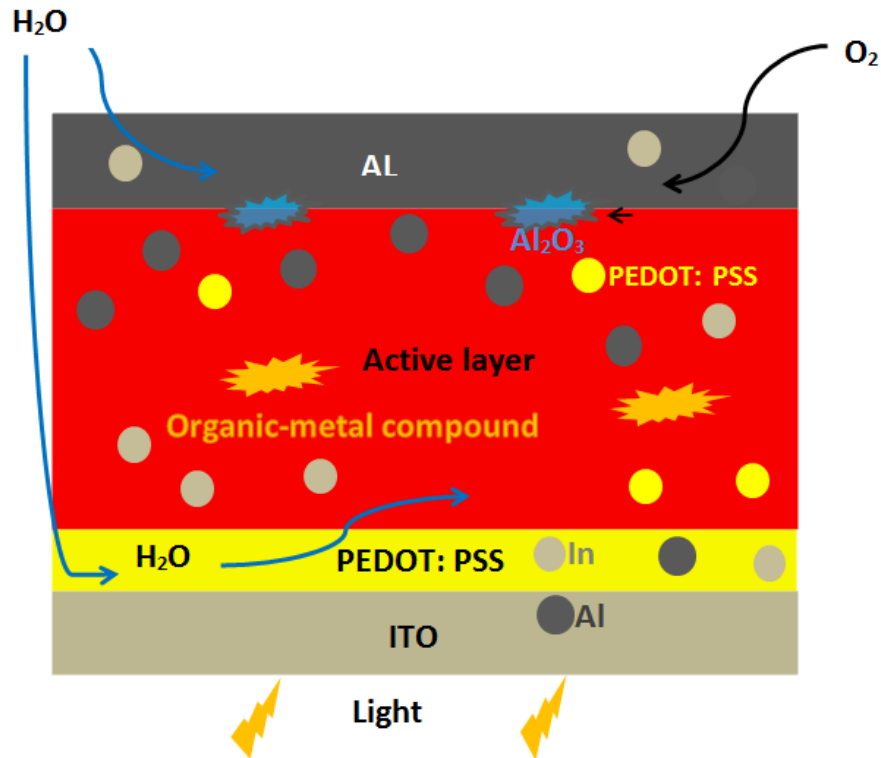


Figure 3.4. Schematic diagram showing metal diffusion and its impact on the active layer.

In other work, Reese et al. investigated the effect of different electrodes on the degradation of devices based on P3HT: PCBM [3]. They used six different electrode types and measured the decay in the performance of the devices in an inert, dark environment for over six weeks. They found that the largest amount of degradation occurred with an Ag electrode. It was suggested that deterioration of Ag at the interface was due to chemical interaction with thiophenes in the P3HT. It was also found that Al/Ca provided the most stable electrode after six weeks. This has been argued to be due to the relative insensitivity of Ca to oxygen [3]. A buffer layer such as Ca or LiF has been added between

the Al electrode and the active layer to protect the cathode from oxidation [1].

Jong et al. [36] investigated the anode electrode and showed that a film of ITO/PEDOT: PSS/PPV stored in air had 1.2% indium in the PEDOT: PSS layer after ten days compared to 0.02 % in the as-prepared sample. It was concluded that the diffusion of indium into the PEDOT: PSS accelerated in the presence of water [36]. However, Kerbs and Norrman found that the indium does not just diffuse into the PEDOT: PSS layer, but continues through all the layers in the device and ends up on the outer surface of the aluminium electrode [7]. It was found that PEDOT: PSS (pH value between 1 and 2) would etch indium from the ITO electrode, leaving it free to diffuse throughout the device and reduce the lifetime [37]. However, Voroshazi et al. demonstrated that the hygroscopic behavior of PEDOT: PSS, and not the acidity, is responsible for device degradation [23]. From this discussion, it was not clear to what extent the etching and diffusion of indium are involved in the degradation process.

The hole transporting layer, PEDOT: PSS, is proposed to be a significant pathway for device degradation, as shown schematically in Figure 3.4. Kawano et al. revealed that the hygroscopic PEDOT: PSS layer absorbs water from the atmosphere leading to an increase in sheet resistance that results in rapid drops in J_{sc} and FF [4]. Moreover, PEDOT: PSS was found to induce degradation in P3HT: PCBM devices by decreasing the absorbance and causing the formation of aggregates in the active layer [33]. In other work, Norrman et al. [9] observed the

formation of small particles, which appear to have a crystal structure, on the surface of C₁₂-PSV/PEDOT: PSS/ITO after storage in darkness and air for several months. The authors suggested that the particles are PSS derivatives. The PSS may diffuse and react with different materials in the device with a reaction called oxido-de-sulfonate-substitution forming the phenolate that can subsequently react with PSS, forming two PSS chains linked together via a sulfonic ester group [9].

3.6 Metastable morphology induced degradation

The device performance depends on the organization of the active layer. Nanophase separation of the active layer into an interpenetrating network of donor and acceptor materials is required for both exciton dissociation and charge transport. However, this structure may not be stable, and the phase separation can change with time due to the mobility of the organic materials [4]. Aggregates and unfavorable large phase separations can form, leading to degradation in the performance of the OPV [38]. Park et al. studied the morphological degradation of P3HT: PCBM by annealing the devices at 25°C and 80°C in an inert environment [38]. Aggregation of PCBM on the surface of the P3HT: PCBM blended film was observed. This sharply decreased the performance of the OPVs was due to the reduced efficiency of exciton dissociation and charge transfer, which resulted from a reduction in the donor-acceptor interfacial area [38]. Bertho et al. [39] also investigated morphological degradation in the active layer of OPVs due to thermal treatment. In their experiment, they made devices based on three different materials: MDMO-PPV: PCBM,

P3HT: PCBM, and high glass transition temperature polymer 'High T_g PPV': PCBM. The devices were stored in the dark. During annealing, a decrease in J_{sc} was observed. The degradation in the performance was attributed to a change in the morphology of the active layer. A rapid formation of PCBM clusters in MDMO-PPV was observed and fiber-like crystalline structure of P3HT, after annealing at 110°C for 16 hours. This condition of annealing for a long time is not an operating condition. However, Bertho et al. used this to test the impact of morphology on the performance. They observed that the aggregation of PCBM reduced the interfacial area between the electron acceptor and donor regions, which resulted in a low photocurrent [39].

There is a further factor that induces physical degradation, namely the glass transition temperature of the polymers. By comparing the three materials that Bertho et al. used in their experiments, 'High T_g PPV' material exhibited a more stable absorption spectrum during their long thermal treatment (16 hours of annealing at 110°C) than P3HT and MDMO-PPV. It was suggested that the higher glass transition temperature of the 'High T_g PPV' made its matrix firmer, and this reduced the diffusion and segregation of PCBM, leading to less degradation [39]. This suggestion was supported by different studies which showed that the morphology of active layers is unstable if the environmental temperature is higher than the T_g of the polymers [40], [41].

Finally, Bauld et al. observed an extensive change in the morphology of a P3HT: PCBM blend film after exposure to moisture for 10 hours. They observed a coalescence of several P3HT and PCBM

nanocrystals into larger, smoother, and presumably amorphous, domains [27]. From the literature, it was concluded that physical degradation in the active layer had not been widely investigated. It seems that other factors cause a physical change in the active layer. Most studies are focused on the effect of annealing temperature on the degradation of the morphology and only rarely have studies investigated other factors.

3.7 Degradation mechanisms in P3HT: PCBM

Various degradation mechanisms occur inside the OPV device at different rates. Although degradation is well studied, there have been few studies which investigate the degradation mechanisms in OPVs, and not all mechanisms have been identified. The mechanism that has been widely investigated is the formation of oxidation products (photochemical), which appears to be the major mechanism that causes degradation in these devices. This section attempts to give a brief review of the degradation mechanisms in specifically devices based on P3HT: PCBM.

3.7.1 Photochemical mechanisms in P3HT

Photochemical degradation mechanisms in P3HT were elucidated under illumination in the presence of oxygen. Two different processes were proposed. The first, oxidation by the formation of singlet oxygen [42], and the second, oxidation by a free-radical chain mechanism [18]. Singlet oxygen may be formed on the dissociation of the excited state of the charge transfer complex, and form an unstable radical species which attacks the thiophene ring, and then decomposes into carbonyl, olefinic

and sulfine derivatives [28]. It was proposed that the loss of conjugation lead to the bleaching of the material without affecting the side chains [18]. A radical chain mechanism was demonstrated by Matthieu et al., who showed that singlet oxygen is not the main factor responsible for the photo- degradation of P3HT [43]. They believed that direct attack on the thiophene ring is not the main reason for degradation, which instead starts from the side chain [28].

A degradation mechanism was also illustrated by Rivaton et al., who proposed that the photochemical behavior of the chromophoric species (moieties that absorb visible spectrum energy) involved in the chain radical oxidation of P3HT is a key factor in the degradation mechanism that was proposed by Matthieu et al. [30]. Here, the summary of the photochemical mechanism is divided into three steps:

Step 1: Side chain oxidation

The absorption of UV light is sufficient to break the single covalent bonds [30]. When P3HT absorbs UV photons, macro alkyl radicals are formed, which can initiate oxidation of the polymer. The oxidation takes place in the α -carbon atoms of the side chain, forming hydroperoxides which result from oxygen fixation and hydrogen abstraction on the carbon atom in the α -position to the thiophene ring [18]. O-O bond hemolysis in hydroperoxides and generates two free reactive radicals: alkoxy and hydroxy. Rivaton et al. found that the oxidation process after this step does not depend on irradiation, so that even if P3HT does not

absorb any photons, the oxidation process will continue to form sulfinate groups [30].

Step 2: Radical reactions

Radicals can react and produce different products through three routes: First, hydrogen abstraction of alkoxy radicals may produce α -unsaturated alcohols [18]. Second, aromatic ketones [18], [30] can be produced by the cage reaction of the alkoxy with hydroxyl radicals [18]. Such ketonic groups were found to be photo-unstable when the irradiation was at $\lambda < 400$ nm, followed by oxidation and the formation of aromatic carboxylic acid. This reaction also produces alkyl radicals that are oxidized into aliphatic carboxylic acids [18], [30]. The third product was an aromatic aldehyde from the B-Scission reaction, but these species are unstable and rapidly oxidize to carboxylic acids [18]. B-scission may produce alkyl radicals that transform into aliphatic carboxylic acids. Anhydride groups are also generated upon oxidation from the condensation of carboxylic acids [18].

Step 3: Sulfur atom oxidation

The oxidation of the sulfur atom of the thiophene ring by hydroxyl radicals may occur [18]. This process is thought to proceed in three steps. First sulfur oxidized to sulfoxides, then to sulfones that finally decompose into sulfinate esters [18]. XPS and UV-visible spectroscopy showed the existence of sulfinate esters, indicating that the thiophene ring was broken [43]. The final degradation product (sulfinate esters)

causes a disruption of the π -conjugation in P3HT, resulting in low light absorption [43].

Overall, it was clear that most studies agreed that during degradation, the alkyl groups and thiophene rings disappeared, leading to a loss of π -conjugation and reduction in UV-visible absorbance. However, some studies showed that the thiophene rings and alkyl chain disappeared together [2], [18] while others showed a high-intensity absorption due to thiophene rings at first which disappeared with increasing aging time [30]. It seems that the rate of disappearance of the thiophene rings depends on certain conditions such as the temperature, the diffusion rate of oxygen, or the intensity and wavelength of light. Secondly, it was shown that UV irradiation was responsible for the initiation of oxidation reactions. However, the degradation occurred even in dark conditions, but at a slower rate [9]. This suggests that either there is another factor contributing to the oxidization of the materials, or another mechanism may occur.

3.7.2 Photochemical degradation of PCBM

Different studies have shown that PCBM increases the stability of P3HT [2], [30] and slows the degradation, which means that the degradation mechanism in the presence of PCBM may be different. It was found that exposing a P3HT: PCBM film to UV light can cause the oxidation of PCBM [30]. The oxidized molecules act as deep traps and therefore decrease the electron mobility and cause degradation [30]. Rivaton et al. observed a noticeable increase of carbon content

originating from PCBM in P3HT: PCBM films [30]. Reese et al. also observed a significant fraction of oxidized PCBM in P3HT: PCBM films after aging the films in air for 1000 h and supposed that the oxidized materials are creating traps inside the PCBM domains under illumination, causing a decrease in the conductivity [20]. Details about the degradation mechanism of PCBM is still under investigation [20]. One possible mechanism that may occur in the presence of oxygen and light is the breaking of the double bond between oxygen molecules in the PCBM (the chemical structure of PCBM and P3HT shown in Chapter 4, Figure 4.2), and creation of a single bond [20]. This leads to a C-O-C component which forms oxidized species that affect the electronic structure and optical properties of PCBM. The oxidized PCBM molecules that are adjacent to the polymer molecules can then initiate the oxidation reaction on the side chain and thiophene rings. The change in the chemical structure of the polymer can reduce the values of all the electrical parameters, and finally, the S shape in the J-V curve will appear, indicating the death of the device.

3.8 Conclusion

This Chapter has explained different factors that caused various degradation mechanisms. Different degradation mechanisms occur in different parts of OPV device. According to the literature, Water and oxygen are a significant cause of performance degradation in OPVs. They can diffuse into OPV device through Al electrode and PEDOT: PSS layer. Presence of water and oxygen inside the active layer may cause oxidation

reactions and form an insulating layer at cathode and PEDOT: PSS/ active layer interfaces leading to degradation of the device performance.

This thesis investigates the degradation induced by water and oxygen. Oxidation reaction that may occur due to diffusion of water and oxygen is studied in Chapter 5. Ternary blend film and lamination process are used (Chapter 6, 7 and 9) to reduce the diffusion of water and oxygen through PEDOT: PSS and Al electrode into P3HT: PCBM devices to slow down the degradation process.

3.9 References

- [1] H. Cao, W. He, Y. Mao, X. Lin, K. Ishikawa, J. Dickerson, and W. Hess, "Recent progress in degradation and stabilization of organic solar cells," *J. Power Sources*, vol. 264, pp. 168–183, 2014.
- [2] M. Manceau, S. Chambon, A. Rivaton, J. L. Gardette, S. Guillerez, and N. Lematre, "Effects of long-term UV visible light irradiation in the absence of oxygen on P3HT and P3HT: PCBM blend," *Sol. Energy Mater. Sol. Cells*, vol. 94, no. 10, pp. 1572–1577, 2010.
- [3] M. Reese, A. Morfa, M. White, N. Kopidakis, S. Shaheen, G. Rumbles, and D. Ginley, "Pathways for the degradation of organic photovoltaic P3HT: PCBM based devices," *Sol. Energy Mater. Sol. Cells*, vol. 92, no. 7, pp. 746–752, 2008.
- [4] Mikkel Jørgensen, K. Norrman, and F. C. Krebs, "Stability/degradation of polymer solar cells," *Sol. Energy Mater. Sol. Cells*, vol. 92, no. 7, pp. 686–714, 2008.
- [5] V. S. Balderrama, M. Estrada, P. L. Han, P. Granero, J. Pallarés, J. Ferré-Borrull, and L. F. Marsal, "Degradation of electrical properties of PTB1: PCBM solar cells under different environments," *Sol. Energy Mater. Sol. Cells*, vol. 125, pp. 155–163, 2014.
- [6] K. Norrman, S. A. Gevorgyan, and F. C. Krebs, "Water-induced degradation of polymer solar cells studied by H 2 18 O labeling," *ACS Appl. Mater. Interfaces*, vol. 1, no. 1, pp. 102–112, 2009.

- [7] K. Norrman and F. C. Krebs, "Analysis of the failure mechanism for a stable organic photovoltaic during 10 000 h of Testing," *Prog. Photovolt Res. Appl.*, vol. 15, pp. 697–712, 2007.
- [8] K. Norrman and F. C. Krebs, "Lifetimes of organic photovoltaics: Using TOF-SIMS and $^{18}\text{O}_2$ isotopic labelling to characterise chemical degradation mechanisms," *Sol. Energy Mater. Sol. Cells*, vol. 90, no. 2, pp. 213–227, 2006.
- [9] K. Norrman, N. B. Larsen, and F. C. F. Krebs, "Lifetimes of organic photovoltaics: Combining chemical and physical characterisation techniques to study degradation mechanisms," *Sol. Energy Mater. Sol. Cells*, vol. 90, no. 5, pp. 2793–2814, Nov. 2006.
- [10] M. Hermenau, M. Riede, K. Leo, S. A. Gevorgyan, F. C. Krebs, and K. Norrman, "Water and oxygen induced degradation of small molecule organic solar cells," *Sol. Energy Mater. Sol. Cells*, vol. 95, no. 5, pp. 1268–1277, 2011.
- [11] A. Rivaton, S. Chambon, M. Manceau, J.-L. Gardette, N. Lemaître, and S. Guillerez, "Light-induced degradation of the active layer of polymer-based solar cells," *Polym. Degrad. Stab.*, vol. 95, no. 3, pp. 278–284, 2010.
- [12] K. Norrman, M. V. Madsen, S. A. Gevorgyan, and F. C. Krebs, "Degradation patterns in water and oxygen of an inverted polymer solar cell," *J. Am. Chem. Soc.*, vol. 132, no. 47, pp. 16883–16892, 2010.

- [13] J. Wang and B. Qi, "Fill factor in organic solar cells," *Phys. Chem. Chem. Phys.*, vol. 15, no. 23, pp. 8972–8982, 2013.
- [14] E. Glowacki, N. Sariciftci, and C. Tang, "Organic solar cells," *Sol. Energy*, pp. 97–128, 2013.
- [15] J. Brédas, J. E. Norton, J. Cornil, and V. Coropceanu, "Molecular understanding of organic solar cells: the challenges," *Acc. Chem. Res.*, vol. 42, no. 11, pp. 1691–1699, 2009.
- [16] B. Kippelen and J.-L. Brédas, "Organic photovoltaics," *Energy Environ. Sci.*, vol. 2, no. 3, pp. 241–332, 2009.
- [17] A. Aguirre, S. C. J. Meskers, R. A. J. Janssen, and H. J. Egelhaaf, "Formation of metastable charges as a first step in photoinduced degradation in p-conjugated polymer: fullerene blends for photovoltaic applications," *Org. Electron. physics, Mater. Appl.*, vol. 12, no. 10, pp. 1657–1662, 2011.
- [18] M. Manceau, A. Rivaton, J.-L. Gardette, S. Guillerez, and N. Lemaître, "The mechanism of photo- and thermooxidation of poly(3-hexylthiophene) (P3HT) reconsidered," *Polym. Degrad. Stab.*, vol. 94, no. 6, pp. 898–907, 2009.
- [19] A. Guerrero, P. P. Boix, L. F. Marchesi, T. Ripolles-Sanchis, E. C. Pereira, and G. Garcia-Belmonte, "Oxygen doping-induced photogeneration loss in P3HT: PCBM solar cells," *Sol. Energy Mater. Sol. Cells*, vol. 100, pp. 185–191, 2012.

- [20] M. O. Reese, A. M. Nardes, B. L. Rupert, R. E. Larsen, D. C. Olson, M. T. Lloyd, S. E. Shaheen, D. S. Ginley, G. Rumbles, and N. Kopidakis, "Photoinduced degradation of polymer and polymer-fullerene active layers: experiment and theory," *Adv. Funct. Mater.*, vol. 20, no. 20, pp. 3476–3483, Oct. 2010.
- [21] J. Schafferhans, A. Baumann, A. Wagenpfahl, C. Deibel, and D. Vladimir, "Oxygen doping of P3HT:PCBM blends: influence on trap states, charge carrier mobility and solar cell performance," *Org. Electron.*, pp. 1693–1700, 2010.
- [22] T. Xiao, F. Fungura, M. Cai, J. W. Andereg, J. Shinar, and R. Shinar, "Improved efficiency and stability of inverted polymer solar cells with a solution-processed BPhen interlayer and polystyrene beads," *Org. Electron. physics, Mater. Appl.*, vol. 14, no. 10, pp. 2555–2563, 2013.
- [23] E. Voroshazi, B. Verreet, A. Buri, R. Müller, D. Di Nuzzo, and P. Heremans, "Influence of cathode oxidation via the hole extraction layer in polymer:fullerene solar cells," *Org. Electron. physics, Mater. Appl.*, vol. 12, no. 5, pp. 736–744, 2011.
- [24] H. Klumbies, M. Karl, M. Hermenau, R. Rösch, M. Seeland, H. Hoppe, L. Müller-Meskamp, and K. Leo, "Water ingress into and climate dependent lifetime of organic photovoltaic cells investigated by calcium corrosion tests," *Sol. Energy Mater. Sol. Cells*, vol. 120, Part B, pp. 685–690, 2014.

- [25] K. Kawano, R. Pacios, D. Poplavskyy, J. Nelson, D. D. C. Bradley, and J. R. Durrant, "Degradation of organic solar cells due to air exposure," *Sol. Energy Mater. Sol. Cells*, vol. 90, no. 20, pp. 3520–3530, 2006.
- [26] V. I. Madogni, B. Kounouhe'wa, A. Akpo, M. Agbomahe'na, S. A. Hounkpatin, and C. N. Awanou, "Comparison of degradation mechanisms in organic photovoltaic devices upon exposure to a temperate and a subequatorial climate," *Chem. Phys. Lett.*, vol. 640, pp. 201–214, 2015.
- [27] R. Bauld, L. M. Fleury, M. Van Walsh, and G. Fanchini, "Correlation between density of paramagnetic centers and photovoltaic degradation in polythiophene-fullerene bulk heterojunction solar cells," *Appl. Phys. Lett.*, vol. 101, no. 10, pp. 1–5, 2012.
- [28] M. Jørgensen, K. Norrman, S. A. Gevorgyan, T. Tromholt, B. Andreasen, and F. C. Krebs, "Stability of polymer solar cells," *Adv. Mater.*, vol. 24, no. 5, pp. 580–612, 2012.
- [29] C. J. Brabec, G. Zerza, G. Cerullo, S. De Silvestri, S. Luzzati, J. C. Hummelen, and S. Sariciftci, "Tracing photoinduced electron transfer process in conjugated polymer/fullerene bulk heterojunctions in real time," *Chem. Phys. Lett.*, vol. 340, no. 3–4, pp. 232–236, 2001.
- [30] A. Tournebize, P.-O. Bussièrre, A. Rivaton, J.-L. Gardette, H. Medlej, R. C. Hiorns, C. Dagrón-Lartigau, F. C. Krebs, and K. Norrman,

- "New insights into the mechanisms of photodegradation/stabilization of P3HT:PCBM active layers using poly(3-hexyl-d₁₃-Thiophene)," *Chem. Mater.*, vol. 25, no. 22, pp. 4522–4528, 2013.
- [31] S. Karak, S. Pradhan, and A. Dhar, "The effects of different atmospheric conditions on device stability of organic small-molecule solar cells under constant illumination," *Semicond. Sci. Technol.*, vol. 26, 95020, 2011.
- [32] R. A. Street, J. E. Northrup, and B. S. Krusor, "Radiation induced recombination centers in organic solar cells," *Phys. Rev. B - Condens. Matter Mater. Phys.*, vol. 85, no. 20, pp. 1–13, 2012.
- [33] V. M. Drakonakis, A. Savva, M. Kokonou, and S. A. Choulis, "Investigating electrodes degradation in organic photovoltaics through reverse engineering under accelerated humidity lifetime conditions," *Sol. Energy Mater. Sol. Cells*, vol. 130, pp. 544–550, 2014.
- [34] M. Wang, F. Xie, J. Du, Q. Tang, S. Zheng, Q. Miao, J. Chen, N. Zhao, and J. B. Xu, "Degradation mechanism of organic solar cells with aluminum cathode," *Sol. Energy Mater. Sol. Cells*, vol. 95, no. 12, pp. 3303–3310, 2011.
- [35] J. Nishinaga, T. Aihara, H. Yamagata, and Y. Horikoshi, "Mechanical and optical characteristics of Al-doped C₆₀ films," *J. Cryst. Growth*, vol. 278, no. 1–4, pp. 633–637, 2005.

- [36] M. P. de Jong, L. J. van IJzendoorn, and M. J. a de Voigt, "Stability of the interface between indium-tin-oxide and poly(3,4-ethylenedioxythiophene)/poly(styrenesulfonate) in polymer light-emitting diodes," *Appl. Phys. Lett.*, vol. 77, no. 2000, pp. 2255–2257, 2000.
- [37] B. Ecker, J. C. Nolasco, J. Pallarés, L. F. Marsal, J. Posdorfer, J. Parisi, and E. Von Hauff, "Degradation effects related to the hole transport layer in organic solar cells," *Adv. Funct. Mater.*, vol. 21, no. 14, pp. 2705–2711, 2011.
- [38] H. Park, K. Y. Lee, W. Kim, H. W. Shin, D. H. Wang, T. K. Ahn, and J. H. Park, "Discrepancy of optimum ratio in bulk heterojunction photovoltaic devices: initial cell efficiency vs long-term stability," *ACS Appl. Mater. Interfaces*, vol. 5, no. 5, pp. 1612–1618, 2013.
- [39] S. Bertho, G. Janssen, T. Cleij, B. Conings, W. Moons, A. Gadisa, J. D'Haen, E. Goovaerts, L. Lutsen, J. Manca, and D. Vanderzande, "Effect of temperature on the morphological and photovoltaic stability of bulk heterojunction polymer:fullerene solar cells," *Sol. Energy Mater. Sol. Cells*, vol. 92, no. 7, pp. 753–760, 2008.
- [40] T. Wang, A. J. Pearson, A. D. F. Dunbar, P. A. Staniec, D. C. Watters, H. Yi, A. J. Ryan, R. A. L. Jones, A. Iraqi, and D. G. Lidzey, "Correlating structure with function in thermally annealed PCDTBT:PC₇₀BM photovoltaic blends," *Adv. Funct. Mater.*, vol. 22, no. 7, pp. 1399–1408, 2012.

- [41] J. Zhao, A. Swinnen, G. Van Assche, J. Manca, D. Vanderzande, and B. Van Mele, "Phase diagram of P3HT/PCBM blends and its implication for the stability of morphology," *J. Phys. Chem. B*, vol. 113, no. 6, pp. 1587–1591, 2009.
- [42] M. Koch, R. Nicolaescu, and P. V. Kamat, "Photodegradation of polythiophene-based polymers: excited state properties and radical intermediates," *J. Phys. Chem. C*, vol. 113, no. 27, pp. 11507–11513, 2009.
- [43] M. Manceau, J. Gaume, A. Rivaton, J.-L. Gardette, G. Monier, and L. Bideux, "Further insights into the photodegradation of poly(3-hexylthiophene) by means of X-ray photoelectron spectroscopy," *Thin Solid Films*, vol. 518, no. 23, pp. 7113–7118, 2010.

CHAPTER 4

EXPERIMENTAL TECHNIQUES

4.1 Introduction

This chapter describes the materials used in this thesis and the fabrication processes used in the manufacture of binary and ternary blend OPV devices. It also discusses the device structure and the measurement techniques used for lifetime tests. Finally, a description of the instrumentation used for characterization is provided.

4.2 Materials and device structure

The standard device used in this study was a binary blend bulk heterojunction of a donor and acceptor that was sandwiched between two electrodes, as illustrated in Figure 4.1 (a). As stated previously, one significant disadvantage of OPV devices is their short lifetime. In this study, a ternary bulk heterojunction active layer was proposed as a route to improve the lifetime. This was formed by introducing an insulating polymer into the active layer. The structure of this device is shown in Figure 4.1 (b).

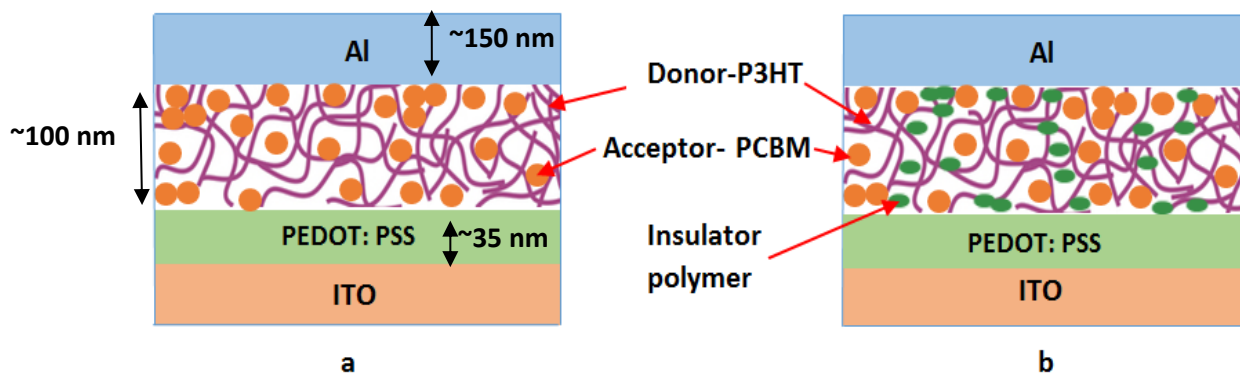


Figure 4.1. Schematic structure of devices based on (a) a binary blend film, (b) a ternary blend film.

4.2.1 Active layer

The bulk heterojunction active layer represents the heart of the OPV. The electron donor used in the active layer was regioregular poly (3-hexylthiophene-2, 5-diyl) (P3HT) (Rieke Metals, $M_w=50-70 \text{ kg mol}^{-1}$) which is the most studied polymer used for OPV devices to date [1]. The chemical structure of P3HT is shown in Figure 4.2.

P3HT can crystallize and create thin fibrils which form a percolating network for carrier transport. The polymer possesses a high hole mobility [2], which ranges from $10^{-4} \text{ cm}^2 \text{ V}^{-1} \text{ s}^{-1}$ up to $10^{-1} \text{ cm}^2 \text{ V}^{-1} \text{ s}^{-1}$ [3]. The polymers have good solubility in common organic solvents [4]. The band gap of P3HT is around 1.9 eV, which limits the absorption onset to approximately 650 nm [5].

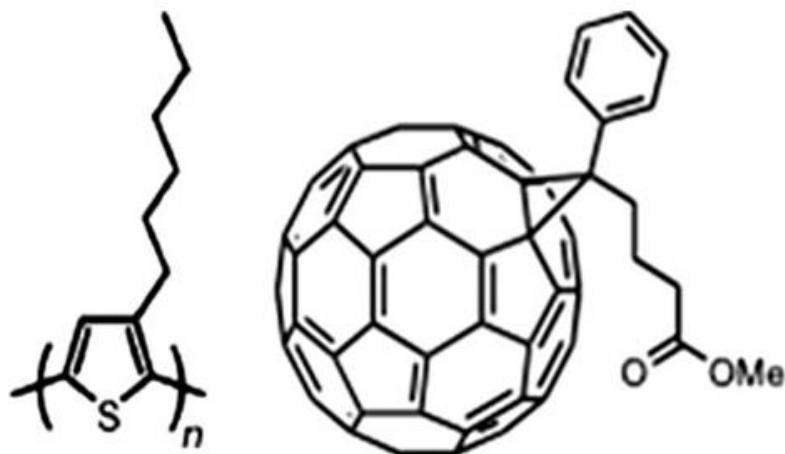


Figure 4.2. Chemical structures of P3HT (left) and PCBM (right).

The electron acceptor used here was [6, 6]-phenyl C₆₁ butyric acid methyl ester (PCBM) (Luminescence Technology Corp., $M_w=0.91 \text{ kg mol}^{-1}$), which has a high electron affinity. This makes it a popular acceptor used for OPV devices [6]. Its chemical structure is illustrated in Figure 4.2.

PCBM shows high solubility in common organic solvents [2]. It has excellent charge transport properties, so that electrons can move from one molecule to another [6]. The energy level diagram of the device structure ITO/PEDOT: PSS/P3HT: PCBM/Al is shown in Figure 4.3.

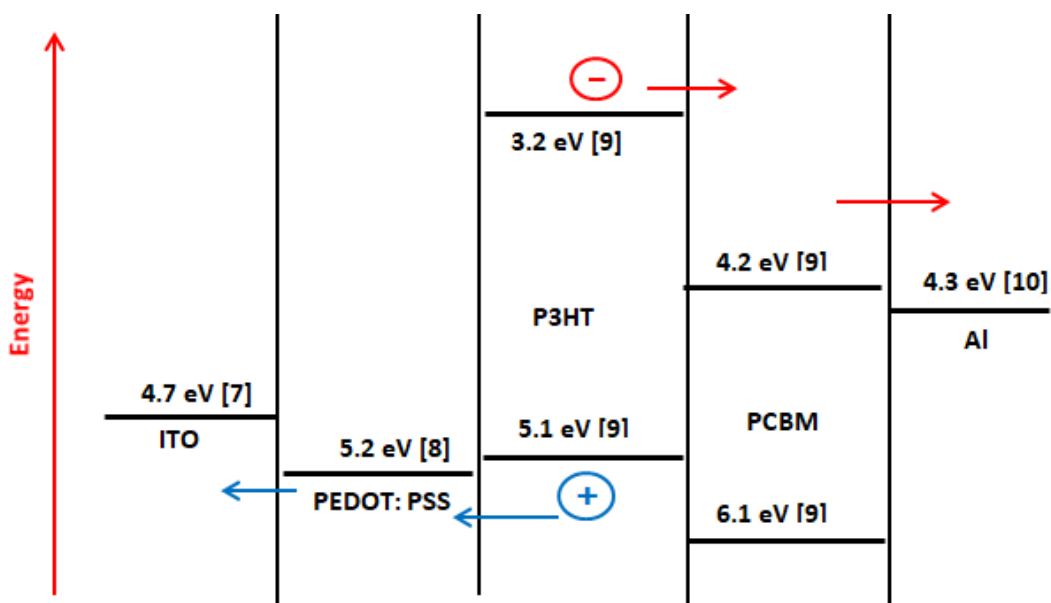


Figure 4.3. Energy level diagram showing the component in a standard device. Ref [7][8][9][10].

4.2.2 Insulating polymers

The insulating polymers used for ternary blend films were polystyrene (PS) (Sigma-Aldrich, $M_w=400\text{kg mol}^{-1}$), poly(methyl methacrylate) (PMMA) (Sigma-Aldrich, $M_w=97\text{ kg mol}^{-1}$) and poly(ethylene glycol) (PEG) (Sigma-Aldrich, $M_w=108\text{ kg mol}^{-1}$). These polymers were chosen due to their "hygroscopicity," which is the ability of a material to absorb humidity from the air [11]. The most hygroscopic polymer is PEG, while PMMA has an intermediate hygroscopicity, and PS is the least hygroscopic [12]. The chemical structures of these polymers are shown in Figure 4.4, and detailed properties of each polymer are provided in the following sections.

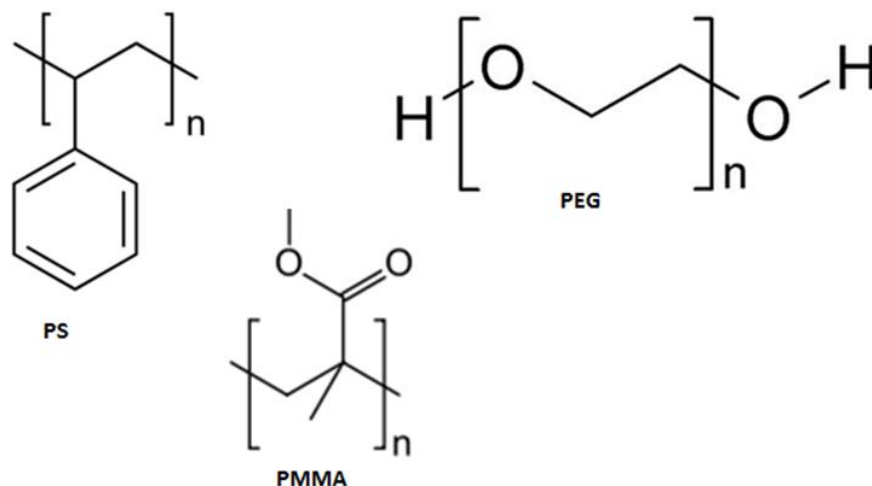


Figure 4.4. Chemical structures of the different insulating polymers used in this study.

(a) Poly(methyl methacrylate)

Poly(methyl methacrylate) (PMMA) is the polymer of methyl methacrylate, with the chemical formula $(C_5H_8O_2)_n$ [13]. It is commonly called acrylic [13]. It is readily available and dissolves easily in dichlorobenzene (DCB) which was used as the solvent for the P3HT:PCBM OPVs in this work. It also offers a light transmittance of 92% [14]. Physically, PMMA is a soft polymer that can be easily deformed [14].

PMMA is hygroscopic and absorbs water, with an absorption capacity ranging from 0.1-0.4% [15]. The absorption capacity is the maximum amount of water by weight that polymers can absorb when they are exposed to a humid environment [11], generally at 50% relative humidity (RH) and a temperature of 23°C, for 24 hours [15].

(b) Polystyrene

Polystyrene (PS) is a long chain hydrocarbon with alternating carbon atoms connected to phenyl groups [16]. The chemical formula of PS is $[\text{CH}_2\text{-CH}(\text{C}_6\text{H}_5)]_n$ [17]. It is an amorphous, nonpolar, glassy polymer which is also an excellent electrical insulator and inexpensive [18]. The phenyl (benzene) groups can arrange in three ways: all on one side of the polymer chain, so called 'isotactic polystyrene'; if they arranged on alternative sides of the backbone, the polymer called "syndiotactic polystyrene" and if they are randomly distributed on both sides of the chain, the polymer is called 'atactic polystyrene' [16]. This random positioning of phenyl (benzene) groups prevents the chains from achieving any crystallinity and the polymer can be easily dissolved in a chlorinated solvent [16]. In this study, atactic polystyrene (a-PS) was used due to it being readily soluble in the DCB solvent, which was used for P3HT: PCBM OPVs. The light transmission of PS is 80-90% [16]. The water absorption capacity of PS is 0.01-0.07% [15], which is lower than that of PMMA.

(c) Polyethylene glycol

Polyethylene glycol (PEG) is a hydrophilic polymer synthesized from ethylene oxide [19]. The molecular formula structure for PEG is $\text{H}(\text{OCH}_2\text{CH}_2)_n\text{OH}$, where n represents the number of ethylene glycol units contained in the polymer chain [20]. PEG is considered to be a super absorbent polymer [11]. Superabsorbent materials are hydrophilic networks that can absorb and retain huge amounts of water or aqueous

solution [11]. The capacity of PEG for absorbing water depends on its molecular weight, and ranges from 50%-100% [11], [21]. The absorption capacity of the PEG used in this study reached around 50% [21].

4.2.3 Electrodes

The active layer is sandwiched between two electrodes with different work functions, chosen to match the donor HOMO and the acceptor LUMO. This leads electrons to transfer to the low work function electrode and holes to transfer to the high work function electrode [22]. Here, the low work function material is aluminium (Al) (4.3 eV) [10]. This metal is thermally evaporated on top of the active layer and forms the cathode. Indium tin oxide (ITO) (VisionTek Systems Ltd., sheet resistance 7 Ω /sq) forms the high work function (4.7 eV) anode [7]. This electrode is a transparent thin film material coated onto a glass substrate. It possesses high optical transparency up to 90.2% [23], and electrical conductivity ($\sigma = 7.2 \times 10^{-4} \Omega \cdot \text{cm}$) [23].

4.2.4 The interfacial layer

Poly (3, 4-ethylene dioxythiophene): poly (4-styrene sulfonate) (PEDOT: PSS) (CLEVIOS P VP AI 4083 purchased from Heraeus) was used to coat the ITO. It forms a transparent film with high conductivity and has high visible light transmission [24]. The chemical structure of PEDOT: PSS is shown in Figure 4.5.

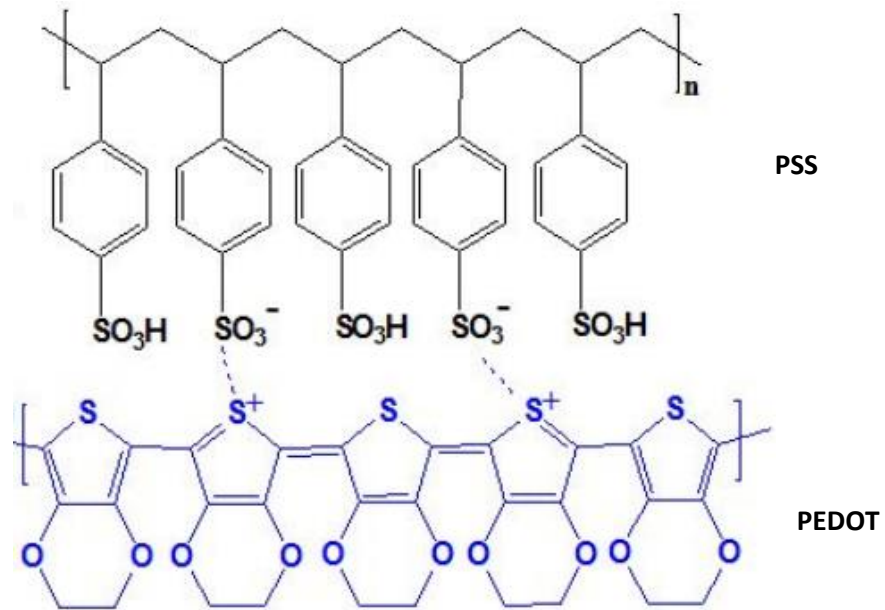


Figure 4.5. The chemical structure of PEDOT: PSS. The dots linking the SO_3^- and thiophene rings represent ionic bonds resulting in a complex structure of PEDOT with PSS.

PEDOT: PSS is used to smooth the surface of the ITO, reduce the diffusion of indium into the active layer, and has a work function matching that of the donor HOMO [25]. The high work function of this material allows it to improve hole injection from the active layer. This is because of the work function of PEDOT: PSS is around 5.2 eV [8], which provides a better match to the HOMO orbital of P3HT than ITO, as shown in Figure 4.3.

4.3 Deposition techniques

Two deposition techniques were used: thermal evaporation for the cathode, and spin coating for the PEDOT: PSS and active layers.

4.3.1 Thermal evaporation

Thermal evaporation works by heating the source material to a high temperature in a vacuum chamber until it reaches the point of evaporation. The evaporation source used here was a tungsten filament. The source material, in the form of aluminium wire, was hung over the filament. The electrical power to the filament was increased until the metal melted and started to evaporate. The metallic vapor travels in the chamber until it reaches and condenses onto the substrate surface, as shown in Figure 4.6.

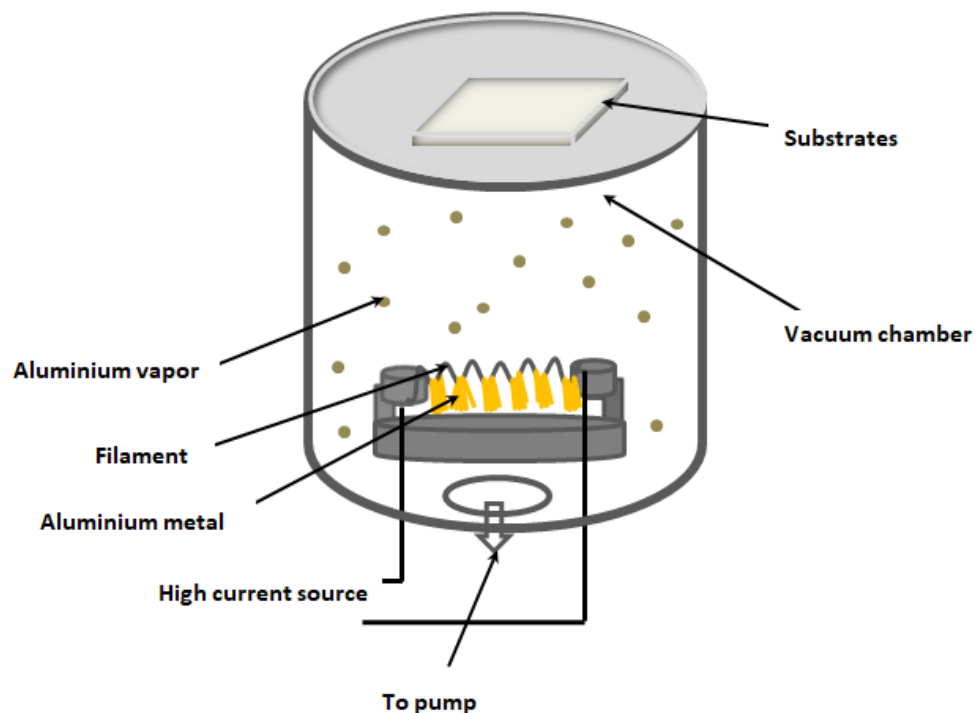


Figure 4.6. Schematic diagram of a thermal evaporation system.

Evaporation was carried out under a high vacuum ($<3 \times 10^{-6}$ mbar), so that the vapor reached the substrate without collision or reaction with gas molecules in the chamber. Two Edwards 306 thermal evaporators

were used in this study: one inside a glovebox that was used to deposit metal cathodes on the top of the active layers and one outside the glovebox that was used to deposit Al layers on glass slides to enable FTIR measurements.

4.3.2 Spin coating

Spin coating is a common technique used for the deposition of uniform thin films on substrates. The steps involved in this technique are depicted schematically in Figure 4.7. First, an excess amount of solution is applied on top of the substrate which is placed on the chuck of the spinner and held in place using vacuum (Figure 4.7 (a & b)). As the chuck accelerates (Figure 4.7 (c)), the solution is spread, by centrifugal force, over the entire surface of the substrate. During spinning (Figure 4.7 (d)), the excess amount of solution flows outward across the substrate and a uniform thin film is formed.

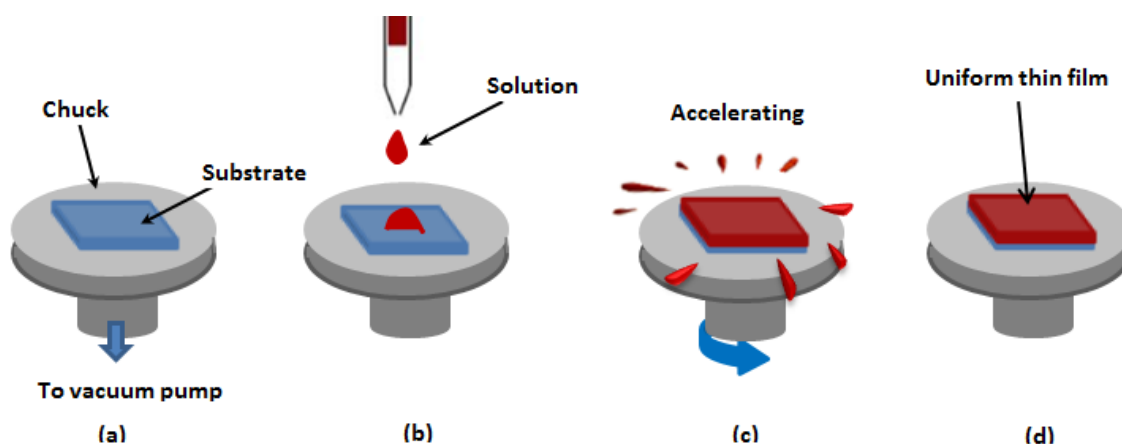


Figure 4.7. Schematic diagram showing the spin coating process.

The solvent evaporates during spinning. This is an important parameter in OPV devices because the rate of solvent evaporation from a thin film has a strong influence on the film morphology, which in turn affects the efficiency of the device [26], [27]. A uniform film thickness is another important factor. This can be obtained by controlling different parameters in the spin process such as spin speed, duration of spin and viscosity of the solution [28]. The general formula that shows the relationship between the quantities can be expressed in equation 4.1 [28]

$$d = \left(\frac{\eta}{4\pi\rho\omega^2} \right)^{\frac{1}{2}} t^{-\frac{1}{2}} \quad (4.1)$$

where d is the thickness of the spun film, η is the viscosity coefficient of the solution, ρ is the density of the solution, ω is the angular velocity of spinning, and t is the spinning time.

In this study two spin coaters were used: a WS-650 B (Laurell Technologies Corporation) used to spin-coat the PEDOT: PSS layers and a home made system located inside a glovebox to spin-coat the active layers and insulating polymers.

4.4 Fabrication process

Several steps were involved in the fabrication of ITO/PEDOT: PSS/P3HT: PCBM/Al devices. The processes are illustrated schematically in Figure 4.8 and described in detail in the following sections.

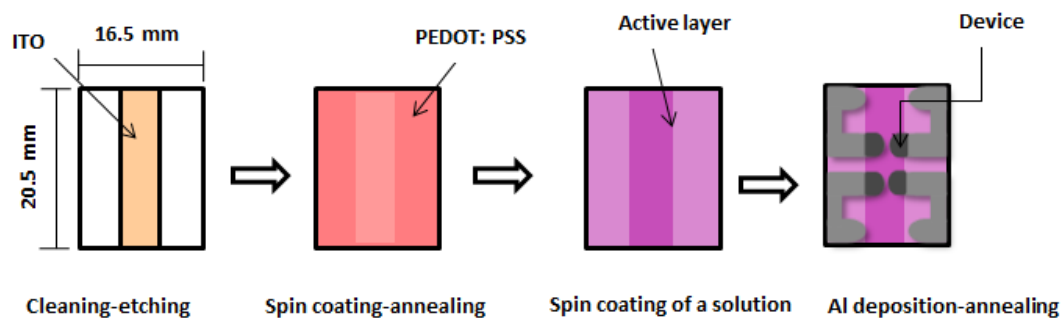


Figure 4.8. Fabrication of an OPV device.

4.4.1 Substrate preparation

Substrates (dimensions 20.5 mm x 16.5 mm) were cut from sheets of ITO-coated glass. The ITO layer was patterned by masking a 6 mm strip down the centre of each substrate with Lacomit Varnish (G371, Agar Scientific Ltd). After allowing 15 minutes for the varnish to dry, the remaining areas were painted with an aqueous paste of zinc powder, and then etched by immersing them in hydrochloric acid. The patterned substrates were sonicated in Decon 90 solution (2% aqueous), deionized water, acetone, and then propanol-2-ol for 15 minutes each, and followed by drying with N₂ gas. The cleaned substrates were exposed to oxygen plasma (Yield Engineering Systems Inc., YESR3) for 5 minutes with a radio frequency (RF) power of 100 W.

4.4.2 PEDOT: PSS layer

The conductive polymer PEDOT: PSS was filtered using a 0.2 μm poly(tetrafluoroethylene) (PTFE) syringe filter. A micropipette was used to drop 200 μl of the filtered material onto the clean substrate surface before spinning at 2500 rpm for 45 seconds and annealing at 140 °C for

10 minutes in ambient air, to give a layer thickness of 30-35 nm, as measured by atomic force microscopy (AFM).

4.4.3 Blend solution

(a) Preparation of binary solution

Working in a glovebox, separate 30 mg/ml solutions of P3HT and PCBM were prepared by dissolving 30 mg of each in 1ml of anhydrous 1,2-dichlorobenzene (DCB, Sigma-Aldrich) and stirring for 30 minutes. These solutions were mixed in a ratio of 1:1 by volume and stirred overnight. A micropipette was used to drop 150 μ l of this mixture onto the PEDOT: PSS coated substrates before spinning at 1000 rpm for one minute.

(b) Preparation of ternary solution

In order to make a ternary blend solution, 10 mg/ml solutions of insulating polymer (PS, PMMA or PEG) was prepared by dissolving the solid material in DCB and stirring for two days (PMMA) or 4-5 hours (PEG and PS) in a glovebox, to achieve a clear solution. Binary P3HT: PCBM solution with a concentration of 30 mg/ml was prepared and stirred for 3 hours before the insulating polymer solution was added. This ternary solution was then stirred overnight before spin coating.

4.4.4 Active layer

A uniform film of the active layer was achieved by dropping 150 μ l of the binary or ternary solution onto the PEDOT: PSS film and then

spinning at 1000 rpm for 60 seconds. The thickness of the film varied from 95-130 nm depending on the type of solution used in the experiment.

4.4.5 Al evaporation

Al cathodes, 150 nm thick, were thermally evaporated through a shadow mask. The base pressure in the vacuum chamber of the evaporator was $<3 \times 10^{-6}$ mbar. A deposition rate of 1 nm/s was maintained by carefully observing a quartz crystal film thickness monitor and adjusting the power supplied to the filament during the deposition. Finally, the devices were annealed at 120 °C for 10 min in the glovebox prior to lifetime tests. There were four devices on each substrate, defined by the overlap of the patterned ITO and Al electrodes.

4.4.6 Lamination process

To laminate the device, a solution of insulating polymer was prepared by dissolving 10 mg of insulating polymer (PMMA or PEG) in 1 ml of nitrobenzene (NB) solvent. After the OPV devices were fabricated and post annealed, the solution of insulating polymer was spun cast at 1300 rpm for 60 seconds onto the surface of the substrate, so that all of the devices were covered with the solution. Then, the insulating material was removed from the electrode contact pads by wiping with a cotton bud soaked in NB solvent.

4.5 Device Characterization

4.5.1 Current-voltage characteristics

The performance of OPV devices is established from the electrical characteristics by measuring the current density through the device as a function of applied bias (J-V characteristics).

(a) J-V curve under illumination

For the measurement of J-V under illumination, a solar simulator (Oriel Sol1A 94021 A) was used, which provided an illumination close to the Air Mass (AM 1.5) solar spectrum. Air mass is a standard terrestrial spectrum of sunlight after passing through the atmosphere at an angle of 48° [22]. This corresponds to an irradiance of 1000 W/m^2 .

A test chamber (Figure 4.9) was used to make reliable electrical contacts to the devices and enable repeatable measurements. A 1 mm diameter pinhole defined the illumination area of each device to 0.79 mm^2 . Spring pins were used to make contact to all four aluminium cathodes and the common ITO anode on each substrate. Outside the chamber, the connections between the device and the test instruments were made by two wires, one to the Al metal and the other to the ITO. A DC voltage sweep was applied to each device, from -1.0 V to 1.0 V with a step size of 200 mV , and the photo-generated current was measured, using a Keithley 2400 Source Meter controlled by a LabView PC program. This procedure was used to generate J-V curves, which are discussed in section 2.8.

(b) J-V curve in the dark

For the measurement of J-V in the dark, a Keithley 2400 source meter was used to create a J-V curve similar to a diode characteristic. Dark J-V curves were plotted on semi-logarithmic axes and without illumination. The shunt resistance (R_{sh}) is assumed to be much greater than the series resistance (R_s) [29]. R_{sh} in an OPV may originate from current leakage in the cell, while series resistance may arise from the bulk resistance of the active layer or contact resistance at the electrodes [30].

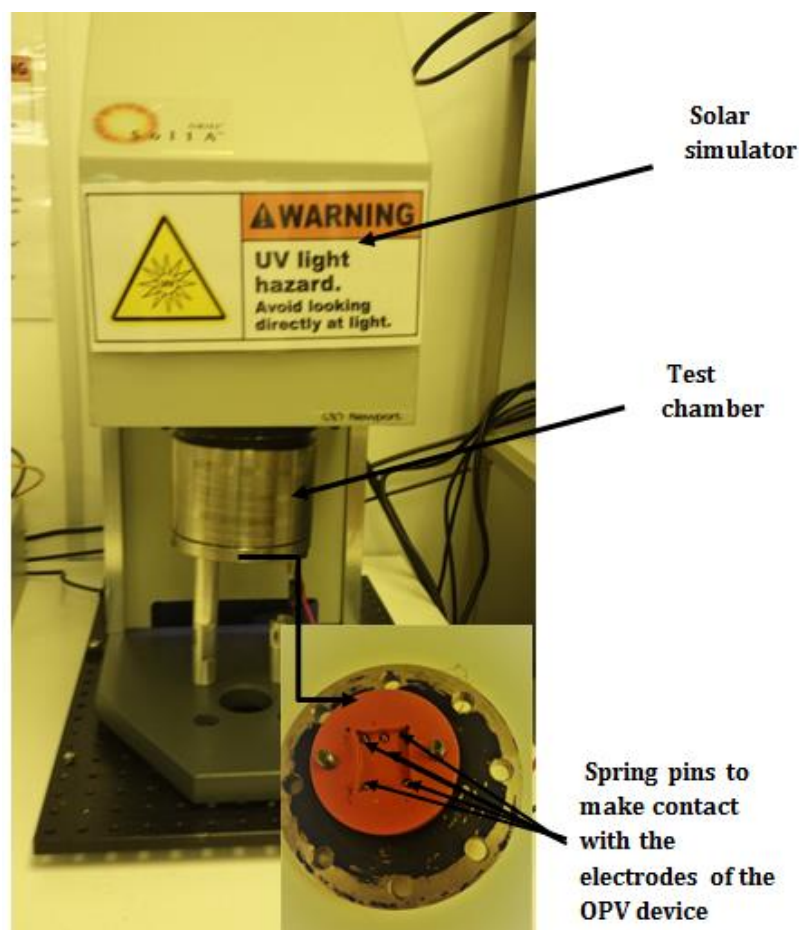


Figure 4.9. The test chamber.

Typically, the J-V curve is composed of three distinct regions [29]. From Figure 4.10, it can be seen that region I, called the shunt region, which is linear in the low voltage regime [31], where R_{sh} limits the current. This is followed by exponential behavior at intermediate positive voltages (region II), where the current increases exponentially, and is controlled by the diode. Region III is the high voltage regime where the current is limited by the series resistance, and the curve is mostly linear [29].

The reverse current in the dark J-V curve indicates the amount of leakage current that may occur at the electrode-active layer interface, which can affect the open circuit voltage [32].

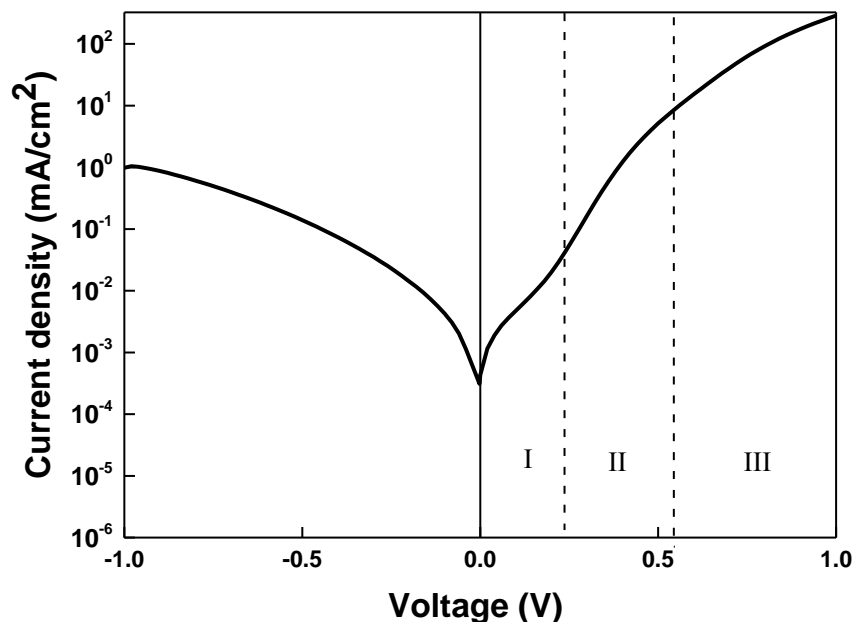


Figure 4.10. J-V curve in the dark for a standard device (P3HT: PCBM).

4.5.2 Space charge limited current for hole mobility measurements

Space charge limited current (SCLC) is a simple method that may be used to measure charge carrier mobility in organic semiconductors. In order to be valid, only one type of charge carrier in a blend film can be present, meaning injection of the other carrier must be suppressed via large injection barrier [33]. In this study, the hole mobility was measured by fabricating hole-only devices. This was achieved by replacing the low work function aluminium cathode with the high work function metal Au [34]. In this type of device, electron injection into the LUMO of PCBM is suppressed. The work functions of both electrodes: Au (-5.1 eV) [33], and PEDOT: PSS (-5.2 eV) [8] are close to the HOMO level of P3HT (-5.1 eV) [35]. Therefore, the current in the device is hole-dominated. Figure 4.11 shows a band diagram of such a hole-only device.

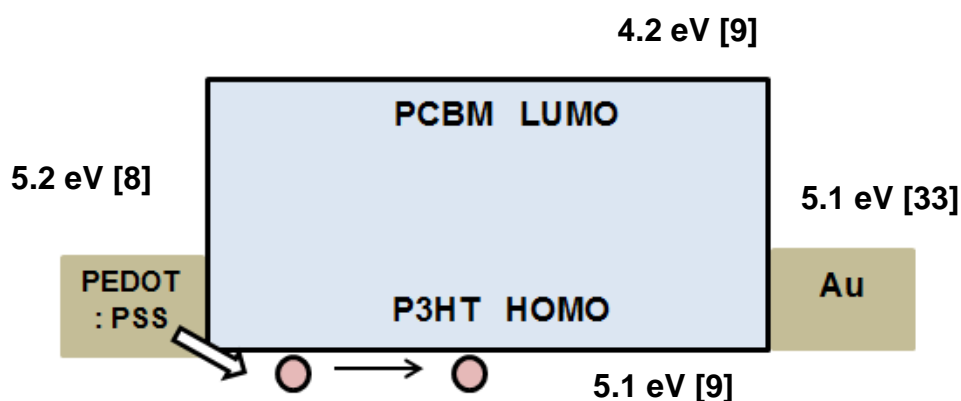


Figure 4.11. Schematic diagram of a hole-only device based on P3HT: PCBM. Ref [8][9][33].

The PEDOT: PSS forms an ohmic contact for hole injection, whereas the mismatch between the work function of Au and the LUMO of PCBM (-4.2 eV) [9], strongly suppresses the injection of electrons into the PCBM. The hole mobility can be measured by fitting the Mott-Gurney equation, which will be discussed in Chapter 8, to the experimental data of the dark J-V curve.

4.5.3 Ultraviolet-visible spectroscopy

Ultraviolet-visible (UV-vis) spectroscopy is an optical technique used to obtain information about the absorption of organic polymers. It can also provide information on crystalline vibrations and molecular interactions. P3HT and PCBM absorb light in the UV-Vis spectral region. A typical absorption spectra for a P3HT: PCBM film is shown in Figure 4.12.

Three absorption peaks are observed in P3HT: the absorption peak of the P3HT main chain and two absorption shoulders. These two absorption shoulders indicate the level of crystalline order and the inter-chain interaction in the conjugated polymer [36]. The higher the crystallinity and P3HT order, the more pronounced are the shoulders. In this study, the absorption peak is at approximately ~ 512 nm, while the absorption shoulders are at ~ 558 nm and 600 nm, as shown in Figure 4.12.

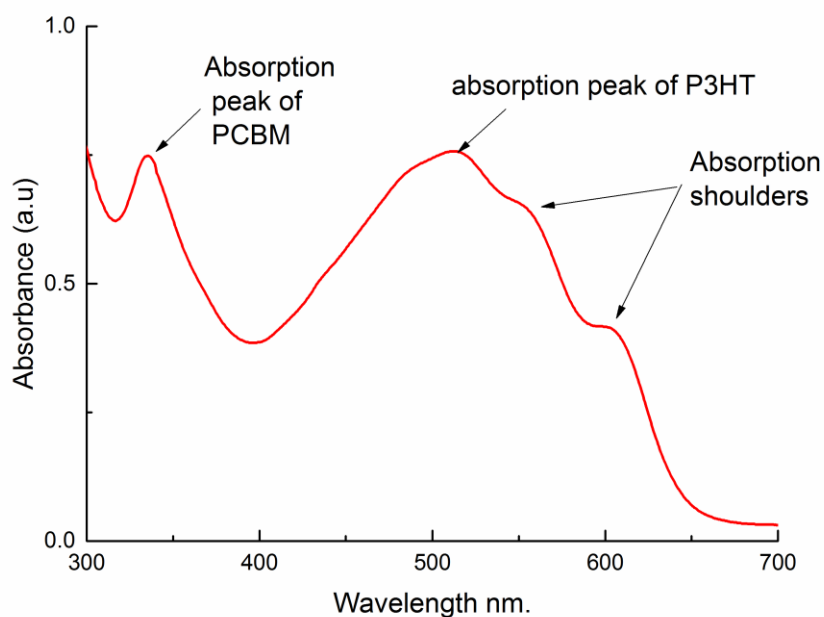


Figure 4.12. Typical absorption spectrum of a P3HT: PCBM blend film.

Light absorption occurs when sufficient light energy is incident in the region of electronic transitions (HOMO-LUMO transitions), causing an electron to move from the ground state to an excited state [37]. Spectroscopy records the wavelength at which the absorption occurs[37]. The spectrum is measured by absorbance (A) which can be defined by the logarithmic ratio between the incident light intensity (I_0) and the transmitted light intensity (I). This is expressed by Beer's Law [37]:

$$A = \log (I_0/I) \quad (4.2)$$

The absorption spectra of blend films were measured using a Shimadzu UV-1800 spectrophotometer over the range 190 to 1100 nm. The instrument uses two light sources: a deuterium lamp for UV light and a tungsten iodine/halogen lamp for visible light. A diffraction grating is

used to split the light into different wavelengths. The detector measures the photons that are transmitted through the film. A schematic diagram of the spectrometer is shown in Figure 4.13.

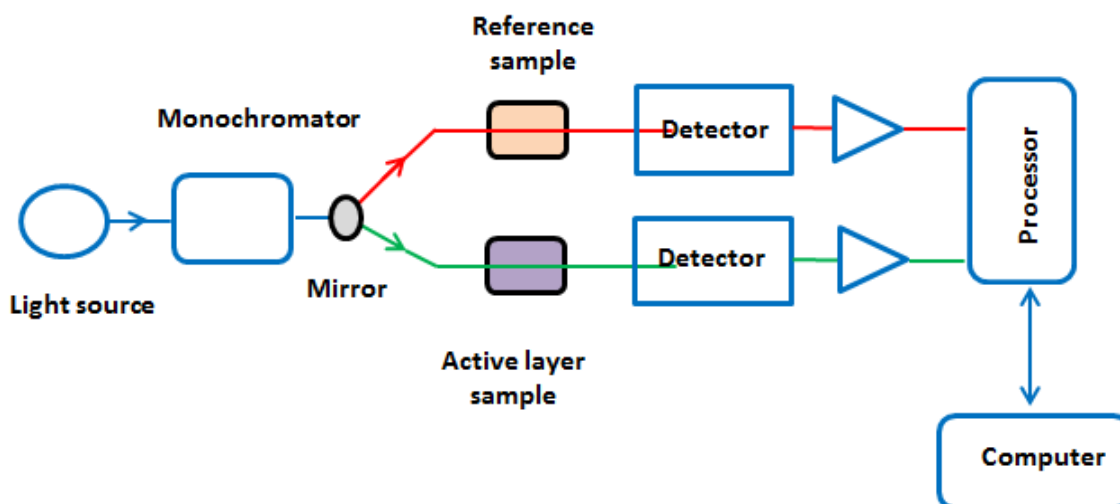


Figure 4.13. Schematic diagram of a spectrophotometer.

A clean ITO glass substrate coated with a PEDOT: PSS layer was used as the reference sample. This was inserted into the first holder, and the baseline was corrected to measure I_0 , while in the second holder, an active layer sample, was inserted.

4.5.4 Atomic force microscopy

Atomic force microscopy (AFM) is a scanning probe technique that can be used to image the topography of a surface at high resolution. Figure 4.14 shows the basic components of a typical AFM.

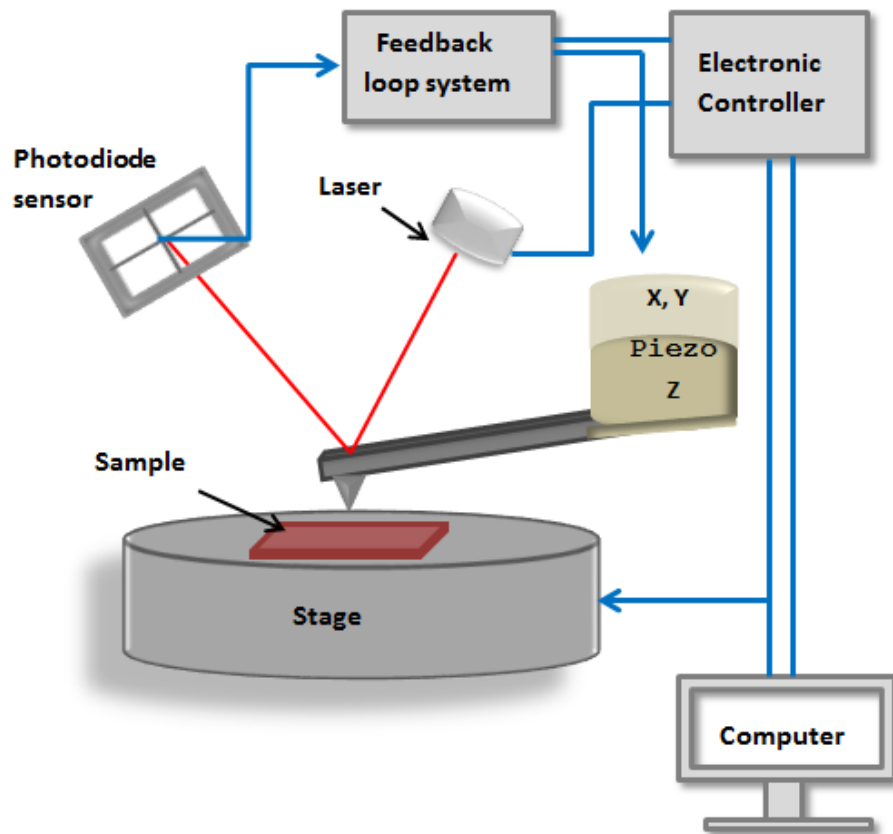


Figure 4.14. Schematic diagram showing the basic components of an AFM system.

The AFM has a sharp tip (radius typically <10 nm) that is attached to the end of a cantilever spring. As the tip is scanned across the surface of the sample, the force between the tip and the surface causes the cantilever to deflect. This deflection is detected by the movement of a laser beam reflected from the back of the cantilever onto a quadrant photodetector [38]. There are three main imaging modes in an AFM: contact, non-contact and tapping mode [39]. In contact mode, the tip is in continuous contact with the surface of the sample. In non-contact mode, the tip does not contact the surface, but oscillates during scanning, with an amplitude typically from a few nm (<10) down to a few pm. In tapping mode, the cantilever oscillates at its resonant frequency,

with an amplitude ranging from a few nm up to 200 nm, and the tip touches the surface gently [39]. This mode was used in this study for topography. The cantilever oscillation is achieved using a piezoelectric crystal in the tip holder. The oscillating tip is moved toward the surface until it engages and starts to scan. Interactions between the tip and the sample cause the amplitude of the cantilever oscillations to change (usually decrease). The oscillation amplitude of the tip is measured by the detector. A feedback loop system maintains constant oscillation amplitude by controlling the height of the tip above the sample. The z-movement required to maintain this constant amplitude is used to generate a topographic image [39].

Two images are produced simultaneously: topography and phase images. A phase image occurs when the tip moves across regions of different composition on the surface. The phase image is used to map the variation in surface properties such as adhesion, elasticity, and friction. It can also detect contamination, and the different components in composite materials to some extent [40].

Typically, the scan size was adjusted to 10 μm \times 10 μm . By carefully adjusting the set point, the force on the sample was minimized during scanning of the surface to prevent damage to the tip and the sample. To ensure a clear image, a slow scan rate was employed. A Dimension 3100 microscope and Nanoscope IVa controller were used to image the surface of OPV devices and determine the root mean square (rms) roughness (R_q). It was also used to measure the thickness of the active layer. The AFM probe was from Budget Sensors, model Tap300Al-

G with a spring constant of 0.2 Nm^{-1} . The captured AFM data were analyzed using Gwyddion 2.42 software.

a) Measuring the active layer thickness

The thickness was measured by imaging the edge of a scratch, created by abrasion using a sharp metal point. The sample was placed on the stage surface, and the scratched area was scanned at a location where all of the device layers could be clearly observed. After the topography data had been collected, the image was flattened using the AFM software. Finally, both the total thickness of the device layers (active layer + PEDOT: PSS layer) and the PEDOT: PSS thickness were determined, separately, from a line profile. The active layer thickness was calculated by subtracting the thickness of the PEDOT: PSS from the total thickness.

b) Conductive atomic force microscopy

Conductive atomic force microscopy (C-AFM) is an electrical mode that can provide information about the electrical properties of organic thin films. In this study, a C-AFM was used to measure the distribution of conductivity over the surface of the active layer using a gold-coated tip as an electrical probe (Budget Sensors, model ContGB-G). A wire was attached to the ITO using a small amount of Electrodag 1415 M conductive silver paint, so that an appropriate potential difference could be applied between the gold-coated tip and the ITO. As the tip scanned the surface (in contact mode) the current flowing between the sample

and the tip was measured, and a current map generated, simultaneously with the topography image.

It was found from C-AFM experiments that the quality of the current image depended on the scan history of the region under investigation. The surface was damaged by the tip (AFM-tip ploughing) so that more than one scan in the same area could change the value of the current and affect the results. This is demonstrated in Figure 4.15.

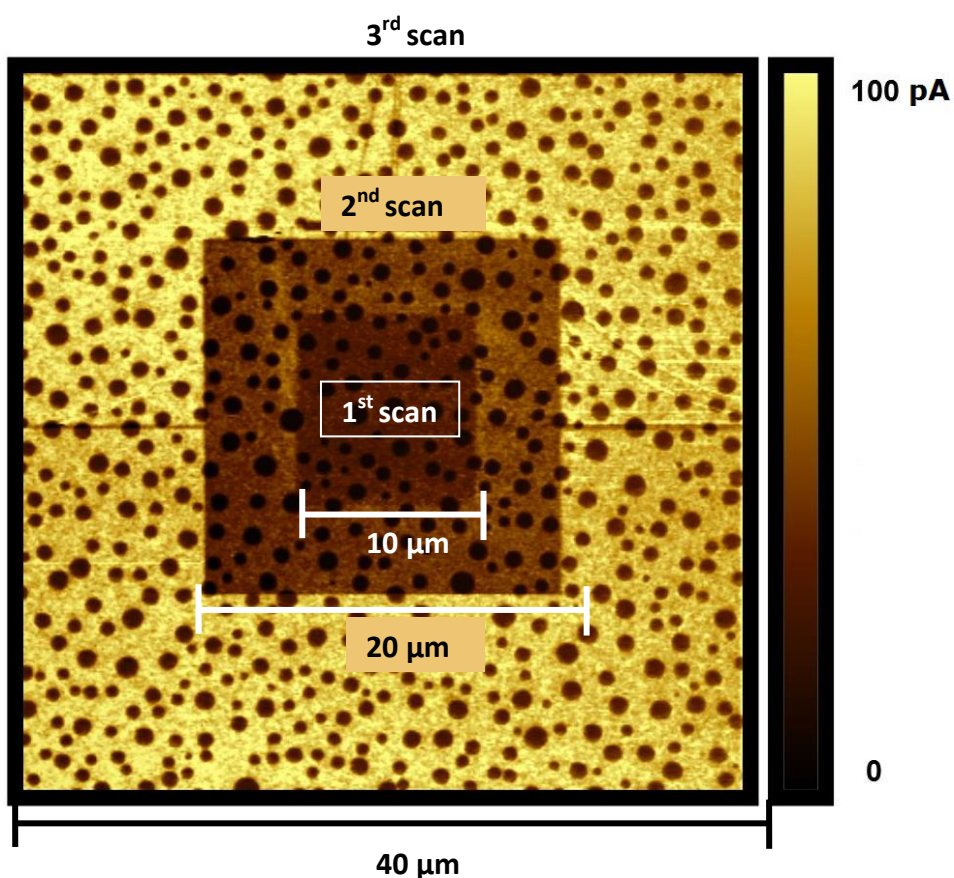


Figure 4.15. C-AFM image of a ternary blend film showing the effect of repeated rescanning on the image quality.

Three scans, with increasing size, were performed on a ternary blend film of P3HT: PCBM: PMMA, allowing the effect of rescanning the same area to be clearly seen. Figure 4.15 shows the current map obtained from the third scan. Different current values were observed in

each of the three areas (10 μm , scanned three times; 20 μm , scanned twice; 40 μm , scanned once), the current was reduced by repeatedly scanning an area. Therefore, to get a high quality image with the correct current, images were taken from the first scan of an area only.

4.5.5 Fourier transform infrared spectroscopy

Fourier transform infrared (FTIR) spectroscopy is a technique based on inducing vibrations, stretching or twisting in the chemical bonds of molecules by illumination with infrared radiation [41]. The changes in the chemical bonds can be detected and then translated into a spectrum. Figure 4.16 shows the basic components of an FTIR spectrometer.

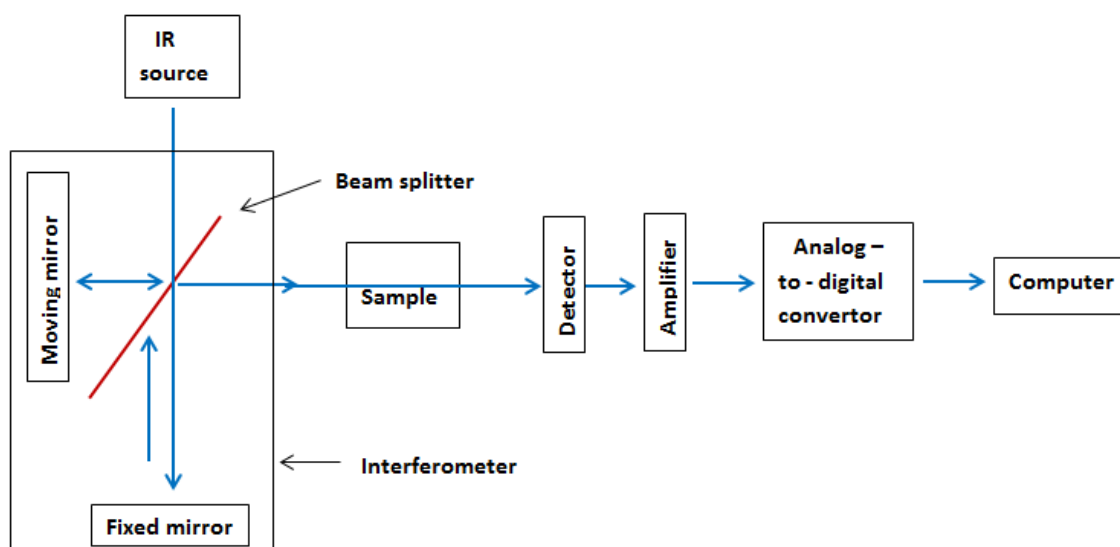


Figure 4.16. Schematic diagram showing the basic components of an FTIR instrument. Redrawn from [41].

Polychromatic infrared radiation passes through the interferometer, which splits the beam into two, and then recombines with the difference in path lengths leading to destructive and constructive

interference [41]. The recombined beam passes through the sample which absorbs energy, causing the chemical bonds to vibrate. The detector measures the variation in vibration energy versus time for all absorbed wavelengths in the sample. This signal is converted to digital form by an analog-to-digital converter and transferred to the computer for Fourier-transformation. The Fourier transform converts an intensity-vs-time spectrum into an intensity-vs-frequency spectrum in units of inverse centimeters (wavenumbers).

A Nicolet NEXUS FTIR spectrometer working with OMNIC software in the Chemistry Department at Durham University was used to observe any chemical changes that may occur in the active layer during the degradation process. Spectra were recorded by collecting 128 scans with 4 cm^{-1} resolution over the range 600 cm^{-1} to 4000 cm^{-1} . A background spectrum, measured using an Al-coated glass slide was collected first. After this step, the active layer sample was run. The active layer was prepared by drop casting $400\text{ }\mu\text{l}$ of P3HT:PCBM solution onto a glass substrate coated with Al of 100 nm thickness. The wet film was left in the glovebox for 24 h to dry.

4.5.6 Scanning electron microscopy

Scanning electron microscopy (SEM) uses an electron beam to image the layers of OPVs. Typically, the energy of the electron beam ranges from 0.5 keV to 30 keV . Images in this study were captured at a beam energy of 5 keV . Cross-sectional SEM images were obtained by coating the device with carbon followed by a protective platinum layer. A

cross section of the OPV device was cut using a focused ion beam (FIB) system.

SEM images were collected with a Hitachi SU-70 scanning electron microscope and FEI Helios Nanolab 600 microscope in the Physics Department at Durham University.

4.6 Lifetime measurements

The device lifetime can be determined by measuring the J-V characteristics at different times after fabrication. From the J-V curves, various electrical parameters can be obtained, such as J_{sc} , V_{oc} , FF, and PCE. The most useful parameter for monitoring the device lifetime is the PCE because it provides a direct measure of how efficiently the device can convert light into electrical energy.

The device lifetime was quantified using three parameters: T_0 , represents the initial time of OPV device when is tested immediately after fabrication, T_{80} and T_{20} , the time taken for the device efficiency to decay to 20% and 80% of its initial value, respectively [42].

4.7 Aging test environment

In order to understand how OPVs degrade over time, devices were stored in different environments at room temperature, 21°C. All devices were stored in the dark to exclude the effect of light. This was achieved by wrapping the devices in aluminium foil and then keeping them in the

appropriate environment for lifetime measurement. Different environments used in this study are listed as follows:

(a) Inert environment

A degradation test under an inert environment was made by storing the devices in a nitrogen filled glove box. The dew point inside the glovebox was -48°C , corresponding to a relative humidity of $<1\%$.

(b) Ambient environment

To test the degradation in an ambient environment, devices were stored in a cleanroom which had controlled atmospheric conditions. The temperature was 21°C while the humidity was controlled to be around 50% RH. The air in the cleanroom also contained less contamination, such as dust.

(c) High humidity environment

Devices were tested under high humidity conditions, reaching 85% RH, in an Espec SH-641 bench-top type temperature and humidity chamber (Figure 4.14). The temperature was fixed at 21°C . The control range of humidity at this temperature was from 50% to 95% RH. Devices were placed in the chamber after the humidity had stabilized at the desired value.

(d) Low humidity environment

A low humidity environment at 21°C was outside of the range achievable inside the temperature and humidity chamber. A desiccator containing silica gel was used to create a low relative humidity environment, as low as 1% RH, as shown in Figure 4.17.

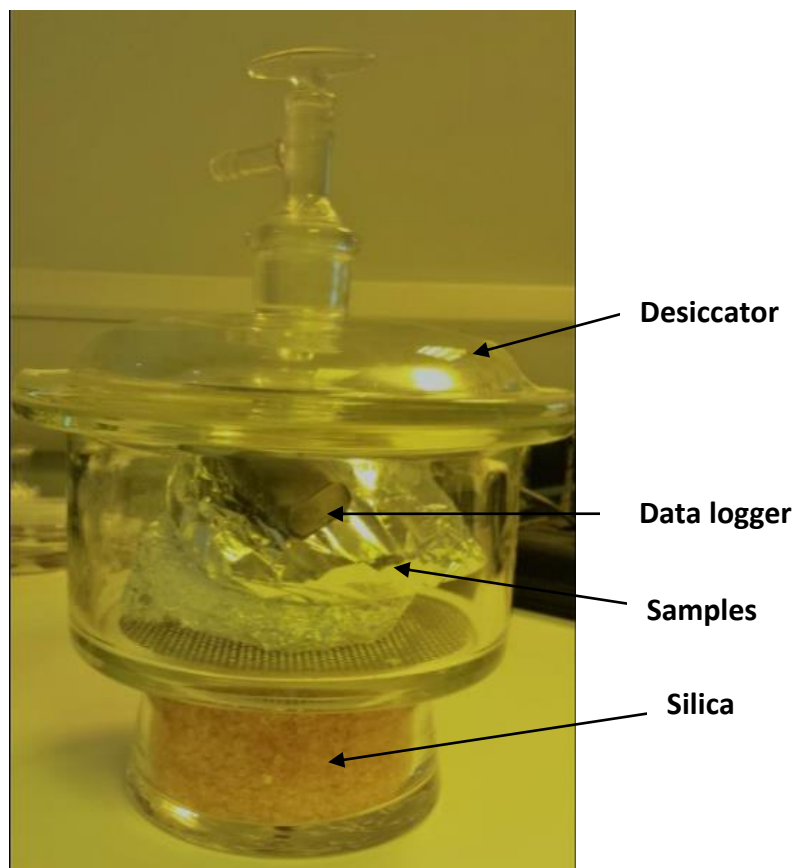


Figure 4.17. Low humidity environment in the desiccator.

To dry silica gel crystals, these were heated in an oven (Medline scientific-OV-II) at 150°C for 2 hours. This procedure was performed when the color of the self-indicating crystals changed, meaning that they were saturated with water. The desiccator was placed in a cleanroom. The conditions inside the desiccator were monitored during the aging test

using an EL-USB-2 temperature and humidity logger. The devices were placed in the desiccator, which was sealed, and only opened when measurements were to be performed.

Finally, it is important to note that all the four devices on each substrate in all the experiments in this study were measured and all the J-V curves illustrated in the thesis represent typical devices.

4.8 References

- [1] M. T. Dang, L. Hirsch, and G. Wantz, "P3HT: PCBM, best seller in polymer photovoltaic research," *Adv. Mater.*, vol. 23, no. 31, pp. 3597–3602, 2011.
- [2] P. Kumar and S. Chand, "Recent progress and future aspects of organic solar cells," *Prog. Photovoltaics : Res. Appl.*, vol. 20, pp. 377–415, 2012.
- [3] F. Laquai, D. Andrienko, R. Mauer, and P. Blom, "Charge carrier transport and photogeneration in P3HT: PCBM photovoltaic blends," *Macromol. Rapid Commun*, vol. 36, pp. 1001–1025, 2015.
- [4] R. Hu, W. Zhang, P. Wang, Y. Qin, R. Liang, L. M. Fu, J. P. Zhang, and X. C. Ai, "Characterization and distribution of poly(3-hexylthiophene) phases in an annealed blend film," *ChemPhysChem*, vol. 15, pp. 935–941, 2014.
- [5] R. Kroon, M. Lenes, J. Hummelen, P. Blom, and B. de Boer, "Small bandgap polymers for organic solar cells (polymer material development in the last 5 years)," *Polym. Rev.*, vol. 48, no. 3, pp. 531–582, 2008.
- [6] G. Dennler, M. C. Scharber, and C. J. Brabec, "Polymer-fullerene bulk-heterojunction solar cells," *Adv. Mater.*, vol. 21, no. 13, pp. 1323–1338, 2009.

- [7] L.-M. Chen, Z. Hong, G. Li, and Y. Yang, "Recent progress in polymer solar cells: manipulation of polymer: fullerene morphology and the formation of efficient inverted polymer solar cells," *Adv. Mater.*, vol. 21, no. 14–15, pp. 1434–1449, 2009.
- [8] J. Jeong, S. Woo, S. Park, H. Kim, S. W. Lee, and Y. Kim, "Wide range thickness effect of hole-collecting buffer layers for polymer: fullerene solar cells," *Org. Electron.*, vol. 14, no. 11, pp. 2889–2895, 2013.
- [9] D. Veldman, S. Meskers, and R. Janssen, "The energy of charge-transfer states in electron donor-acceptor blends: insight into the energy losses in organic solar cells," *Adv. Funct. Mater.*, vol. 19, no. 12, pp. 1939–1948, 2009.
- [10] C. Deibel, A. Wagenpfahl, and V. Dyakonov, "Influence of charge carrier mobility on the performance of organic solar cells," *Phys. Status Solidi -Rapid Res. Lett.*, vol. 2, no. 4, pp. 175–177, 2008.
- [11] M. J. Zohuriaan-Mehr and K. Kabiri, "Superabsorbent polymer materials: a Review," *Iran. Polym. J.*, vol. 17, no. 6, pp. 451–477, 2008.
- [12] A. Rudin and P. Choi., *The Elements of Polymer Science and Engineering*, 3rd ed. USA: Academic Press, 2012.
- [13] M. Koleva, "Polymethyl methacrylate (PMMA)," *Technical University of Gabrovo*. [Online]. Available: <http://webhotel2.tut.fi/projects>

- /caeds/tekstit/plastics/plastics_PMMA.pdf. [Accessed: 31-Oct-2015].
- [14] MDDI, "Acrylic polymers: a clear focus," *UBM Canon*, 1996. [Online]. Available: <http://www.mddionline.com/article/acrylic-polymers-clear-focus>. [Accessed: 23-Mar-2017].
- [15] "The universal selection source: plastics & elastomers," *SpecialChem*, 2017. [Online]. Available: <https://www.specialchem.com/about-specialchem>. [Accessed: 27-Mar-2017].
- [16] M. Koleva, "Polystyrene (PS)." [Online]. Available: http://webhotel2.tut.fi/projects/caeds/tekstit/plastics/plastics_PS.pdf. [Accessed: 04-Apr-2017].
- [17] W.-F. Su, "Polymer size and polymer solutions," in *Principles of Polymer Design and Synthesis*, 1st ed., Springer-Verlag Berlin Heidelberg, 2013, p. 306.
- [18] "Polymer properties database," 2015. [Online]. Available: <http://polymerdatabase.com/index.html>. [Accessed: 04-Apr-2017].
- [19] D. Hutanu, M. D. Frishberg, L. Guo, and C. C. Darie, "Recent applications of polyethylene glycols (PEGs) and PEG derivatives," *Mod Chem appl*, vol. 2, no. 2, pp. 1–6, 2014.
- [20] "Polyethylene Glycol," *AroKor Holdings Inc.*, 2013. [Online]. Available: www.chemicaland21.com. [Accessed: 07-Apr-2017].

- [21] J. Lewalter, G. Skarping, D. Ellrich, and U. Schoen, "Polyethylene glycol," *MAK Collect. Occup. Heal. Saf.*, vol. 10, pp. 248–270, 2012.
- [22] T. Benanti and D. Venkataraman, "Organic solar cells : an overview focusing on active layer morphology," *Photosynth. Res.*, vol. 87, pp. 73–81, 2006.
- [23] Z. Chen, W. Li, R. Li, Y. Zhang, G. Xu, and H. Cheng, "Fabrication of highly transparent and conductive indium-tin oxide thin films with a high figure of merit via solution processing.," *Langmuir*, vol. 29, pp. 13836–42, 2013.
- [24] C. S. Suchand Sangeeth, M. Jaiswal, and R. Menon, "Correlation of morphology and charge transport in poly(3,4-ethylenedioxythiophene)-polystyrenesulfonic acid (PEDOT-PSS) films.," *J. physics. Condens. Matter*, vol. 21, no. 7, p. 72101, 2009.
- [25] M. T. Dang, G. Wantz, H. Bejbouji, M. Urien, O. J. Dautel, L. Vignau, and L. Hirsch, "Polymeric solar cells based on P3HT: PCBM: Role of the casting solvent," *Sol. Energy Mater. Sol. Cells*, vol. 95, no. 12, pp. 3408–3418, 2011.
- [26] S. Gunes, N. Helmut, and N. Sariciftci, "Conjugated polymer-based organic solar cells," *Chem. Rev.*, vol. 107, no. 4, pp. 1324–1338, 2007.
- [27] T. Wang, A. J. Pearson, D. G. Lidzey, and R. A. L. Jones, "Evolution of structure, optoelectronic properties, and device performance of

- polythiophene: fullerene solar cells during thermal annealing," *Adv. Funct. Mater.*, vol. 21, no. 8, pp. 1383–1390, 2011.
- [28] M. C. Petty, *Molecular Electronics: From Principles to Practice*. Chichester: John Wiley & Sons, Ltd, 2007.
- [29] C. Waldauf, M. C. Scharber, P. Schilinsky, J. A. Hauch, and C. J. Brabec, "Physics of organic bulk heterojunction devices for photovoltaic applications," *J. Appl. Phys.*, vol. 99, no. 10, 104503, 2006.
- [30] J. Wang and B. Qi, "Fill factor in organic solar cells," *Phys. Chem. Chem. Phys.*, vol. 15, no. 23, pp. 8972–8982, 2013.
- [31] G. Yu, J. Gao, J. Hummelen, F. Wudl, and A. Heeger, "Polymer photovoltaic cells - enhanced efficiencies via a network of internal donor-acceptor heterojunctions," *Science.*, vol. 270, no. 5243, pp. 1789–1791, 1995.
- [32] J.-L. Brédas, J. Norton, J. Cornil, and V. Coropceanu, "Molecular understanding of organic solar cells: the challenges," *Acc. Chem. Res.*, vol. 42, no. 11, pp. 1691–1699, 2009.
- [33] P. Blom, V. Mihailetschi, J. A. Koster, and D. Markov, "Device physics of polymer: fullerene bulk heterojunction solar cells," *Adv. Mater.*, vol. 19, no. 12, pp. 1551–1566, 2007.
- [34] H. Nicolai, M. Kuik, G. Wetzelaer, B. De Boer, C. Campbell, C.

- Risko, J. Brédas, and P. Blom, "Unification of trap-limited electron transport in semiconducting polymers," *Nat. Mater.*, vol. 11, no. 10, pp. 882–887, 2012.
- [35] H. L. Yip and A. K. -Y Jen, "Recent advances in solution-processed interfacial materials for efficient and stable polymer solar cells," *Energy Environ. Sci.*, vol. 5, pp. 5994–6011, 2012.
- [36] G. Li, V. Shrotriya, J. Huang, Y. Yao, T. Moriarty, K. Emery, and Y. Yang, "High-efficiency solution processable polymer photovoltaic cells by self-organization of polymer blends," *Nat. Mater.*, vol. 4, no. 11, pp. 864–868, 2005.
- [37] T. Owen, *Fundamentals of UV-visible spectroscopy*. Germany: Agilent Technologies, 2000.
- [38] H.-J. Butt, B. Cappella, and M. Kappl, "Force measurements with the atomic force microscope: technique, interpretation and applications," *Surf. Sci. Rep.*, vol. 59, no. 1–6, pp. 1–152, 2005.
- [39] H.-Q. Li, "The common AFM modes," 1997. [Online]. Available: <http://www.chemistry.uoguelph.ca/educmat/chm729/afm/details.htm>. [Accessed: 03-Feb-2017].
- [40] F. J. Giessibl, "Advances in atomic force microscopy," *Rev. Mod. Phys.*, vol. 75, no. 3, pp. 949–983, 2003.
- [41] B. Stuart, *Infrared Spectroscopy: Fundamentals and Applications*.

John Wiley & Sons, Ltd, 2004.

- [42] M. Reese, S. Gevorgyan, M. Jørgensen, E. Bundgaard, S. Kurtz, D. Ginley, D. Olson, M. Lloyd, P. Morvillo, E. Katz, A. Elschner, O. Haillant, T. Currier, V. Shrotriya, M. Hermenau, M. Riede, K. R. Kirov, G. Trimmel, T. Rath, O. Inganäs, F. Zhang, M. Andersson, K. Tvingstedt, M. Lira-Cantu, D. Laird, C. McGuinness, S. Gowrisanker, M. Pannone, M. Xiao, J. Hauch, R. Steim, D. DeLongchamp, R. Rosch, H. Hoppe, N. Espinosa, A. Urbina, G. Yaman-Uzunoglu, J. Bonekamp, O. Bernd, A. Van Breemen, C. Girotto, E. Voroshazi, and F. C. Krebs, "Consensus stability testing protocols for organic photovoltaic materials and devices," *Sol. Energy Mater. Sol. Cells*, vol. 95, no. 5, pp. 1253–1267, 2011.

CHAPTER 5

THE DEGRADATION OF P3HT: PCBM DEVICES STORED UNDER DIFFERENT ATMOSPHERIC CONDITIONS

5.1 Introduction

As noted in Chapter 3, there are many effects cause degradation in OPVs, such as the diffusion of water, oxygen, metal or In into the active layer. One means to facilitate the understanding of the major reasons behind a short lifetime in OPVs is to study and compare their degradation behaviour in different environments. This chapter contrasts the degradation behaviour of OPV devices stored in ambient and inert environments.

5.2 The effect of ambient environment on the device lifetime

The first aim of this study was to reveal the effect of ambient conditions on the lifetime of standard devices. Devices were stored in two conditions of ambient environments:

- Controlled environment, where humidity and temperature were fixed at ~50% RH and 21°C.
- Un-controlled environment, where the humidity and temperature were not controlled (laboratory conditions).

Eight devices were fabricated, as described in section 4.3. Four of these were stored in an ambient controlled environment, while the other four devices were stored in an environment of laboratory conditions. Figure 5.1 compares the typical J-V curves of devices stored in the two different environments.

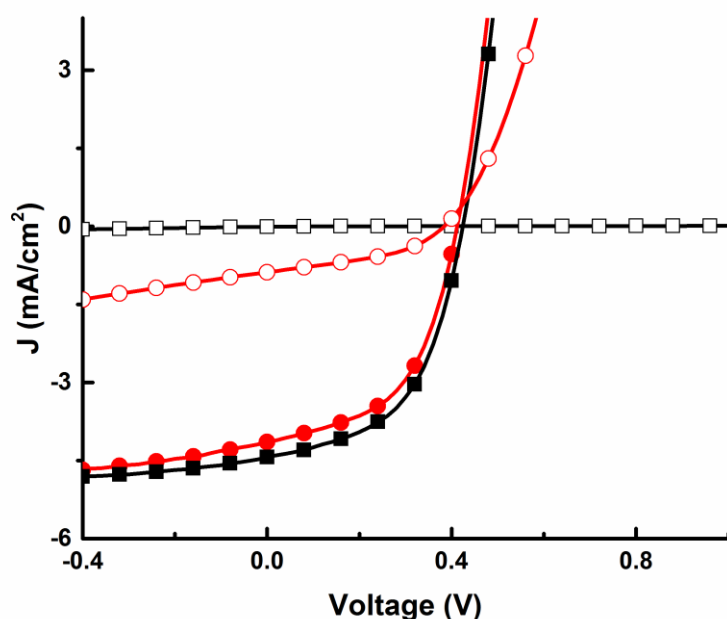


Figure 5.1. J-V curves, under illumination, for devices stored in laboratory conditions (black squares) and a controlled environment (red circles). Closed symbols represent the initial measurements, and open symbols represent devices after aging for 96 h.

The initial measurements for both devices revealed approximately the same power conversion efficiency ($\sim 0.9\%$). Degradation was observed in both devices, as illustrated in figure 5.1. However, the devices stored in normal laboratory conditions exhibited a more rapid degradation. It was observed that the PCE dropped quickly, reaching less than 10% of its original value within 72 h, compared to 96 h for devices

stored in a controlled environment. This result indicates that changes in the atmospheric conditions could influence the degradation mechanisms.

All the devices in this thesis after this experiment were stored in the controlled ambient environment with RH \sim 50% and 21°C which is briefly called "ambient environment."

5.3 Degradation of standard devices in different environments

In order to elucidate the reasons behind the rapid degradation of devices stored in an ambient environment, two sets of eight standard devices were fabricated and tested after being stored in a controlled, ambient environment as in the previous experiment and in an inert gas environment in a glovebox.

5.3.1 Variation in lifetime of standard devices

The lifetimes of the devices stored in a controlled ambient environment in this set of experiments and in the previous experiment were found to be different. The PCE of devices in the first experiment (section 5.2) reached less than 10% of their initial performance in \sim 96 h while in this experiment \sim 192 h. Generally, a variation in the values of lifetime of standard devices stored in an ambient environment was noticed in most experiments in this thesis. Sometimes, the lifetime was shorter than 192 h and sometimes was longer. Although all the

experiments were done with care, it was difficult to achieve the same results, perhaps for two reasons:

(a) Fabrication process

It was difficult to control some fabrication parameters such as spinning speed, spinning and annealing time (the spinner used is a home made). This is because these parameters were controlled manually (the accuracy of the measurements were approximately ± 100 rpm, ± 2 s and ± 2 min, respectively). In addition, the quality of Al layer also may change from batch to batch due to a variation that might have occurred in the deposition rate of the Al on the active layer.

(b) Environmental conditions

There was a slight variation in the level of humidity in the ambient environment ($\sim 10\%$) where OPV devices were stored for lifetime measurements. This variation may cause a change in the lifetime.

5.3.2 Changes in electrical parameters

Figure 5.2 compares typical J-V curves from the two sets of devices. The results indicate that the initial performance of devices from the two sets was approximately the same. A substantial difference in performance was observed after aging in the different environments. In the ambient environment, the PCE dropped to more than 80% after 192 h. However, the PCE for the devices stored in the inert environment was

almost unchanged, with 90% of the initial performance retained after 1488 h.

From these results, it can be concluded that the degradation in the performance of devices stored in the ambient environment was likely related to the presence of water and oxygen. It was found that both J_{sc} and V_{oc} were responsible for the degradation (Figure 5.2).

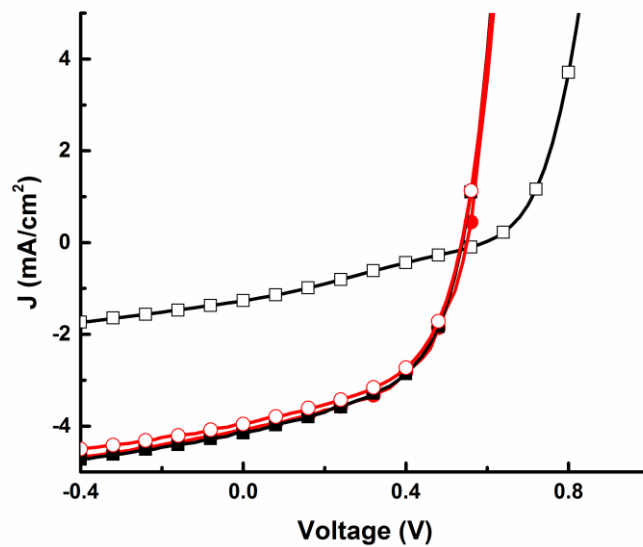


Figure 5.2. J-V curves, under illumination, for devices stored in an ambient environment (black squares) and an inert environment (red circles). Closed symbols represent the initial measurements, and open symbols after aging for 190 hours.

These results suggest that the diffusion of water and oxygen into the active layer may induce chemical degradation in the active layer, leading to a decrease in carrier generation and/or increase in recombination. However, this chemical degradation mechanism involving water and oxygen has a much lower chance of occurring in the devices stored in an inert environment.

5.3.3 UV-vis absorption

The absorption spectra of blended films for devices stored in inert and ambient environments were measured, as-deposited and after aging for 192 h. Figure 5.3 shows the spectra between 400 nm and 610 nm which is attributed to the absorption of P3HT. The spectra reveal a peak at 510 nm and two vibronic absorption shoulders at 551 nm and 602 nm. Devices stored in an ambient environment showed a decrease in absorption across the wavelength range studied, as illustrated in Figure 5.3. This reduction may be attributed to bleaching of the absorption band the P3HT chains [6], which may also cause a decrease in J_{sc} [1]. In contrast, for devices stored in an inert environment, the spectrum was stable. This finding indicates that storing the device in an ambient environment may affect the optical properties of P3HT.

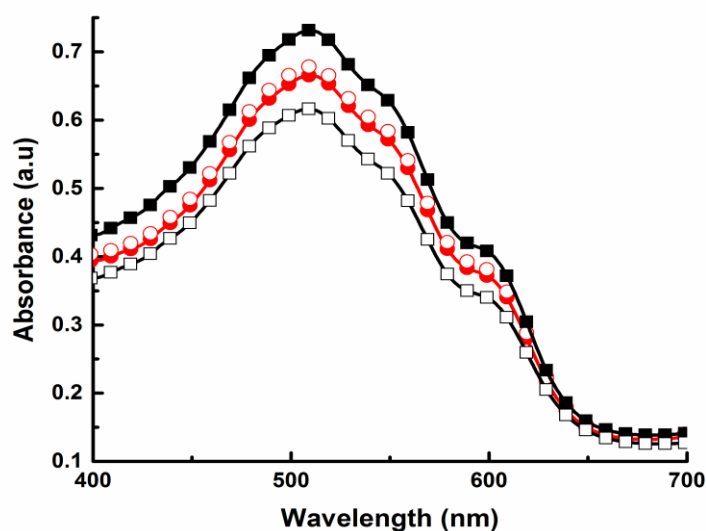


Figure 5.3 UV-vis absorption spectra for standard devices stored in an ambient environment (black squares), and in an inert environment (red circles). Closed symbols represent the spectra as-deposited and open symbols after aging for 192 h.

5.4 Fourier transform infrared spectroscopy

From previous results, it appears that the main cause of the short lifetime in standard devices might be chemical degradation due to reactions with water and oxygen. Further analysis was therefore performed on blended films of P3HT: PCBM stored in an ambient environment using FTIR spectroscopy. This experiment was used to reveal information about specific functional groups that evolved during the aging process.

5.4.1 FTIR spectra of as – deposited P3HT: PCBM

A thin film sample of P3HT: PCBM was prepared and measured as described in section 4.5.5. The absorption spectrum of this film is illustrated in Figure 5.4. Table 5.1 lists the FTIR absorption bands for pristine P3HT and PCBM obtained from the literature.

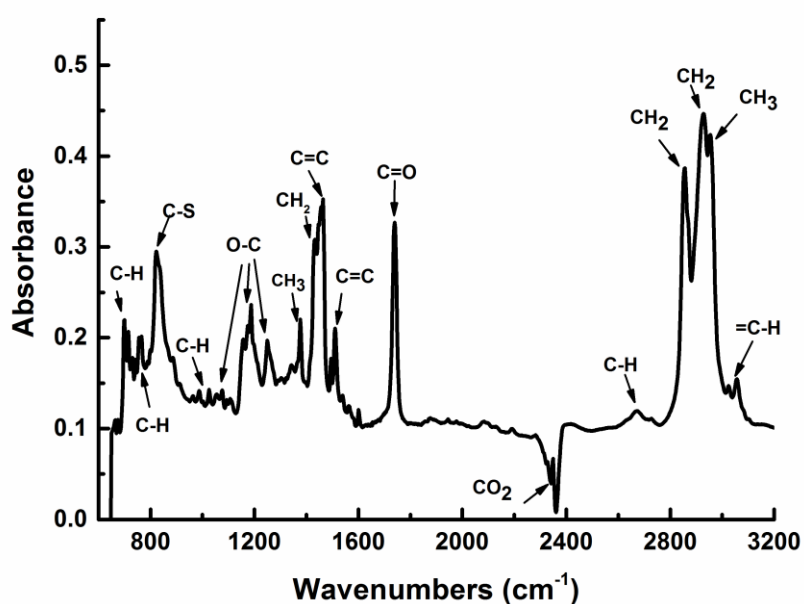


Figure 5.4. FTIR spectrum for an as-deposited film of P3HT: PCBM.

Table 5. 1 Assignments of the main FTIR absorption bands in pristine P3HT and PCBM

P3HT Wavenumber (cm⁻¹)	Assignment	PCBM Wavenumber (cm⁻¹)	Assignment
725 [2]	=C-H bending	692 [3]	C-H bending
820 [3]	C-S stretching	1052-1250 [3]	O-C bending
1377 [4]	CH ₃ symmetrical bending	1424,1432 [3]	CH ₂ bending
1454 [4]	CH ₂ bending-CH ₃ asymmetrical bending	1732-1745 [3]	C=O Stretching
2855 [4]	CH ₂ symmetrical stretching	1800-1840 [2]	C=O stretching
2870 [4]	CH ₃ stretching		
2924 [4]	CH ₂ asymmetrical stretching		
2954 [4]	CH ₃ asymmetrical stretching		
3055 [4]	=C-H stretching		

The spectrum was consistent with that reported in the literature (Table 5.1). However, two additional bands were evident, in the range 900-960 cm⁻¹ and at 2680 cm⁻¹. These bands indicate the presence of C-H bending and C-H stretching vibrations, respectively [2]. The appearance of these bands agrees with results from Shrotriya et al. [5], who suggested that this was due to a change in vibration energy, which might result from charge transfer between the P3HT and PCBM molecules [5].

5.4.2 FTIR spectra of degraded P3HT: PCBM

It has been reported in the literature that chemical degradation causes the disappearance of some functional groups and the appearance of new functional groups, as summarized in Table 5.2.

Table 5. 2 Evidence for degradation effects in the FTIR spectra of P3HT: PCBM, as described in references [4].

Degradation products	Indication	Wavenumber (cm⁻¹)
Alkyl group	Disappear or decrease	3000-2850
Thiophene ring	Disappear or decrease	1510, 1454
Aromatic groups	Disappear or decrease	3055,820
Carbonyl group	Appear	1775,1715,1675, and 1620
OH stretching of alcohols + hydroperoxides	Appear	3460
O-O stretching	Appear	880
Acid fluorides	Appear	1840
Thiophene carboxylic acid	Appear	1670

To observe changes in the functional groups present in an aged P3HT: PCBM film, the FTIR spectrum for a pristine film is compared to that for the film after it had been stored in an ambient environment for 840 h in Figure 5.5 (a). The absorptions for three important functional groups in the P3HT: PCBM film, aromatic C-H groups, thiophene rings and alkyl groups, are expanded for illustration, and presented in Figure 5.5 (b), (c), and (d).

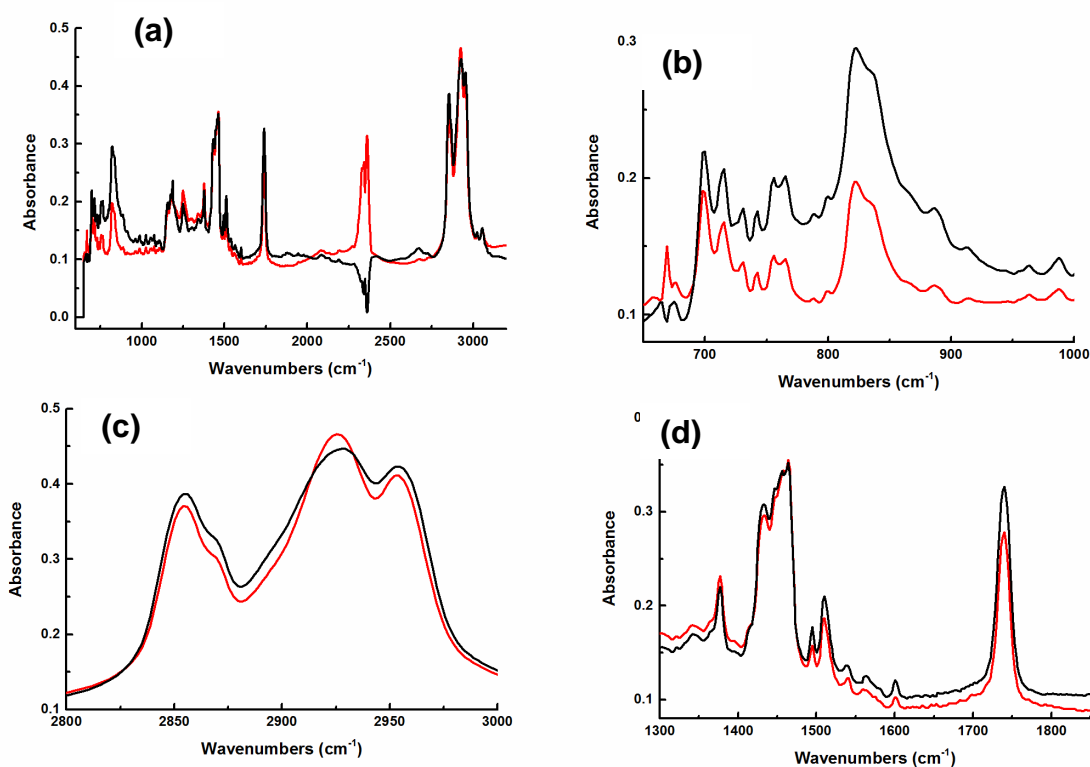


Figure 5.5. FTIR spectra of a P3HT:PCBM film stored in an ambient environment. (a) full range of measurement and the expanded regions of: (b) aromatic groups, (c) thiophene rings, and (d) alkyl groups. The black line represents the spectra as deposited, and the red line was recorded after 840 h.

In general, no new spectral bands were seen in the aged film. However, there was a decrease in the intensity of the bands assigned to aromatic C-H groups, at 700-990 cm^{-1} , and at 900-960 cm^{-1} , which may indicate a decrease in the charge transfer between the P3HT and PCBM molecules. Also, there was an increase in the intensity of the bands at 660-676 cm^{-1} . These bands are related to PCBM, indicating that some re-ordering may have occurred in the PCBM component.

In the spectral range 1300-1850 cm^{-1} , there was a slight decrease in the intensities attributed to the thiophene rings at 1510 cm^{-1} , while no change was observed in the intensity at 1454 cm^{-1} , which indicates that

no modification occurred to the thiophene rings after 840 h. However, there was a decrease in the intensity of the ester band at 1736 cm^{-1} , indicating that the PCBM was slightly affected. No noticeable decrease occurred in the intensity of the bands assigned to alkyl groups ($2800\text{-}3000\text{ cm}^{-1}$)

The chemical degradation mechanisms which were explained in Chapter 3, should result in two relevant degradation products: carbonyl and sulfur groups which were not seen in the present results. The FTIR showed that no observable oxidization reactions were occurring in the devices, after at least 840 h. This contrasts with the J-V characteristics and UV -Vis absorption spectra, as shown in Figure 5.2 and Figure 5.3, respectively. The devices degraded rapidly, within 192 h, when stored in an ambient environment. These contradicting results may indicate that there is another, faster, degradation mechanism taking place in the device. Another reason might be that the sensitivity of the FTIR measurement used here may not be sufficient to detect the minor chemical changes that occurred in these films.

On the other hand, the disagreement between the results and the literature may be attributed to differences in the storage conditions. According to the literature, most studies that used the FTIR technique tested devices under illumination conditions [4][6][7]. The samples in this study were stored in the dark. Oxidization reactions are accelerated in the presence of light and occur more slowly in the dark.

5.5 Conclusion

The results presented in this chapter indicate that water and oxygen from the environment are the primary causes of device degradation. It was found that in the absence of water and oxygen (inert environment); the lifetime of the device was relatively long compared with devices stored in the ambient environment. In FTIR spectroscopy, no new bands or shifts in the spectra were observed, indicating that no observable chemical degradation of the P3HT and PCBM had occurred. However, the decrease in the intensity of the absorptions assigned to some functional groups revealed that there was a reduction in the strength of the chemical bonds and/or a decrease in the strength of charge transfer between the molecules, causing degradation.

5.6 References

- [1] Q. Wu, M. Bhattacharya, L. M. J. Moore, and S. E. Morgan, "Air processed P3HT: PCBM photovoltaic cells: morphology correlation to annealing, degradation, and recovery," *J. Polym. Sci. Part B Polym. Phys.*, vol. 52, no. 23, pp. 1511–1520, 2014.
- [2] B. Stuart, *Infrared Spectroscopy: Fundamentals and Applications*. Australia: John Wiley & Sons, Ltd, 2004.
- [3] G. Kalonga, G. Chinyama, M. Munyati, and M. Maaza, "Characterization and optimization of poly (3-hexylthiophene-2, 5-diyl) (P3HT) and [6, 6] phenyl-C₆₁-butyric acid methyl ester (PCBM) blends for optical absorption," *J. Chem. Eng. Mater. Sci.*, vol. 4, no. 7, pp. 93–102, 2013.
- [4] M. Manceau, A. Rivaton, J. L. Gardette, S. Guillerez, and N. Lemaître, "The mechanism of photo- and thermooxidation of poly(3-hexylthiophene) (P3HT) reconsidered," *Polym. Degrad. Stab.*, vol. 94, no. 6, pp. 898–907, 2009.
- [5] V. Shrotriya, J. Ouyang, R. J. Tseng, G. Li, and Y. Yang, "Absorption spectra modification in poly (3-hexylthiophene): methanofullerene blend thin films," *Chem. Phys. Lett.*, vol. 411, pp. 138–143, 2005.
- [6] A. Rivaton, S. Chambon, M. Manceau, J. L. Gardette, N. Lemaître, and S. Guillerez, "Light-induced degradation of the active layer of polymer-based solar cells," *Polym. Degrad. Stab.*, vol. 95, no. 3,

pp. 278–284, 2010.

- [7] A. Dupuis, P. Wong-Wah-Chung, A. Rivaton, and J. L. Gardette, "Influence of the microstructure on the photooxidative degradation of poly(3-hexylthiophene)," *Polym. Degrad. Stab.*, vol. 97, no. 3, pp. 366–374, 2012.

CHAPTER 6

TERNARY OPVs BASED ON P3HT: PCBM: PMMA

6.1 Introduction

The results presented in Chapter 5 revealed that storing devices in an ambient environment had a large effect on their lifetime. It was shown that the presence of water and oxygen degraded the performance of OPVs. To reduce this degradation, a ternary blend system, comprising P3HT and PCBM blended with an insulating polymer was investigated. However, there are very few studies that use insulating polymers as the third component in ternary blend OPVs [1]. This is because it was feared that the addition of an insulating polymer would disrupt the network structure formed between donor and acceptor, leading to reduce charge transport efficiency and poor performance [1], [2]. Furthermore, reducing the concentration of the donor and acceptor components lowers the optical absorbance of the active layer [2], perhaps leading to poor performance.

The above approach has already been used in organic field-effect transistors (OFETs), where it has been shown that insulating polymers can increase the lifetime with minimal effect on the electronic properties of these devices [2], [3]. In the case of OPVs, there have only been a few studies which have used this method. Most work that has used insulating polymers investigated the effects on the device performance rather than the device lifetime. Studies have generally demonstrated that

incorporating insulating polymers may cause either a slight degradation in the photovoltaic properties [2], [4], or enhance the device performance [1], [2], [5]. For example, Ferenczi et al. [2] showed that adding up to 50 wt% of high-density polyethylene (HDPE) or isotactic polystyrene (i-PS) to P3HT: PCBM OPVs had a minimal detrimental effect on initial device performance. In contrast, Wu et al. [1] have demonstrated that adding PMMA (9 wt%) to a P3HT: PCBM blend can actually improve the initial fill factor and open circuit voltage of the resulting OPV. This was suggested to be due to a reduced number of vacancies and leakage pathways.

In this Chapter, PMMA was used as a ternary component in P3HT: PCBM devices. Initially, it was important to observe the effect of PMMA on device performance before studying the degradation behavior in this type of OPVs. Therefore, the initial experiments study the effect of PMMA on the performance of ternary OPVs, while the follow-up work investigates the effect of PMMA on the device lifetime.

6.2 Effect of PMMA on the performance of P3HT: PCBM devices

OPVs based on binary and ternary blend films were fabricated as described in section 4.3. Ternary blends with equal weight ratio (1:1) of P3HT: PCBM and percentage by mass of PMMA of 0 wt%, 2 wt%, 5 wt%, 8 wt%, 10 wt%, 14 wt%, and 16 wt% were used. Four devices for each weight ratio of PMMA were prepared, and the measurement of initial performance was performed on all the OPVs.

6.2.1 Electrical characteristics of ternary devices

Figure 6.1 illustrates the J-V curves under illumination for devices containing different amounts of PMMA.

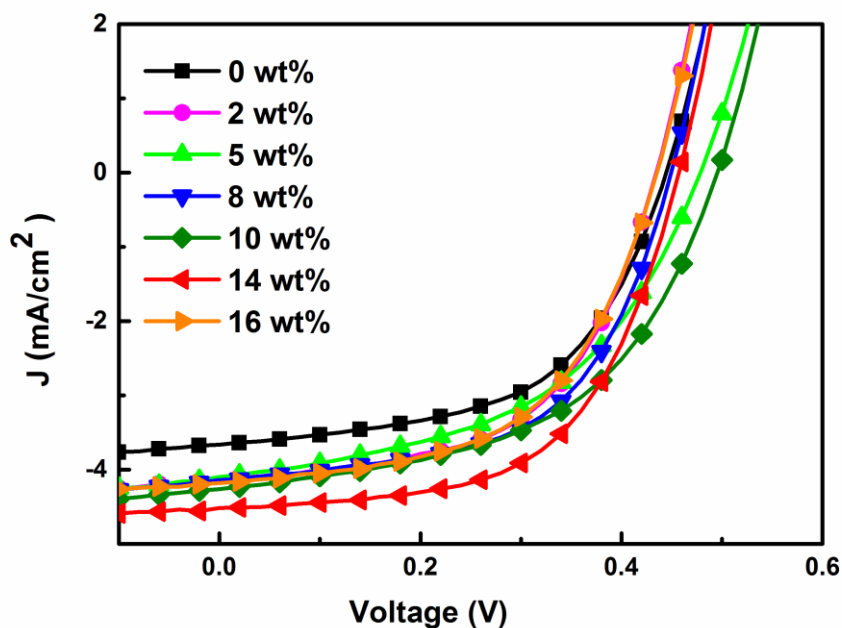


Figure 6.1. J-V curves under illumination for devices with different PMMA content.

It is evident that the addition of PMMA can improve the power conversion efficiency. Table 6.1 summarizes the average values of the electrical parameters for devices containing different fractions of PMMA. Compared with binary devices, both the FF and V_{OC} of ternary devices were slightly improved. However, the noticeable improvement in the power conversion efficiency was mainly due to an increase in J_{sc} .

Table 6.1 Summary of the average values for basic device parameters of binary and ternary devices with different PMMA content.

PMMA (wt%)	V_{oc} (V)	J_{sc} (mA/cm ²)	FF (%)	PCE (%)
0	0.45 ± 0.01	3.76 ± 0.3	53 ± 1	0.9 ± 0.1
2	0.45 ± 0.01	4.17 ± 0.4	54 ± 1	1.0 ± 0.1
5	0.46 ± 0.02	4.23 ± 0.2	54 ± 1	1.1 ± 0.1
8	0.44 ± 0.02	4.05 ± 0.1	53 ± 1	0.95 ± 0.1
10	0.47 ± 0.01	4.46 ± 0.1	55 ± 1	1.2 ± 0.1
14	0.47 ± 0.01	4.77 ± 0.1	56 ± 2	1.3 ± 0.2
16	0.43 ± 0.01	4.20 ± 0.2	52 ± 2	0.94 ± 0.1

It was observed that the current density increased steadily as the amount of PMMA increased up to 14 wt%. Further increase of PMMA (16 wt%) caused a decrease in all parameters, possibly because the PMMA is electrically insulating.

Further electrical measurements were carried out on the binary and ternary devices to establish why the device performance was improved by the addition of PMMA. Figure 6.2 compares typical dark J-V curves for a binary device and a ternary device containing 14 wt% PMMA.

Three distinct regions appeared under forward bias. The first region (I) is at low voltages ($V < 0.16$ V) and is known as the leakage current region [6], where the current density (J) is limited by the shunt resistance (R_{sh}) [7], [8].

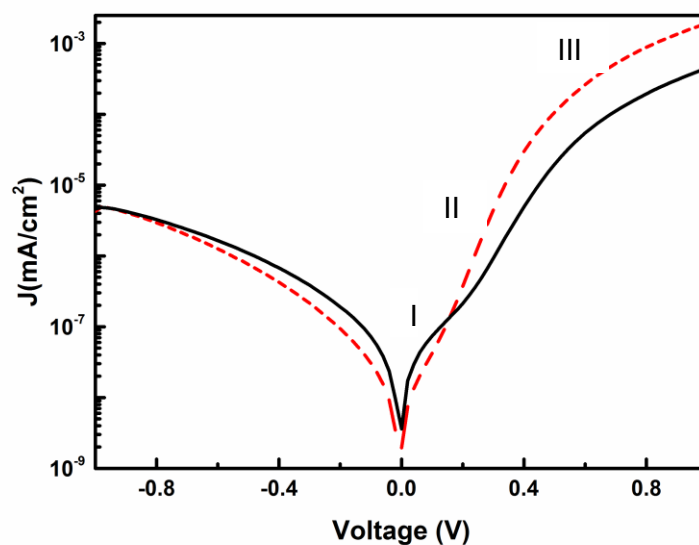


Figure 6.2. Dark J-V curves for a binary device, P3HT: PCBM (50:50), (black line), and a ternary device, 86 wt% (50:50 P3HT: PCBM):14 wt% PMMA (red dashed line).

It is evident in Figure 6.2 that the current in the binary device is greater than that in the ternary device, which possibly indicates that the leakage current density is lower in the ternary device [9]. The addition of PMMA may lead to a morphology where leakage is minimised. A similar suggestion was made by Wu et al. [1], where high R_{sh} is argued to be due to fewer leakage pathways existing in PMMA devices (as it also observed in Figure 6.2 region I) due to the ability of PMMA to suppress the formation of vacancies and reduce traps that may hinder charge transport. Moreover, a lower leakage current and recombination suggests a good interfacial morphology between the electrodes and the active layer, leading to an improvement in J_{sc} [7].

For voltages between 0.16 V and 0.7 V, an exponential region can be distinguished as a straight line (region II). It appears that the current

in the ternary devices is higher than that in the binary devices, indicating that the injected current is greater in ternary devices [6]. The third distinct region (region III) is at high voltage (>0.7 V), where the current is dominated by the series resistance (R_s), which is associated with the bulk resistance of the active layer and the resistance of the contacts between the electrodes and the active layer [7]. R_s can be calculated from the inverse slope of the J-V curve in the dark at a voltage greater than 0.7 V, where the J-V curve is linear. For ternary devices, R_s is smaller than for binary devices ($1.37 \Omega \text{ cm}^2$ vs. $6.4 \Omega \text{ cm}^2$). This indicates that the PMMA reduces the resistivity of the device by either reducing the contact resistance between the electrodes and the active layer or by reducing the resistivity of the active layer. The isolated PMMA may reduce the contact between the Al and the active layer (as explained in the next section), resulting in lower contact resistance [9]. The presence of PMMA might reduce traps in the active layer by reducing the diffusion of Al [10] and PEDOT: PSS [11] into the active layer, which in turn improves the FF and J_{sc} .

6.2.2 The morphology of ternary blend films

The film morphology was studied to understand the influence of PMMA on the structure of blended P3HT: PCBM films. The AFM height images shown in Figure 6.3 indicate that the addition of PMMA changed the surface morphology. When PMMA was added, circular islands were observed in the images, which increased in size as the percentage by mass of PMMA in the film was increased. The diameter of the islands was

in the range of 0.5 μm to 1.5 μm , while the height of the islands was 32-36 nm.

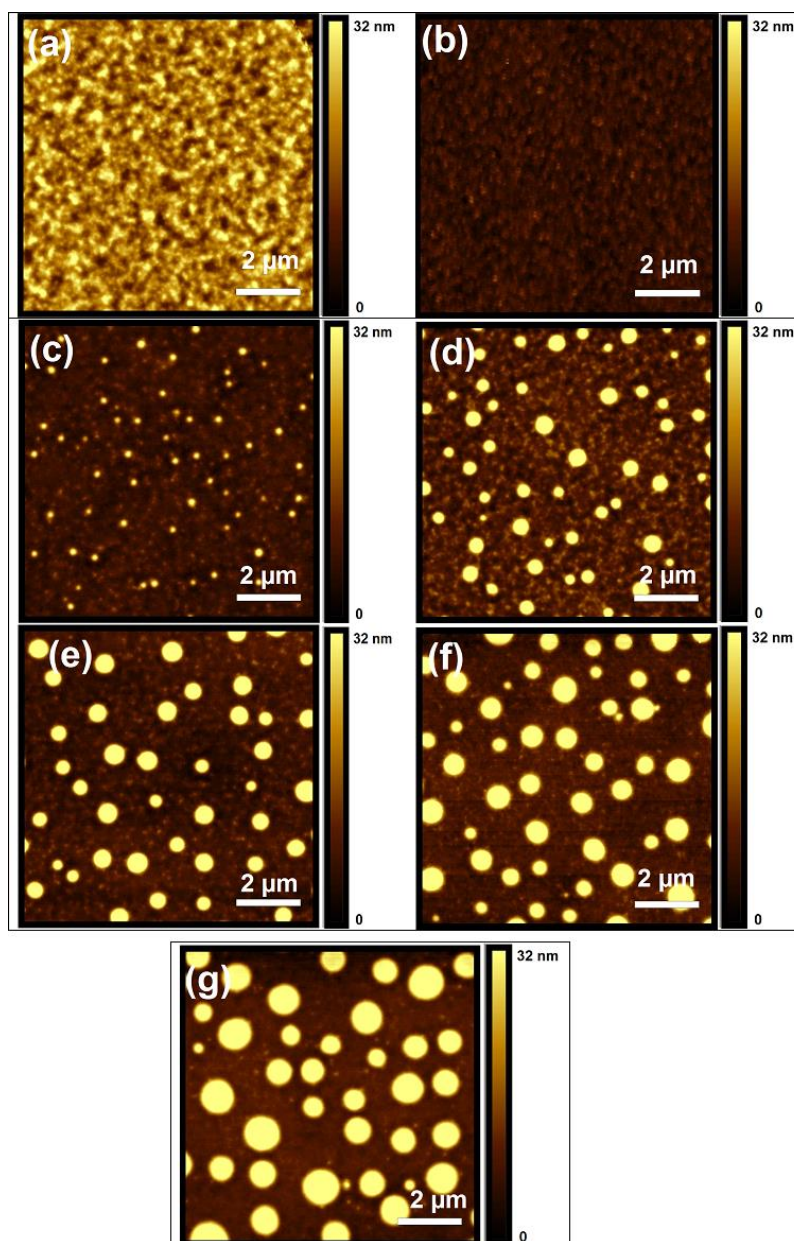


Figure 6.3. AFM topography images of P3HT: PCBM: PMMA ternary films with different percentage by mass of PMMA (a) 0 wt%, (b) 2 wt%, (c) 5 wt%, (d) 8 wt%, (e) 10 wt%, (f) 14 wt%, and (g) 16 wt%.

Profiles for the islands in films containing 5 wt%, and 14 wt% of PMMA are shown in Figure 6.4 (a). It is evident that there is no significant difference in the height of the islands in these two films,

indicating that there was no relationship between the concentration of PMMA and the height of the islands.

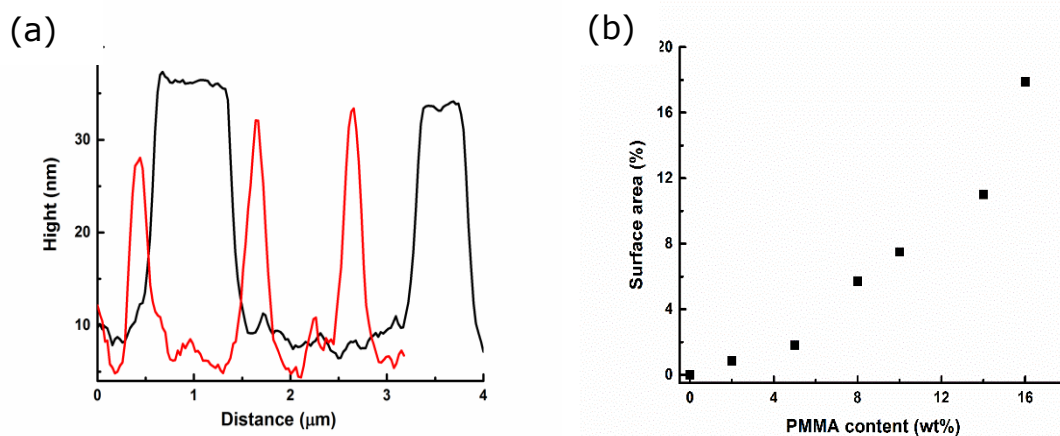


Figure 6.4 (a) Typical profiles for islands chosen from films containing 5 wt% (red), and 14 wt% of PMMA (black); (b) the surface area of the islands as a function of PMMA content (black).

However, the size of these islands increased as the mass percentage of PMMA increased. The topography images from Figure 6.3 were analyzed to determine the surface area of the islands as a fraction of the total surface area of the film. The results in Figure 6.4 (b) illustrate that as the amount of PMMA increased, the surface area of the islands increased.

By comparing this result with the performance data in Table 6.1, it is evident that the short circuit current density increased as the amount of PMMA increased, which leads to the conclusion that the J_{sc} was affected by the size of the islands. For further investigation, the (r.m.s) roughness of a ternary blend film (between the islands) was measured and compared with the active layer of the binary blend film (Table 6.2). Generally, the surface of the ternary film was smoother than that of the

binary film, while the surface roughness increased with increasing PMMA content, as shown in Table 6.2.

Table 6.2 The (r.m.s.) roughness and thickness of P3HT: PCBM: PMMA films containing different amounts of PMMA.

PMMA content (wt%)	(r.m.s) roughness (nm)	Film thickness (nm)
0	5.21	117
2	1.56	83
5	2.30	82
8	2.46	102
10	2.64	95
14	2.70	97
16	2.82	100

6.2.3 Phase separation in ternary blend film

As shown in Figure 6.3, the addition of PMMA to P3HT: PCBM films appear to result in two separate phases: the active materials and the insulating polymer. It seems that the PMMA molecules tend to aggregate rather than mix with the active polymers. The PMMA chains were ordered to form circular islands; and as the concentration of PMMA was increased, the size of the chains may increase leading to larger islands. This behavior was attributed to the chemical dissimilarity between the polymers [12]. The hydrophobic nature of PMMA means it has low wettability, and the polymer chains tend to accumulate [13]. In order to inspect the bottom surface of the active layer, a P3HT: PCBM: PMMA film was spin cast onto a PEDOT: PSS layer on a glass substrate. The

substrate was then immersed into deionized water until the PEDOT: PSS layer dissolved, allowing the P3HT: PCBM: PMMA layer to float off. The layer was then flipped over before being picked up onto a clean glass slide. The AFM image of this inverted film revealed that the PMMA does not segregate at the surface but penetrates the active layer, as shown in Figure 6.5.

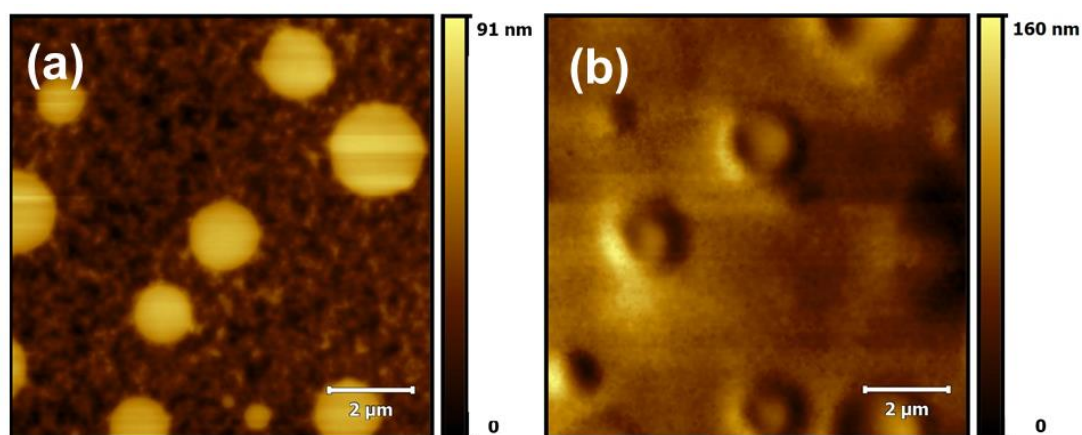


Figure 6.5. AFM topography images of a P3HT: PCBM: PMMA film taken from (a) front (b) back.

Further investigations of the ternary blend film were performed using focused ion beam (FIB) and field-emission scanning electron microscopy (FESEM). FIB cross-section cuts were made through the ternary films to study the separate phases in the film. The SEM image shown in Figure 6.6 reveals that the PMMA molecules accumulate and precipitate on the PEDOT: PSS surface, forming dome-like shapes.

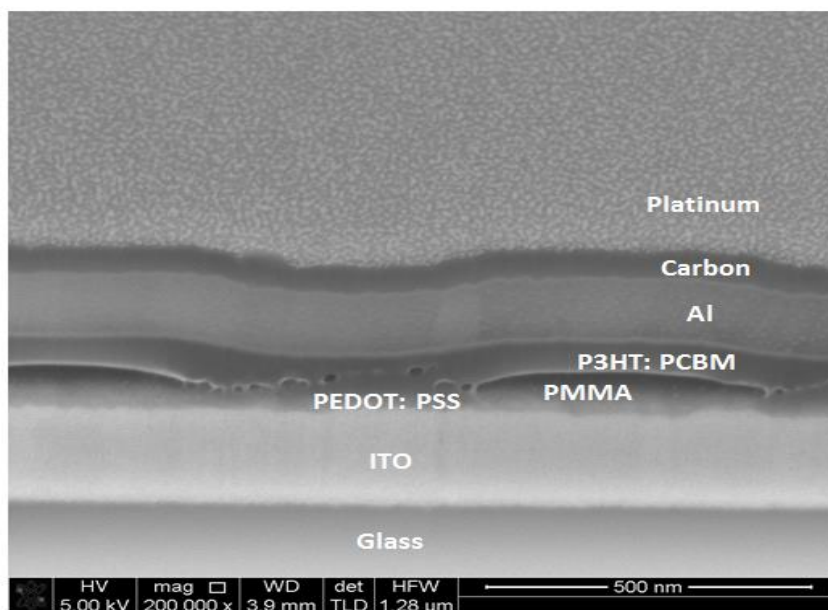


Figure 6.6. Cross-section SEM image of 86 wt% (50: 50 P3HT: PCBM) :14 wt% PMMA blend film.

These domes increase the thickness of the film and therefore when using AFM, island-like high spots were observed on the surface of the active layer. A schematic diagram for the resulting morphology is illustrated in Figure 6.7. The reason for the formation of this structure may be the difference in the solubility of the component polymers. The solubility of PMMA in DCB is lower than P3HT and PCBM. Hence, during spin casting, the solvent is quickly depleted from the PMMA domains, which begin to solidify as a layer on the substrate before the P3HT: PCBM active layer [14].

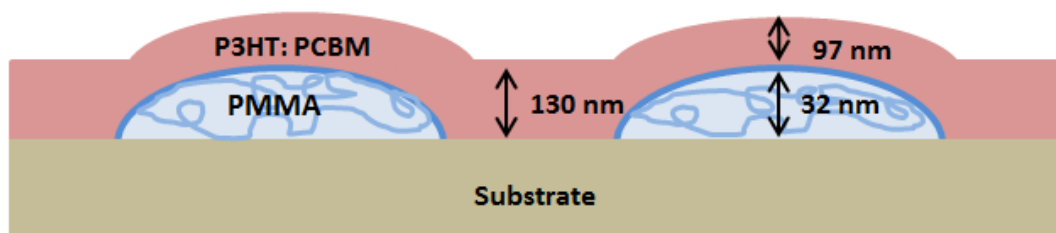


Figure 6.7. Schematic diagram of the morphology of a ternary film.

6.2.4 Absorption spectra of P3HT: PCBM: PMMA

The optical properties were studied by measuring the absorption spectra of binary and ternary blend films with different fractions of PMMA.

The results are presented in Figure 6.8.

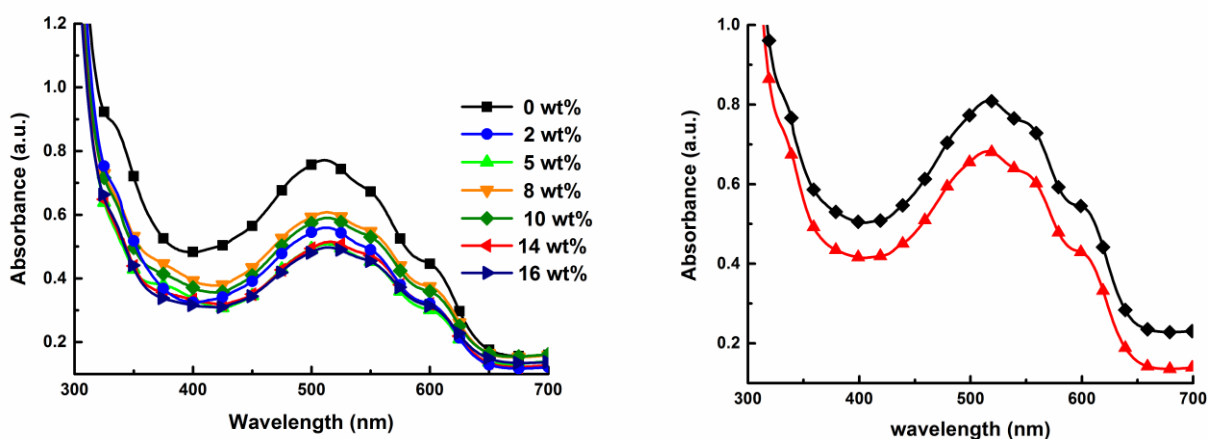


Figure 6.8. UV-vis absorption spectra of ternary blend films (a) containing different amounts of PMMA, (b) P3HT: PCBM (50:50) (black squares) and 86 wt% (50:50 P3HT: PCBM): 14 wt% PMMA films (red triangles) with the same thickness.

The absorption of light was reduced in the ternary films as the amount of PMMA was increased. This might be attributed to changes in the thickness of the film due to the concentration of the solution decreasing as the amount of PMMA was increased. An investigation revealed that the thickness of ternary films was slightly less than that of binary films, as shown in Table 6.2. However, absorptions at 601 nm and 550 nm are pronounced in all spectra, suggesting that the addition of PMMA does not affect the crystallization of P3HT. Further studies were performed by adjusting the film thickness of both binary and ternary films (the active layer with PMMA) to be equal at around 93 nm. The

result shown in Figure 6.8 (b) demonstrates that PMMA at 14 wt% reduced the light absorption and therefore reduces exciton generation, which would be expected to lead to a lowering of J_{sc} . However, this result contrasts with the observed performance of ternary devices (Table 6.1), which shows that ternary devices containing 14 wt% of PMMA have the highest value of J_{sc} . It is therefore apparent that the high performance of ternary devices was unlikely to be due to changes in light absorption or film thickness.

The above results show that PMMA reduces the absorption of light, and does not improve the crystallinity of P3HT. It is therefore unclear how PMMA enhances the performance of the devices. The change in morphology that PMMA induced in the film may enhance the molecular organization of P3HT and PCBM, leading to improved charge transport, or the addition of PMMA may reduce the number of traps and vacancies in the film, which in turn reduces the recombination rate [1]. Further work is clearly necessary to understand this phenomenon.

6.3 The effect of PMMA on the lifetime of P3HT: PCBM devices

In this section, the effect of PMMA on the lifetime of P3HT: PCBM devices was studied by testing the lifetime of devices based on a ternary blend containing 14 wt % of PMMA that were stored in environments with different humidity levels: 85%, 65%, 50% and 1% RH. An environmental chamber and a desiccator were used to achieve these levels of humidity, as described in section 4.6. A large number of devices were made and

stored as follows: 12 devices in 85% RH, 12 devices in 65% RH, 20 devices in 50% RH and 20 devices in 1% RH. The performance of all of the devices was monitored over time.

6.3.1 Lifetime measurements

The effect of humidity on the power conversion efficiency of the binary and ternary devices is illustrated in Figure 6.9. It is clear that the rate of degradation increases with humidity.

The PCE of devices stored under a relative humidity of 85% dropped very rapidly, with T_{20} less than 3 hours after initial operation. In contrast, the T_{20} lifetime increased to around 21 hours when the humidity was decreased to 65%. When the devices were stored under 50% RH, the PCE of both sets of devices dropped to zero after approximately 300 hours. At 1% RH, both sets of devices showed gradual degradation, and the PCE decreased significantly to less than 10% of its original value after 800 hours. The T_{80} and T_{20} lifetimes of the devices stored at different humidity levels are shown in Table 6.3. Both sets of devices were stored in an environment with ambient oxygen; the results agree with previous findings that the principal degradation mechanism in P3HT: PCBM OPVs, under normal operating conditions (i.e., ~40-50% RH), is due to interaction with water [15]. However, the lifetime of OPVs in 1% RH may only partly be limited by water and may be more affected by oxygen.

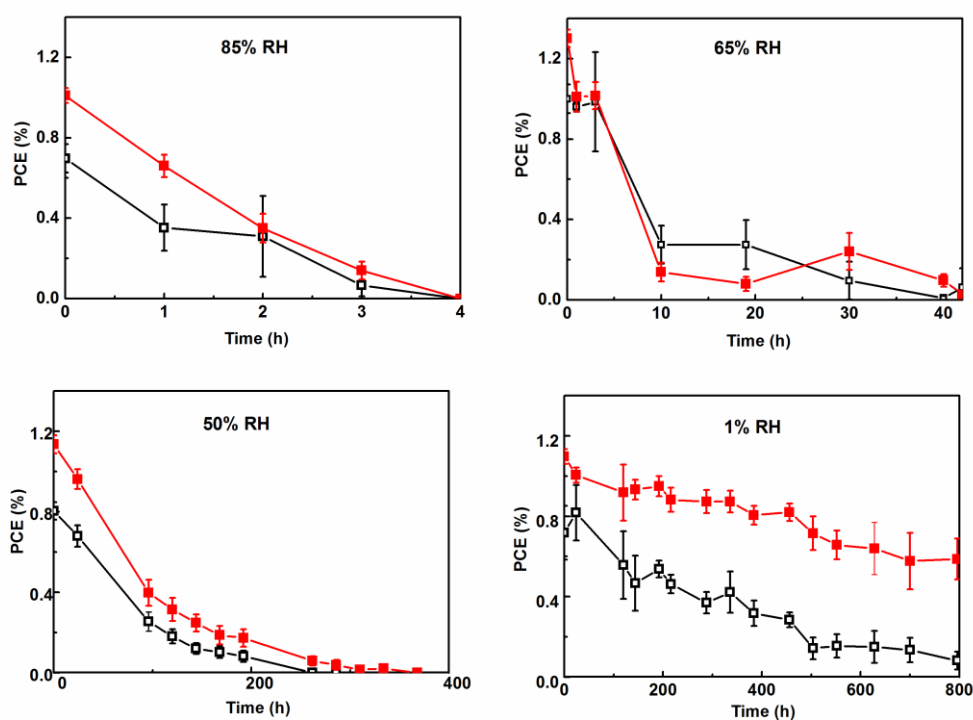


Figure 6.9. Power conversion efficiency as a function of time for P3HT: PCBM (50:50) binary blend, (open black squares), and 86 wt% (50: 50 P3HT: PCBM): 14 wt% PMMA, ternary blend (closed red squares) stored in environments with different humidity levels.

By comparing these data with the results presented in section 5.3, the devices stored in a dry N₂ environment showed no measurable drop in PCE after more than 1400 h.

Table 6.3 The lifetime of devices based on binary and ternary blends stored in environments with different humidity levels.

Humidity level	Binary devices		Ternary devices	
	T ₈₀ (h)	T ₂₀ (h)	T ₈₀ (h)	T ₂₀ (h)
65%	3	21	3	21
50%	24	120	24	168
1%	120	504	216	>1000

The above results revealed that the addition of PMMA to a P3HT:PCBM blend improved both the performance and lifetime of the devices. However, the improvement in the lifetime for a ternary device, when compared to an equivalent binary device, was shown to depend on RH. It was observed that when the devices were stored in 65% and 85 % RH, both the binary and ternary devices had the same lifetime. As the RH decreased to 50%, T_{20} was shown to be slightly higher in the ternary device, but if the RH was further reduced to 1%, both T_{20} and T_{80} were markedly better for the ternary OPV and T_{20} exceeded 1000 hours.

6.3.2 Electrical Characteristics

Further investigation into the electrical properties of aged ternary devices was carried out in an attempt to understand why PMMA improved the lifetime. Figure 6.10 shows typical J-V curves under illumination (a and b) and in the dark (c and d) for binary and ternary devices stored in 1% RH (a and c) and 50% RH (b and d).

The differences in the initial performance of the devices for 1% and 50% RH occur due to small variations in the thickness of the active layer. The thickness of the binary films was in the range 100-120 nm, while the thickness of ternary active films was in the range 90-110 nm. It is evident that V_{OC} remains relatively constant with aging at both humidity levels. The J_{sc} and FF were affected by aging in a 50% RH environment, while for devices aged in 1% RH, only J_{sc} was degraded.

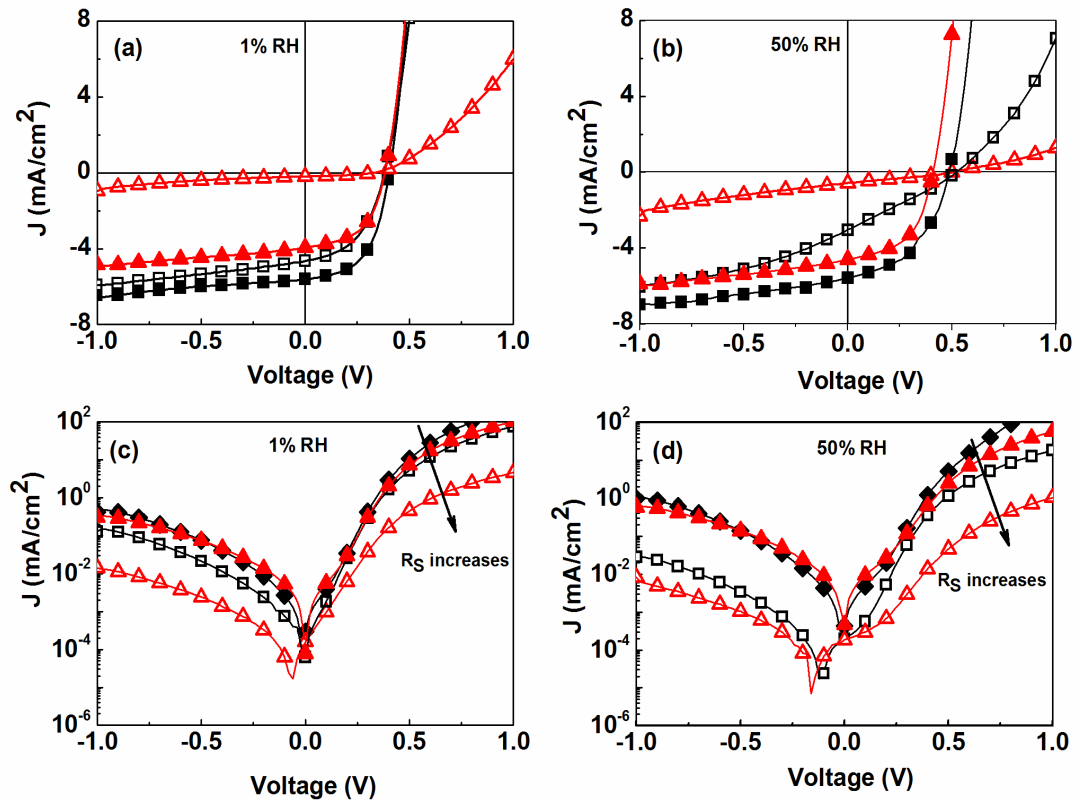


Figure 6.10. J-V curves under AM 1.5 (a & b) and in the dark (c & d) for typical binary P3HT: PCBM (50:50) (red triangles) and ternary 86 wt% (50: 50 P3HT: PCBM): 14wt% PMMA (black squares) OPVs. (a & c) devices stored in 1 % RH. Filled symbols for initial measurements, open symbols for aged devices (after 800 h). (b & d) devices stored in 50 % RH, devices aged for 260 h.

Table 6.4 lists the performance parameters for devices stored in 1% and 50% RH, for devices as-deposited and after 144 hours.

The dark current decreased with time in binary devices more than in ternary devices at both humidity levels, as shown in Figure 6.10 (c and d). This may indicate that the aging of P3HT: PCBM devices stored under 1% and 50% RH for over 1000 h involves the degradation of charge transport in either the P3HT or PCBM, suggesting the formation of traps.

Table 6.4 The average performance parameters of binary and ternary devices stored in 1% and 50% RH as-deposited and after 144 hours.

Humidity level (RH)	Time (Hours)	Device	V_{oc} (V)	J_{sc} (mA/cm ²)	FF (%)	PCE (%)
1%	0	Binary	0.39 ± 0.02	4.01 ± 0.6	50 ± 1	0.78 ± 0.1
		Ternary	0.39 ± 0.01	5.4 ± 0.2	52 ± 1	1.1 ± 0.1
	144	Binary	0.38 ± 0.04	2.6 ± 0.7	48 ± 1	0.47 ± 0.1
		Ternary	0.39 ± 0.01	4.9 ± 0.2	51 ± 1	0.97 ± 0.1
50%	0	Binary	0.43 ± 0.01	3.6 ± 0.2	51 ± 1	0.8 ± 0.1
		Ternary	0.45 ± 0.01	4.8 ± 0.1	53 ± 1	1.1 ± 0.2
	144	Binary	0.40 ± 0.04	0.95 ± 0.2	32 ± 3	0.12 ± 0.03
		Ternary	0.43 ± 0.03	1.5 ± 0.3	40 ± 1	0.26 ± 0.05

This conclusion is supported by the series resistance (R_s) which also changed with humidity. The ternary devices do not show significant differences in R_s , while a noticeable increase was observed in binary devices at both humidity levels, as shown in Table 6.5 and Figure 6.10(c and d). However, the increase in the series resistance may also be due to an increase in the contact resistance between the electrodes and the

active materials [7] due to the diffusion of oxygen and electrode materials into the active layer [16]. Ternary devices are shown to have better performance during aging tests. For example, after 144 hours in 50% RH, the ternary OPVs out-performed their binary counterparts in terms of R_s ($4.9 \Omega \text{ cm}^2$ vs. $83 \Omega \text{ cm}^2$), FF (40% vs. 32%), and J_{SC} (1.5 mA cm^{-2} vs. 0.95 mA cm^{-2}).

Table 6.5 Series resistance values for typical ternary and binary devices stored in 1% RH and 50% RH, for different aging times.

Time (Hours)	$R_s (\Omega \cdot \text{cm}^2)$			
	1% RH		50% RH	
	Ternary	Binary	Ternary	Binary
0	1.9	4.5	1.3	5.6
144	2.2	7.8	4.9	83
260	2.7	10	21.2	801
800	4.8	88	-	-

6.3.3 UV-Vis absorption

UV-Vis absorption spectra of ternary and binary thin films before and after aging were also measured and the results are shown in Figure 6.11. The absorbance of the ternary blend films was similar to that for the binary films, suggesting that the crystallization of P3HT was unaffected by the addition of PMMA. Moreover, no significant change in the absorption occurred after T_{20} and T_{80} , indicating that the crystallization of P3HT was unaffected by the aging process. The similar absorption characteristics of binary and ternary blends before and after aging also excludes photo-bleaching as a possible mechanism for the loss

in PCE shown in Figure 6.9. These results are in agreement with those obtained using FTIR, presented in section 5.4.2, which suggested that no oxidized species were present in the active layer after being stored for more than 800 h in an ambient environment.

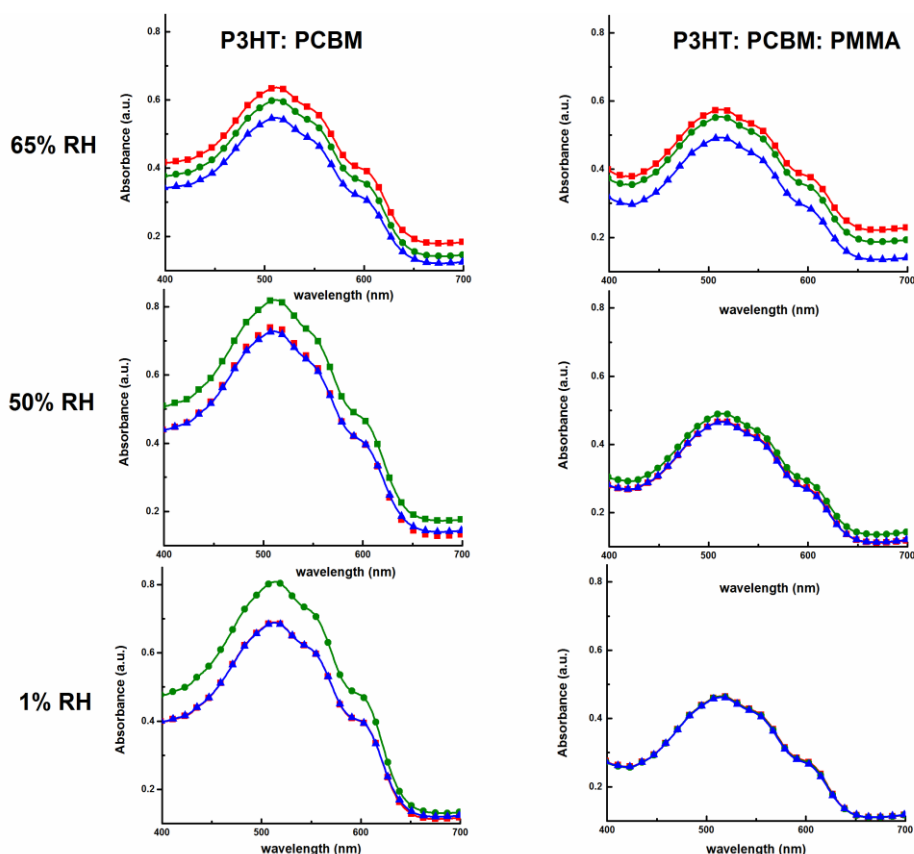


Figure 6.11. UV-visible absorbance spectra of P3HT:PCBM:PMMA and P3HT:PCBM blend films at different humidity levels. Red squares, as-deposited films; green circles, after T_{80} ; blue triangles, after T_{20} . The values of T_{80} and T_{20} are listed in Table 6.3.

These data suggest that the degradation observed in these devices is primarily electronic in origin, and strongly linked to the presence of water. Despite the absence of chemical changes seen in FTIR measurements, it was proposed that the main route for degradation was the formation of trap states through reactions with water [17], which has

the effect of reducing J_{sc} and FF. Furthermore, water can diffuse into the active layer through the PEDOT: PSS film [18] or the Al contact [19]. Kawano et al. [20] have shown that hygroscopic PEDOT: PSS is susceptible to degradation by water. They have revealed that absorption water by PEDOT: PSS caused an increase in series resistance. Hence the aging observed here may be due to a change in the PEDOT: PSS layer. The presence of PMMA on the surface of the PEDOT: PSS, as shown in the SEM image in Figure 6.6, may be another possible reason that helps to increase the lifetime of the devices, because the PMMA may inhibit water from passing from the PEDOT: PSS into the active layer.

6.3.4 C-AFM of binary and ternary blend films

AFM and C-AFM were used to explore how PMMA influences the morphology and conductivity of these films with aging. A comparison between as-deposited binary and ternary blend films is shown in Figure 6.12.

The addition of PMMA resulted in the formation of high spots on the film, as shown in Figure 6.12(c). The current map in Figure 6.12 (d) reveals that the electrical conductivity through these high spots is low, indicating that these regions are affected by the presence of PMMA, so that no current passes through this area, as illustrated in Figure 6.6. The domes that PMMA creates may have a beneficial effect on the lifetime. One possibility is that the PMMA might act as a 'gettering' agent for water in the film.

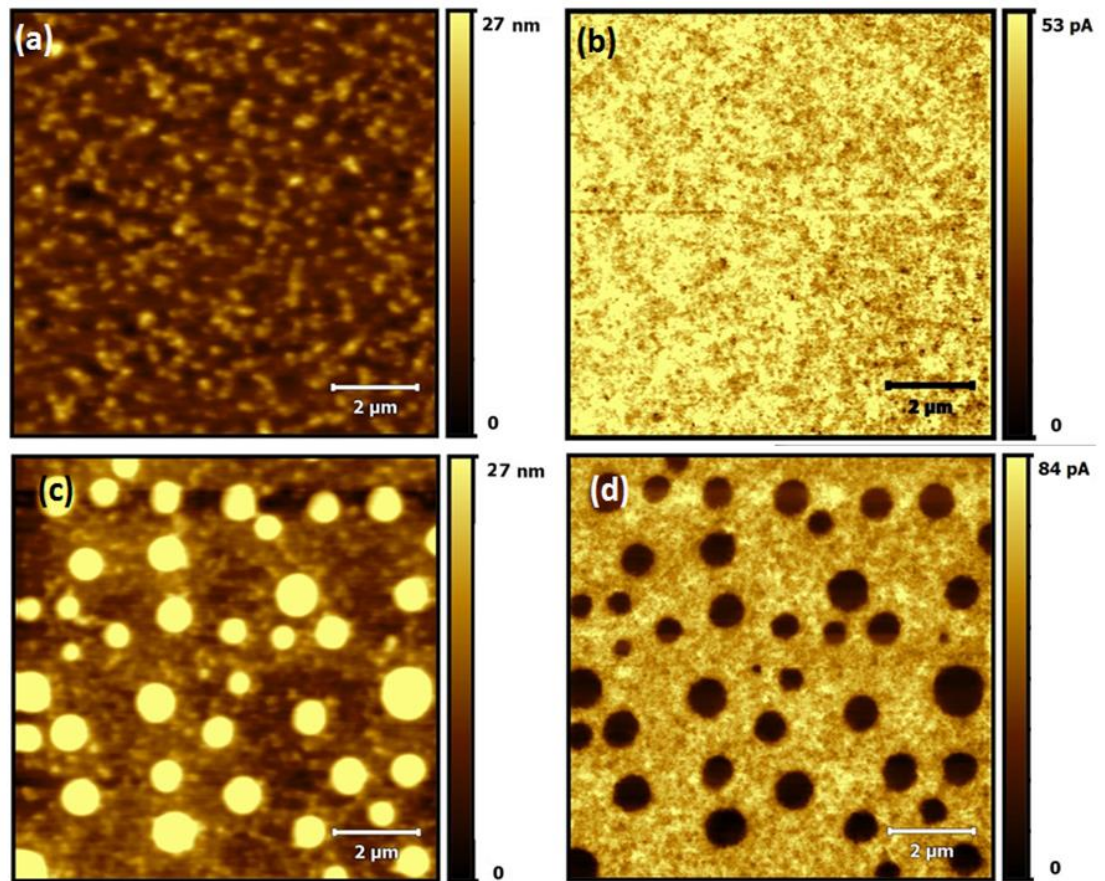


Figure 6.12. AFM topography images of (a) as-deposited (1:1) P3HT: PCBM film and (c) 86 wt%(50:50 P3HT: PCBM): 14 wt% PMMA film. (b & d) C-AFM images of the same areas, taken at 1 V bias.

Table 6.3 reveals that PMMA has a beneficial impact on lifetime for low RH, but that for higher RH (50% and above) the improvement in a lifetime is substantially reduced or absent. This is consistent with the suggestion that PMMA is acting as a gettering agent. The ability of PMMA to absorb water that would otherwise react with the active layer will necessarily be limited.

Returning to the C-AFM images of Figure 6.12, it is evident that the P3HT: PCBM rich regions in both the binary and ternary films show variations in current that would be expected due to local variations in conductivity [18], although P3HT fibrils were not observed. It is possible

that the conductivity in these regions may be related to hole conductivity through P3HT or P3HT-rich domains, since the work function of the conductive Au tip aligns with the highest occupied molecular orbital (HOMO), of P3HT [18]. Figure 6.13 compares C-AFM images for the binary and ternary blend films after storing them under 50% and 1% RH for 500 h.

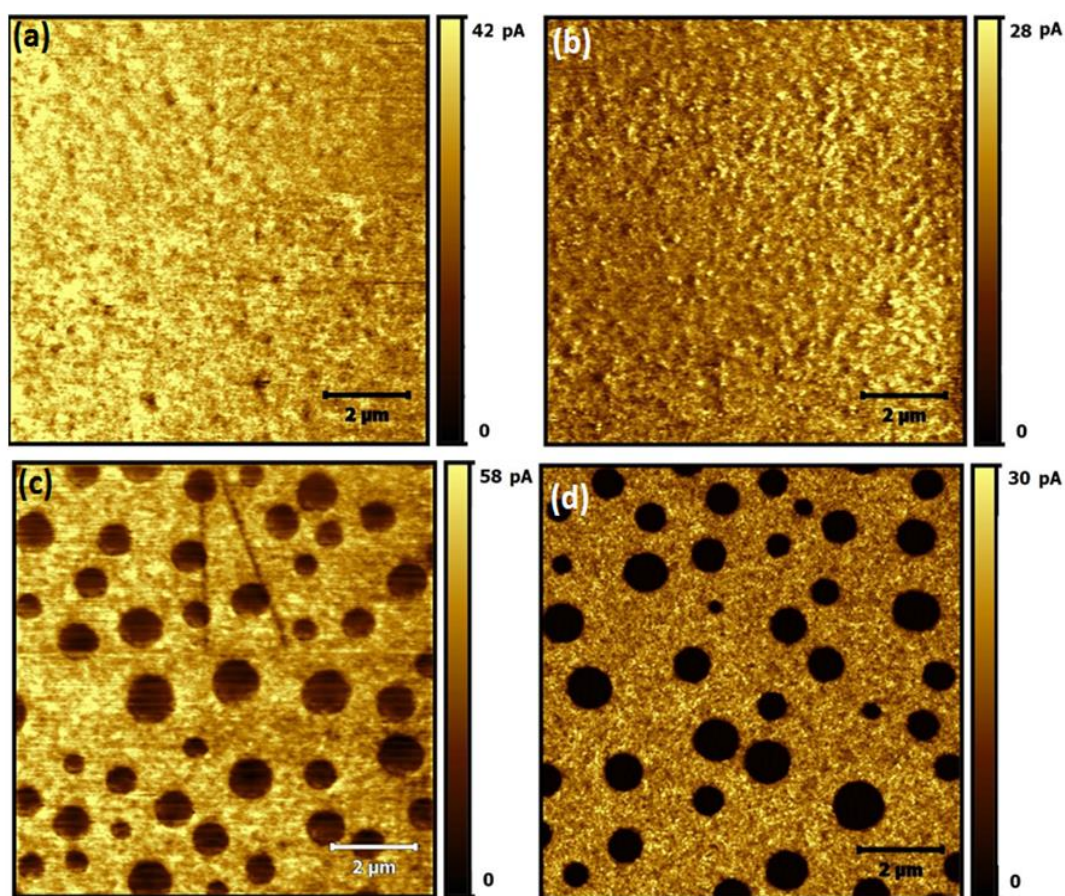


Figure 6.13. C-AFM images of aged P3HT: PCBM (a and b) and P3HT: PCBM: PMMA (c and d) films stored in 1% RH (a and c) and 50% RH (b and d). All images were taken at 1 V bias after 500 h.

The conductivity of the binary film was shown to be lower than that of the ternary film that had been stored under the same RH, although the difference in conductivity is larger at 1% RH than at 50%

RH. This result is consistent with the suggestion that PMMA is acting as a gettering agent for water. It seems that aging at higher RH saturates the PMMA, leading to a similar conductivity for ternary and binary films after aging. The binary and ternary devices aged for 500 h in 50% RH were significantly degraded and showed a PCE of almost zero, as shown in Figure 6.9. This might suggest that recombination mechanisms are additionally affected by the formation of traps.

To obtain further insight, the C-AFM images were analyzed statistically. The average current and the standard deviation were measured in seven different regions with an approximate area of ($1.7 \mu\text{m} \times 0.6 \mu\text{m}$) for each film, as shown in Table 6.6.

Table 6.6 The average values of current, standard deviation and the coefficient of variation calculated from different areas on the binary and ternary blend (between the low conductivity spots) films.

Humidity level (RH)	Device	Average current I (pA)	Standard deviation rms (pA)	Coefficient of variation (rms / I)
Fresh	Binary	47.2 ± 0.6	8.2 ± 0.3	0.2 ± 0.01
	Ternary	64.8 ± 0.7	7.5 ± 0.3	0.1 ± 0.01
Aged in 1% RH	Binary	33.2 ± 1	5.9 ± 0.3	0.2 ± 0.01
	Ternary	45.7 ± 1	7.3 ± 0.2	0.2 ± 0.003
Aged in 50% RH	Binary	12.6 ± 1	4.5 ± 0.4	0.3 ± 0.01
	Ternary	14.6 ± 0.2	3.0 ± 0.1	0.2 ± 0.003

In ternary blend films, the data were extracted from areas between the PMMA islands, which are expected to be P3HT: PCBM rich. Figure 6.14 illustrates histograms of the current for typical areas chosen

from both binary and ternary devices, as-deposited and after 500 h in low (1%) and high (50%) humidity.

As might be expected from Figure 6.13, each histogram shows that the conductivity has a roughly normal distribution, indicating the absence of aging-induced 'hot spots' or 'dead spots.' The initial current in the ternary devices was higher than that in the binary devices, as might be anticipated due to the improved initial performance of the ternary devices (Figure 6.9).

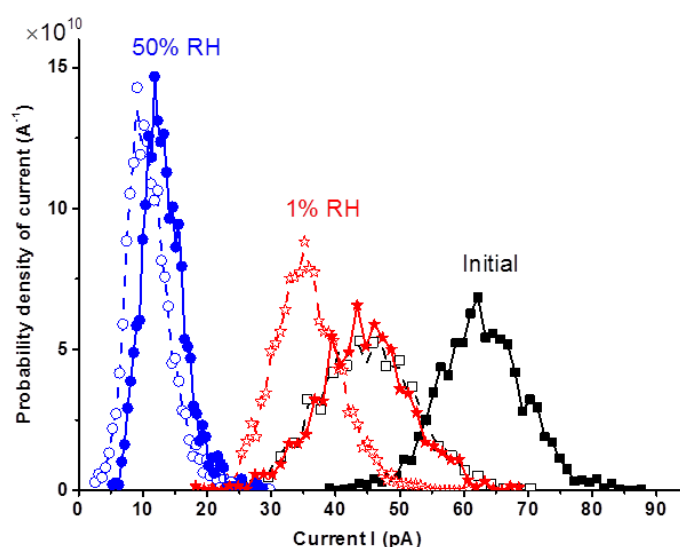


Figure 6.14. Histograms of the current probability distribution for P3HT: PCBM films (open symbols) and P3HT: PCBM: PMMA films (closed symbols) measured as-deposited and after storage for 500 h in 1% RH and 50% RH environments. The measurements were performed on typical small areas ($1.7 \mu\text{m} \times 0.6 \mu\text{m}$) of each device.

After aging for 500 h at 1% RH, the average current fell by $\approx 30\%$ for both devices. This contrasts with the OPV performance (Figure 6.9) which shows that ternary devices age less rapidly under 1% RH than binary devices. Again, this suggests that the electronic properties of the OPVs are degraded by aging, but that the reduction in PCE is due to more than changes in mobility caused by trap formation [21]. Traps may be attributed to structural features, such as defects associated with the polymer backbone [22], incomplete bonding forming vacancies [18], or chemical reactions with oxygen or other contaminants [15], [17], [21]. It has been suggested that structural defects in P3HT largely cause shallow traps [23], while chemical reactions between the active layer materials and water or oxygen lead to deeper traps [21]. It appears that the degradation in the conductivity shown in the C-AFM images of Figure 6.14 is only partly related to the degradation in PCE illustrated in Figure 6.9. The degradation in PCE is largely due to the formation of deep traps, which is partially arrested by the addition of PMMA. It is proposed that the deep traps lead to enhanced Shockley-Read-Hall (SRH) recombination [6] which in turn reduces PCE. This is consistent with the observed loss in performance being primarily via J_{sc} and FF. It is proposed that the degradation in conductivity observed in Figure 6.14 is instead principally due to the formation of shallow traps in the active layer, which is primarily of physical origin [1].

6.4 Conclusion

This chapter has shown that the addition of PMMA to P3HT: PCBM devices improve both the initial performance and the lifetime of OPVs.

Measurements of the electrical parameters demonstrated that PMMA improves the J_{sc} and the FF. UV-vis absorption revealed that PMMA does not cause a noticeable change in the crystallization of P3HT. Measurements at a variety of relative humidities suggest that the PMMA acts as a water getting agent. It is also shown that the lifetime improvement with PMMA reduces with increasing relative humidity, suggesting that the polymer can become saturated. SEM and AFM measurements revealed that the addition of PMMA results in a morphology containing PMMA-rich domes appearing underneath a layer rich in P3HT: PCBM. The rate, at which conductivity degrades, as measured by C-AFM in the dark, is similar in both binary and ternary devices. This suggests that multiple degradation mechanisms are at work and that PMMA only assists in extending the lifetime associated with some degradation pathways. It was proposed that the PCE of P3HT: PCBM devices is largely limited by reactions with water and that PMMA can slow down the process of degradation by the absorption of water. Our work demonstrates that an electrically inert, partially hygroscopic material can be blended with an OPV active layer to improve device lifetime. Although PMMA is used here, saturation of the polymer is observed, suggesting that different materials may extend lifetime still further.

6.5 References

- [1] F.-C. Wu, S.-W. Hsu, H.-L. Cheng, W.-Y. Chou, and F.-C. Tang, "Effects of soft insulating polymer doping on the photovoltaic properties of polymer–fullerene blend solar cells," *J. Phys. Chem. C*, vol. 117, no. 17, pp. 8691–8696, 2013.
- [2] T. A. Ferenczi, C. Müller, D. D. Bradley, P. Smith, J. Nelson, and N. Stingelin, "Organic semiconductor: insulator polymer ternary blends for photovoltaics," *Adv. Mater.*, vol. 23, no. 35, pp. 4093–4097, 2011.
- [3] T. Ameri, P. Khoram, J. Min, and C. Brabec, "Organic ternary solar cells: a review," *Adv. Mater.*, vol. 25, no. 31, pp. 4245–4266, 2013.
- [4] F. Goubard and G. Wantz, "Ternary blends for polymer bulk heterojunction solar cells," *Polym. Int.*, vol. 63, no. 8, pp. 1362–1367, 2014.
- [5] Y. Huang, W. Wen, S. Mukherjee, H. Ade, E. Kramer, and G. Bazan, "High-molecular-weight insulating polymers can improve the performance of molecular solar cells," *Adv. Mater.*, vol. 26, pp. 4168–4172, 2014.
- [6] M. Kuik, G.-J. Wetzelaer, H. Nicolai, N. I. Craciun, D. De Leeuw, and P. Blom, "25th Anniversary article: charge transport and recombination in polymer light-emitting diodes.," *Adv. Mater.*, vol. 26, no. 4, pp. 512–31, 2014.

- [7] J. Wang and B. Qi, "Fill factor in organic solar cells," *Phys. Chem. Chem. Phys.*, vol. 15, no. 23, pp. 8972–8982, 2013.
- [8] V. S. Balderrama, M. Estrada, P. L. Han, P. Granero, J. Pallarés, J. Ferré-Borrull, and L. F. Marsal, "Degradation of electrical properties of PTB1: PCBM solar cells under different environments," *Sol. Energy Mater. Sol. Cells*, vol. 125, pp. 155–163, 2014.
- [9] G. Horowitz, "Organic thin film transistors: from theory to real devices," *J. Mater. Res.*, vol. 19, no. 7, pp. 1946–1962, 2004.
- [10] M. Wang, F. Xie, J. Du, Q. Tang, S. Zheng, Q. Miao, J. Chen, N. Zhao, and J. B. Xu, "Degradation mechanism of organic solar cells with aluminum cathode," *Sol. Energy Mater. Sol. Cells*, vol. 95, no. 12, pp. 3303–3310, 2011.
- [11] V. M. Drakonakis, A. Savva, M. Kokonou, and S. A. Choulis, "Investigating electrodes degradation in organic photovoltaics through reverse engineering under accelerated humidity lifetime conditions," *Sol. Energy Mater. Sol. Cells*, vol. 130, pp. 544–550, 2014.
- [12] X. Han, X. Chen, and S. Holdcroft, "Nanostructured morphologies and topologies of pi-conjugated polymers from thermally reactive polymer blends," *Adv. Mater.*, vol. 19, no. 13, pp. 1697–1702, 2007.
- [13] A. D. Scaccabarozzi and N. Stingelin, "Semiconducting: insulating

polymer blends for optoelectronic applications-a review of recent advances," *J. Mater. Chem. A*, vol. 2, no. 28, pp. 10818–10824, 2014.

- [14] W.-F. Su, "Polymer size and polymer solutions," in *Principles of Polymer Design and Synthesis*, 1st ed., Springer-Verlag Berlin Heidelberg, 2013, p. 306.
- [15] K. Norrman, S. A. Gevorgyan, and F. C. Krebs, "Water-induced degradation of polymer solar cells studied by H₂ ¹⁸O labeling," *ACS Appl. Mater. Interfaces Appl. Mater. Interfaces*, vol. 1, no. 1, pp. 102–112, 2009.
- [16] E. Voroshazi, B. Verreet, A. Buri, R. Müller, D. Di Nuzzo, and P. Heremans, "Influence of cathode oxidation via the hole extraction layer in polymer: fullerene solar cells," *Org. Electron. physics, Mater. Appl.*, vol. 12, no. 5, pp. 736–744, 2011.
- [17] H. Nicolai, M. Kuik, G. Wetzelaer, B. De Boer, C. Campbell, C. Risko, J. Brédas, and P. Blom, "Unification of trap-limited electron transport in semiconducting polymers," *Nat. Mater.*, vol. 11, no. 10, pp. 882–887, 2012.
- [18] H. Cheng, W. Lin, and F. Wu, "Effects of solvents and vacancies on the electrical hysteresis characteristics in regioregular poly (3-hexylthiophene) organic thin-film transistors," *Appl. Phys. Lett.*, vol. 94, no. 22, p. 223302, 2009.

- [19] L. M. Do, E. M. Han, Y. Niidome, M. Fujihira, T. Kanno, S. Yoshida, A. Maeda, and A. J. Ikushima, "Observation of degradation processes of Al electrodes in organic electroluminescence devices by electroluminescence microscopy, atomic force microscopy, scanning electron microscopy, and Auger electron spectroscopy," *J. Appl. Phys.*, vol. 76, no. 9, pp. 5118–5121, 1994.
- [20] K. Kawano, R. Pacios, D. Poplavskyy, J. Nelson, D. D. C. Bradley, and J. R. Durrant, "Degradation of organic solar cells due to air exposure," *Sol. Energy Mater. Sol. Cells*, vol. 90, no. 20, pp. 3520–3530, 2006.
- [21] J. Schafferhans, Andreas Baumann, A. Wagenpfahl, C. Deibel, and D. Vladimir, "Oxygen doping of P3HT: PCBM blends: influence on trap states, charge carrier mobility and solar cell performance," *Org. Electron.*, pp. 1693–1700, 2010.
- [22] W. Graupner, G. Leditzky, G. Leising, and U. Scherf, "Shallow and deep traps in conjugated polymers of high intrachain order," *Phys. Rev. B*, vol. 54, no. 11, p. 7610, 1996.
- [23] J. Simon and J. Andre, *Molecular Semiconductors: Photoelectrical Properties and Solar Cells*. Berlin: Springer-Verlag Berlin Heidelberg, 2011.

CHAPTER 7

TERNARY OPVs USING OTHER INSULATING POLYMERS

7.1 Introduction

As discussed in Chapter 6, blending P3HT: PCBM with the insulating polymer PMMA led to an enhancement in the performance and lifetime of OPV devices. The improvement in device lifetime was attributed to the ability of PMMA to act as a gettering agent for water. This proposed hypothesis invites further investigation with other insulating polymers with greater or lesser hygroscopicity than PMMA. Examples of such materials are atactic polystyrene (a-PS) and polyethylene glycol (PEG). In this Chapter, 14 wt% of a-PS or PEG was blended with P3HT: PCBM to compare the impact of these polymers on the device lifetime.

7.2 The degradation of ternary devices incorporating a-PS

Multiple binary (P3HT: PCBM) and ternary devices (P3HT: PCBM: a-PS containing 14 wt% a-PS) were fabricated as described in section 4.3. They were distributed as follows: 12 binary devices were stored in 50% RH and another 12 devices stored in 1% RH. An equal number of ternary devices were also stored in 50% and 1% RH. Figure 7.1 shows the degradation in PCE of these devices over a 450 h time period.

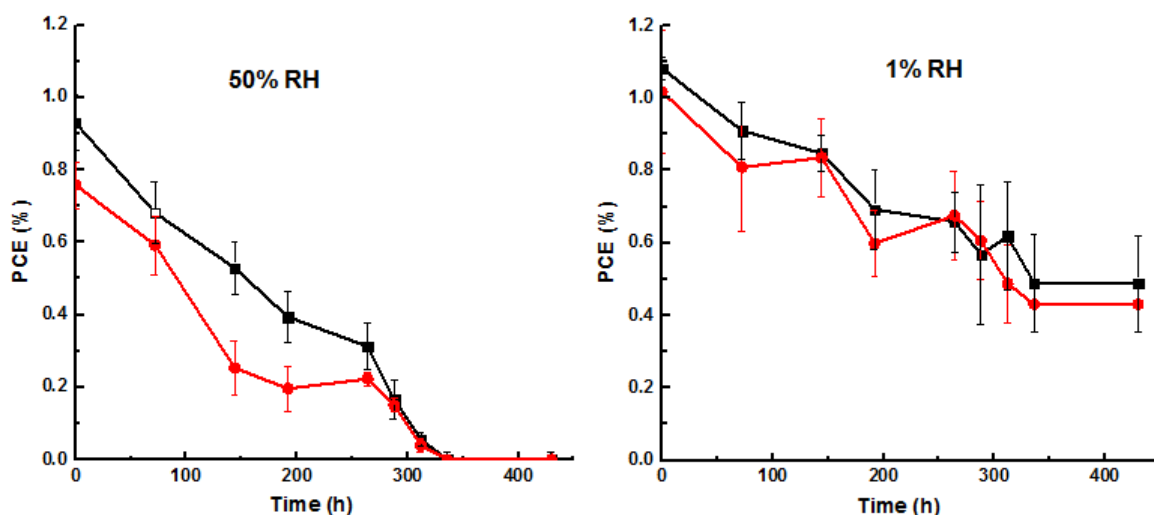


Figure 7.1. Power conversion efficiency as a function of time for binary (black squares) and ternary (red circles) devices containing 14 wt% a-PS stored in 50% and 1% RH.

The binary and ternary devices degraded at the same rate in both humidity levels. Both types of devices reached lifetime less than T_{20} at approximately 280 h storage in 50% RH, while having degraded by $\sim 50\%$ after more than 300 h when stored in 1% RH. This result indicates that the addition of a-PS to P3HT:PCBM has no significant effect on the device lifetime. One possible reason that the degradation is not slowed down in the ternary devices is the weak ability of a-PS to absorb water (maximum absorption of water by weight $\sim 0.01\text{-}0.07\%$) [1]. This result supports the suggestion that PMMA improves lifetime of OPVs by acting as a gettering agent for water.

The ternary devices incorporating a-PS polymer have lower initial performance than their binary counterparts. The differences in the initial performance of the devices for 1% and 50% RH may be due to a slight variation in the thickness of the active layer, or to a change in the quality of deposition of the top Al electrode, in turn caused by variations in the

thermal evaporation process. The poor initial performance of the ternary devices was due to a reduction in J_{sc} compared to equivalent binary devices, as shown in Figure 7.2.

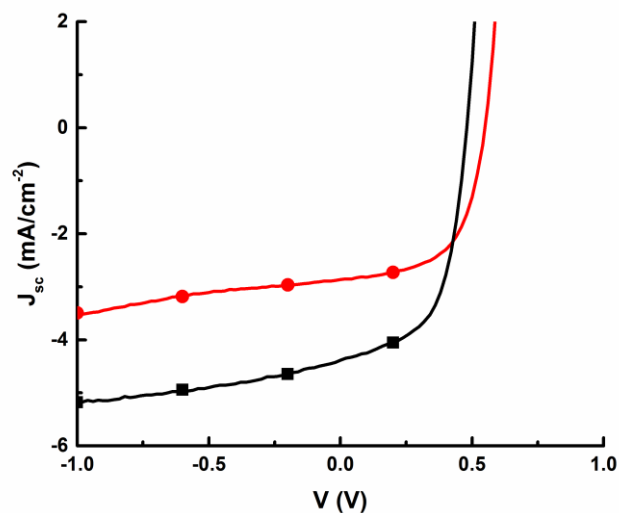


Figure 7.2. J-V curves under illumination for typical binary P3HT: PCBM (1:1) (black squares) and 86 wt% (50: 50 P3HT: PCBM): 14 wt% a-PS (red circles) OPVs.

This finding is consistent with other studies which reported that the amorphous nature of a-PS might cause a negative effect on electronic percolation within the semiconductor component, leading to a reduction in J_{sc} [2], [3].

7.3 The degradation of ternary devices incorporating PEG

Based on previous results with PS, which has low hygroscopicity, it was expected that adding PEG might increase the lifetime of the devices more than PMMA due to its high ability to absorb water. To test this hypothesis, binary and ternary devices (containing 14 wt% PEG) were

fabricated as described in section 4.3. 12 binary (P3HT: PCBM) and 12 ternary (P3HT: PCBM: PEG) devices were fabricated together and stored in 50% RH, and the same number of binary and ternary devices were stored in 1% RH.

The lifetime measurements plotted in Figure 7.3 show that the ternary devices degraded slightly more slowly, when the RH was 50%. The degradation in ternary devices was slower than that in binary devices stored under 50% RH. However, both types of device had the same rate of degradation when stored in a 1% RH environment during the duration of lifetime test (200 h). The increased ability of PEG to absorb water may be the reason for the slow degradation at 50% RH, although these devices started with poorer initial power conversion efficiency.

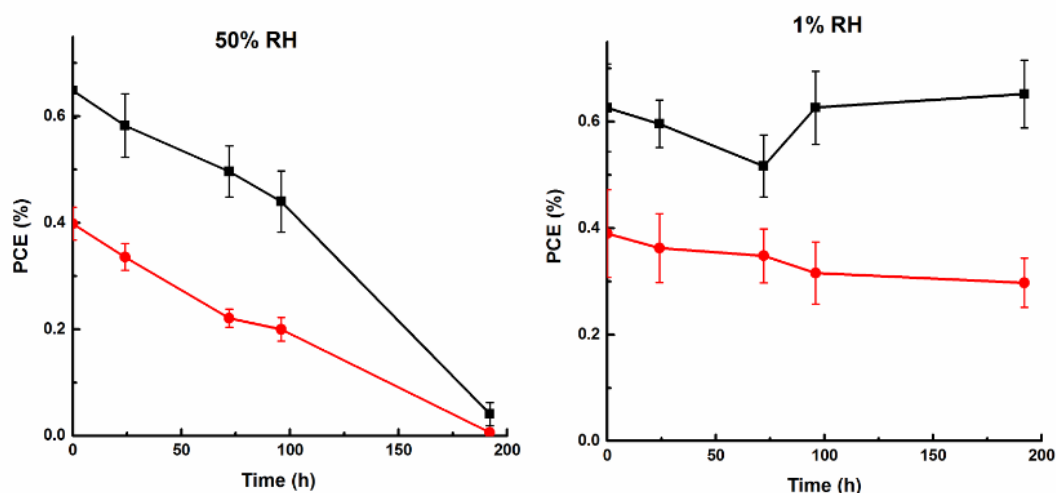


Figure 7.3. Power conversion efficiency as a function of time for binary devices (black squares), and ternary devices containing 14 wt% PEG (red circles) stored at (a) 50% RH and (b) 1% RH.

7.4 Comparison between ternary devices incorporating PMMA, PS, and PEG

When comparing ternary devices containing 14 wt% of PMMA, PS, and PEG with data obtained for binary devices in 50% RH, a variation in lifetime (T_{20}) among binary devices was observed, as shown in Table 7.1

Table 7.1 The T_{20} lifetime and PCE for devices including different insulating polymers stored in 50% RH.

Ternary/Binary or control devices	T_{20} (h)	Initial PCE (%)
P3HT: PCBM: PS / P3HT: PCBM	288 /288	$0.78 \pm 0.10/0.93 \pm 0.08$
P3HT: PCBM: PMMA /P3HT: PCBM	168/120	$1.1 \pm 0.20/0.80 \pm 0.10$
P3HT: PCBM: PEG/ P3HT: PCBM	>150 / ≥ 150	$0.40 \pm 0.03/0.64 \pm 0.05$

The variation in lifetime and performance between binary (P3HT: PCBM) devices indicates that many factors may affect the lifetime of OPVs. These factors, such as fabrication process and atmospheric conditions, are difficult to control. These factors were discussed in section 5.3. It was found that it was difficult to reproduce exactly the same conditions during the fabrication and measurement processes.

However, the general trend is clear from all the experiments. It is evident that the degradation of binary devices is the same as that in devices containing PS but reduced in devices incorporating PMMA and PEG. When comparing the results from PEG devices with those from PMMA devices, the devices containing PMMA degraded faster than those incorporating PEG when they were stored under 50 % RH, indicating that

polymers with higher hygroscopicity may play an important role in the enhancement of the lifetime of OPVs.

7.5 The performance of ternary devices incorporating PEG

Table 7.2 compares the performance of as-deposited binary and ternary devices stored in 50% RH.

Table 7.2 The average performance of as-deposited binary and ternary devices.

Device	V_{oc} (V)	J_{sc} (mA/cm ²)	FF (%)	PCE (%)
Binary	0.41 ± 0.01	3.1 ± 0.20	50 ± 01	0.64 ± 0.05
Ternary	0.39 ± 0.01	2.7 ± 0.10	36 ± 02	0.40 ± 0.03

A noticeable decrease was observed in the performance of ternary devices compared to binary devices. The major factor causing this reduction in the initial PCE was the FF. Ternary devices had a lower FF (36% ± 2%) than binary devices (50% ± 1%). The low FF in these devices may be attributed to a high series resistance (R_s). This series resistance was calculated from the dark J-V curves of the binary and ternary devices as discussed in section 6.2.1. It was found that ternary devices had a higher R_s than binary devices (8.35 $\Omega \cdot \text{cm}^2$ vs. 3.93 $\Omega \cdot \text{cm}^2$). The series resistance arises from the bulk resistance of the active layer and the electrode resistances [4]. It was proposed that the origin of this high series resistance in ternary devices containing PEG molecules might be the ITO/PEDOT: PSS electrode, as explained in the next sections.

7.6 UV-vis absorption spectra of P3HT: PCBM: PEG

Figure 7.4 shows the absorption spectra of the binary (P3HT: PCBM) and ternary (P3HT: PCBM: PEG) films after spin-casting. The light absorption of the ternary film was lower than that of its binary counterpart. This may be attributed to differences in the film thicknesses. It was found that the film thickness of the binary film was ~ 115 nm while the thickness of the ternary film was ~ 90 nm. Furthermore, the absorption at 603 nm was pronounced in both films, indicating that the addition of PEG did not disrupt the crystallinity of the P3HT.

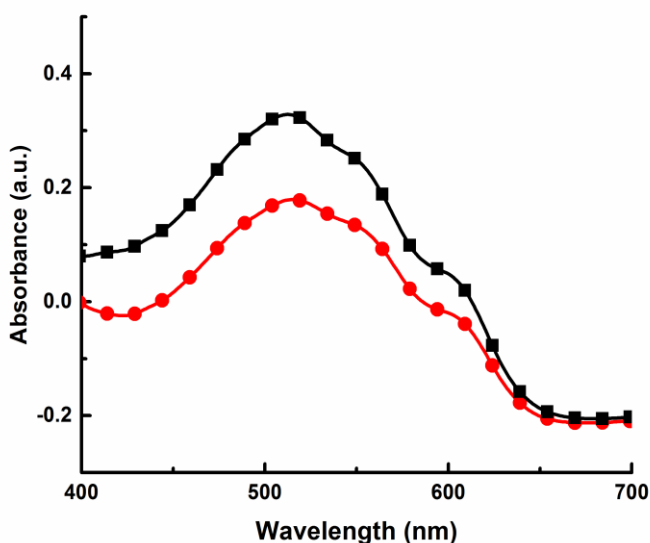


Figure 7.4. The absorption spectra of P3HT: PCBM (black squares), and P3HT: PCBM: PEG films (red circles).

7.7 Morphology of ternary blend film incorporating PEG

The surface film morphology was studied using AFM in order to establish why the addition of PEG did not improve the performance of

P3HT: PCBM devices. Figure 7.5 shows that the addition of PEG into the blend caused the formation of irregularly shaped pits in the active layer with raised edges.

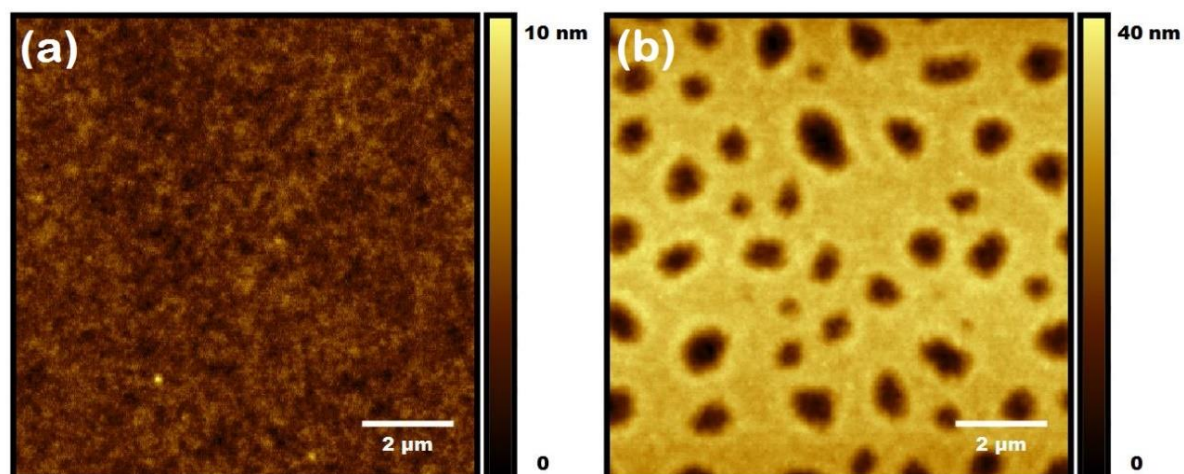


Figure 7.5. AFM topography images of (a) P3HT: PCBM, (b) P3HT: PCBM: PEG films.

The rms roughness of the film was increased by the addition of PEG molecules, from 0.847 nm to 6.75 nm for binary and ternary blend films, respectively. The surface profiles shown in Figure 7.6 indicate that the depth of the holes varies, ranging from ~ 12 nm to 35 nm. It appears that the depth of the holes is less than the thickness of the active layer, i.e., 89 ± 9 nm.

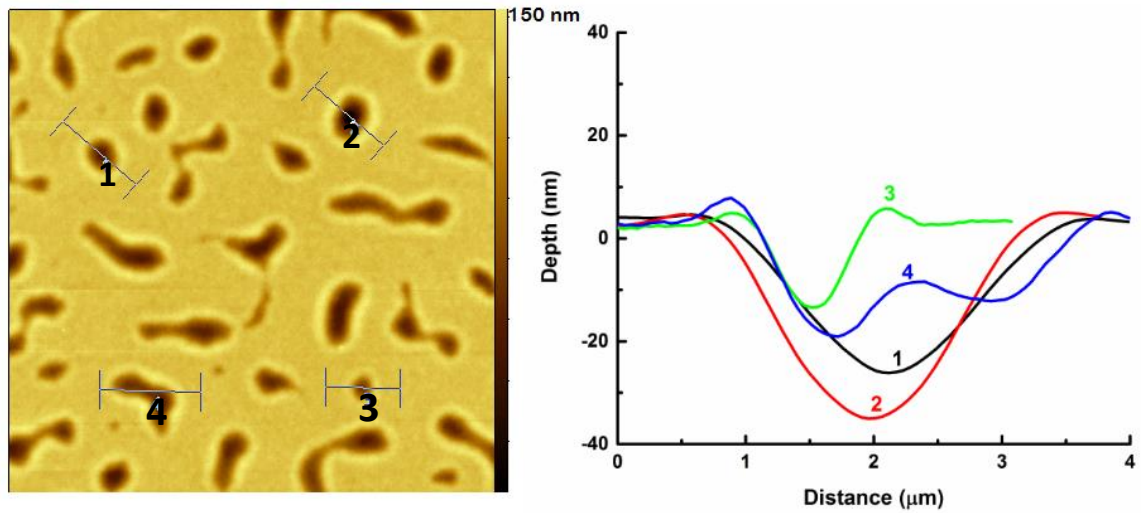


Figure 7.6. Surface profiles (right) showing the depths of holes chosen from the AFM image (left). The numbers on the profiles indicate the positions of line scans on the topography image.

C-AFM was performed on the ternary film in order to better understand the variation in the conductivity of the film caused by the holes. The current map in Figure 7.7(b) shows that the conductivity was higher around the edges of the holes. This may relate to the raised area around the edges of the holes, as illustrated in Figure 7.7 ((c) and (d)).

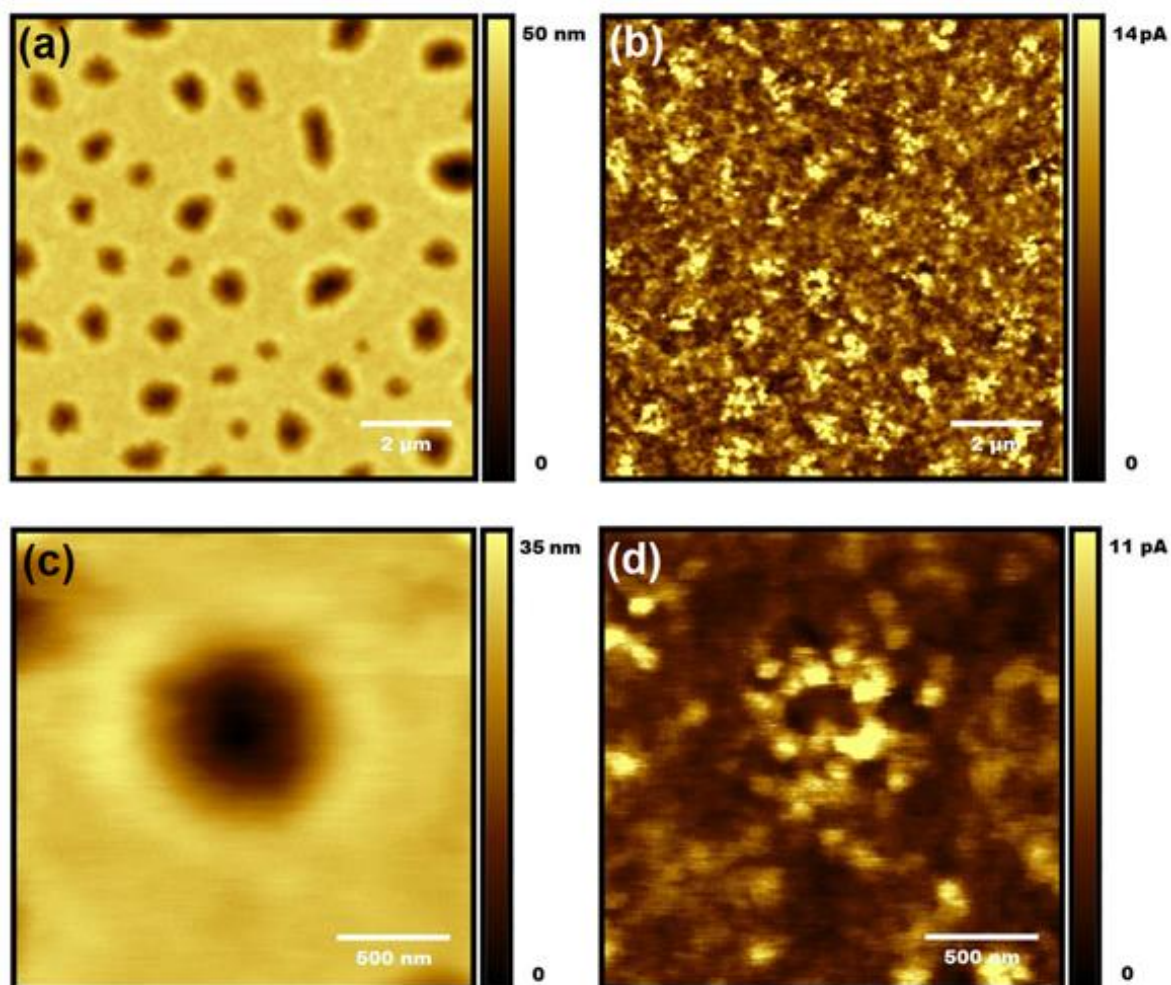


Figure 7.7. AFM images for a P3HT:PCBM:PEG film, (a) topography, (b) the C-AFM current map of the area in (a), (c) topography image of one hole, and (d) the current map of the area in (c), (scan area $2 \times 2 \mu\text{m}$) taken at 1 V.

However, it was not clear if the holes are conductive or not due to the shape of the tip. The U-shape of the contact tip may prevent the measurement of the current flowing through the bottom of the holes. This is because the tip may not reach the bottom or the sidewalls of the holes, just measuring the current at the edges. The scanning of the tip across the holes does not only affect the measurement of current but also the measurement of the hole depth. The depth of the holes obtained from the surface profile in Figure 7.6, may not represent the actual depth but a maximum depth measurement that tip can achieve, which is

smaller than the true depth. This is illustrated in Figure 7.8.

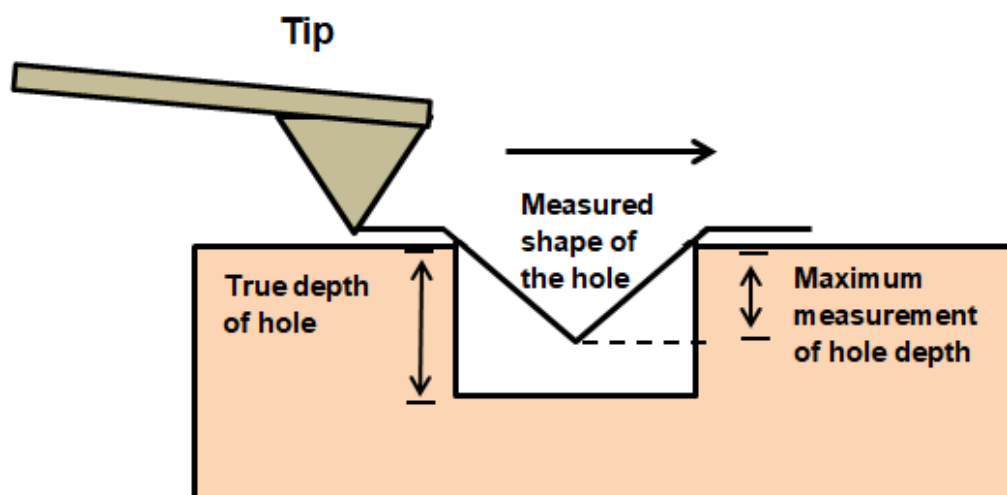


Figure 7. 8. Schematic diagram showing how the profile of the tip can affect the AFM image of features.

In the case of C-AFM, the end contact tip has a semicircular shape which could prevent it from reaching the bottom and the sidewalls of the hole, leading to measuring the current at the edge but not the current flowing through the bottom of the pit. It appears that the tip scans through the edges and this does not give enough information about the conductivity in the hole.

Further investigations were undertaken to ascertain where the PEG molecules migrate to. One possible way to investigate beyond the active layer is to scratch the active layer (with tweezers). The surface of PEDOT: PSS layer was imaged by using AFM tapping mode. Figure 7.9 compares AFM images for the PEDOT: PSS layer from binary and ternary blend devices.

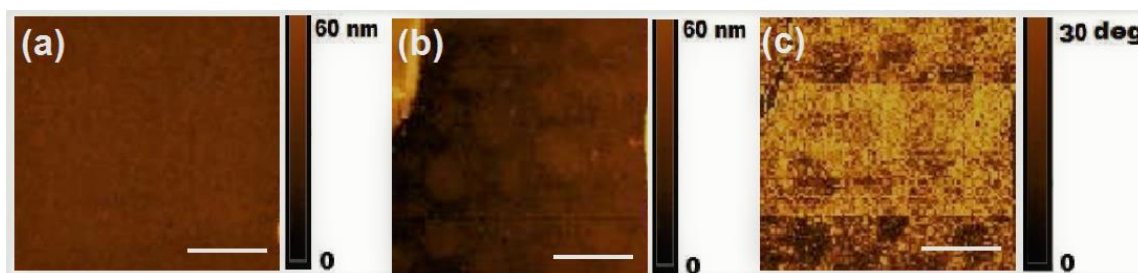


Figure 7.9. AFM images of the PEDOT: PSS layers from devices containing (a) a binary blend film and (b) a ternary blend film. (c) Phase image recorded at the same time as (b). The size of the scale bar is 10 μm .

It was noted that circular, raised features appeared in the topography image of the PEDOT: PSS layer from the ternary device. These features are faintly visible in Figure 7.9 (b), while they were not present in the image from the binary device. These features were also observed in the phase image of the PEDOT: PSS layer from the ternary blend device (Figure 7.9 (c)). The contrast in the AFM phase images is often related to material differences, which might indicate that the raised features are related to the presence of PEG. Multilayer devices, discussed in section 7.9.2 also show these raised features.

7.8 Proposed morphology of ternary blend films incorporating PEG

AFM was used to find a line profile between holes in the active layer and islands observed in the PEDOT: PSS layer. The line profile of holes in the active layer and spots in PEDOT: PSS layer is shown in Figure 7.10.

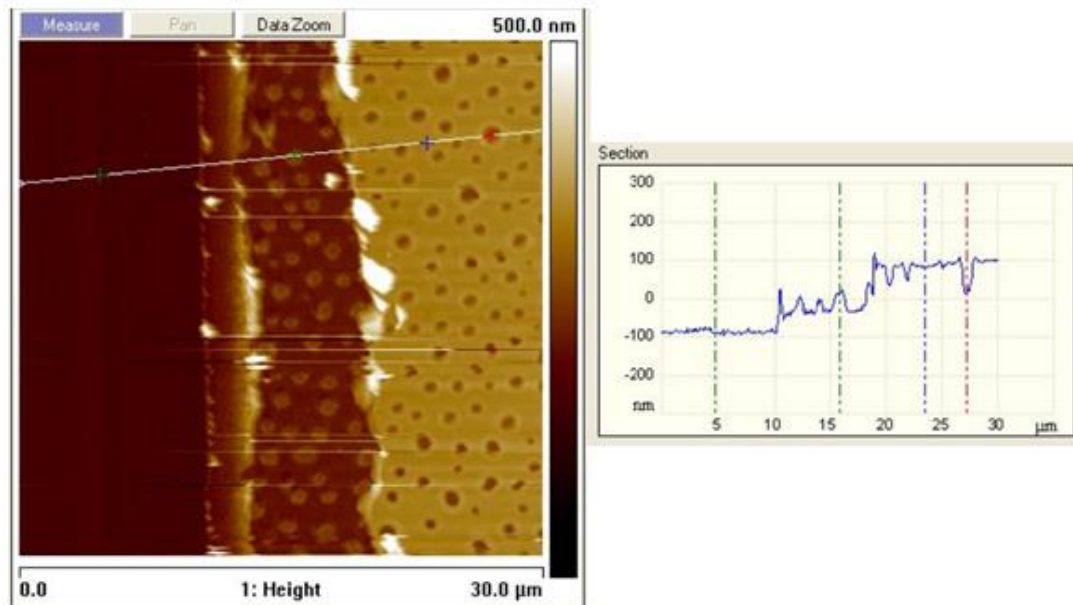


Figure 7.10. A typical line profile (right) taken from an AFM image (left) showing a hole in the active layer and a raised spot on the PEDOT: PSS layer. (x-axis is the distance (μm), and y-axis is the height (nm)).

It was found that the bottom of the holes in the active layer lay at approximately the same height as the top of the raised spots on the surface of the PEDOT: PSS layer, as shown in Figure 7.10. It is possible that during spin coating, PEG molecules accumulate at the PEDOT: PSS surface and form islands underneath the active layer. It was suggested that PEG may form a blend and interact with PEDOT: PSS, leading to increase the device resistance and lower the PCE. A schematic diagram illustrating this proposed morphology is shown in Figure 7.11.

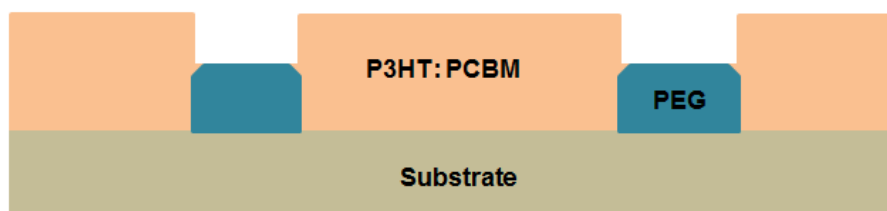


Figure 7.11. Schematic structure of the ternary film morphology.

Here, the PEG regions will lead to reduce current flow. Some PEG molecules may disperse in the active layer (P3HT: PCBM) and might disrupt the interpenetration network in the film. Hence, the overall current will be modified, resulting in a reduced FF and J_{sc} (Table 7.2) and changes in the shape of the J-V curve. Typical J-V curves for as-deposited binary and ternary devices are shown in Figure 7.12. It appears that the J-V curve of the ternary device is deformed due to the presence of holes in the active layer.

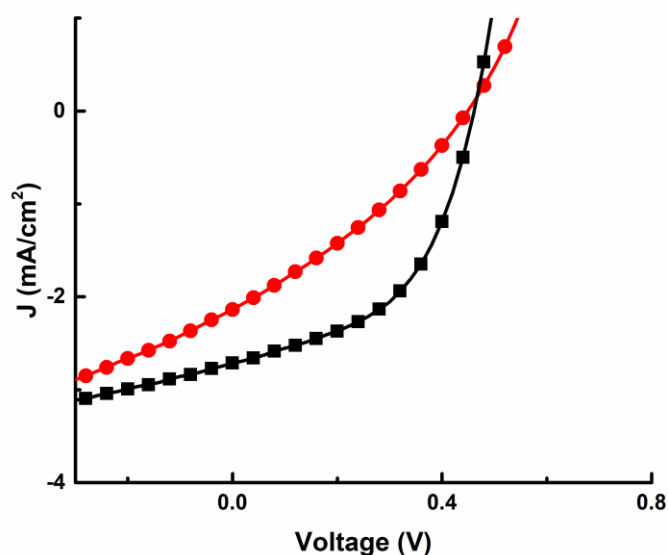


Figure 7.12. Typical J-V curves, under illumination, taken directly after spin-casting for binary devices (black squares) and ternary devices (red circles)

7.9 Degradation of Multilayer devices

There are thought to be two possible reasons for the presence of holes in the active layer of P3HT: PCBM: PEG; the interaction of PEG molecules with the substrate, and the compatibility of the solvent. The

difference in the solubility of the polymers may be the cause of the phase separation.

To investigate the effect of the substrate on the morphology of a ternary blend film containing PEG, a P3HT:PCBM binary layer was interposed between the PEDOT:PSS layer and the ternary layer. Four sets of devices were fabricated with the following structures: a binary blend film (P3HT:PCBM) with thickness of ~ 100 - 120 nm; a ternary blend film (P3HT:PCBM:PEG) with a film thickness of ~ 80 - 100 nm; a bilayer structure: an unannealed binary blend film (~ 100 - 120 nm) beneath a ternary blend film (~ 80 - 100 nm), denoted as "multilayer-unannealed film" to represent the bilayer having an unannealed first layer; a bilayer structure: an annealed binary blend film (~ 100 - 120 nm) beneath a ternary blend film (~ 80 - 100 nm), denoted as "multilayer-annealed film,". The post-annealing process was applied to all the devices. Each set contained four devices, which were all stored in 50% RH. The structures of all four device types are illustrated schematically in Figure 7.13.

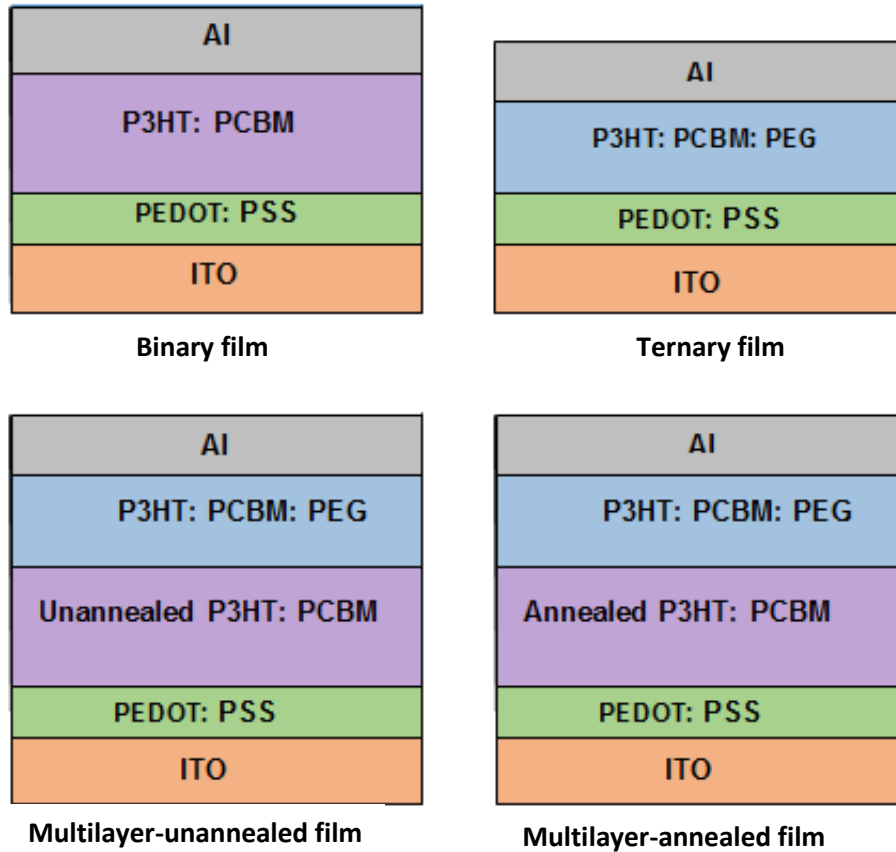


Figure 7.13. The structures of the four sets of devices.

7.9.1 Lifetime measurements

The performance of these devices was monitored for 200 h, and the results are shown in Figure 7.14. The binary devices exhibited longer lifetimes than the other three sets. A PCE was measurable for more than 190 h in the binary devices, while the other three sets had lifetimes (T_{20}) of less than 100 h.

All three sets had lower initial PCE than standard binary devices. The ternary devices showed the poorest performance while that of the devices with multilayer-unannealed film was higher than the annealed devices.

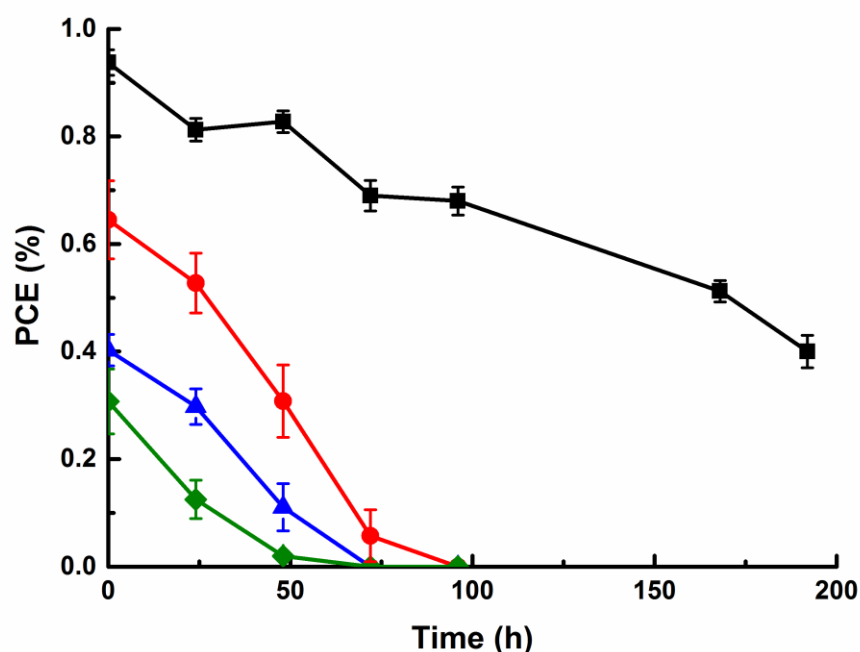


Figure 7.14. PCE as a function of time for devices containing: a binary film (black squares), a ternary film (green diamonds), multilayer-unannealed film (red circles), and multilayer- annealed film (blue triangles).

Although this result indicates that casting the ternary solution on the binary film is better than using one layer of a ternary blend film, the lifetime was not enhanced by this technique.

Moreover, this result showed that ternary devices degraded faster than binary devices, which conflicts with the result shown in Figure 7.3. This contradiction may be related to the variation that may occur in the devices. As discussed before in section 5.3, it was not possible to reproduce exact fabrication and ambient environment conditions. Furthermore, the lifetime measurement in this experiment was taken from an average of four devices or one substrate, which may be poor due to variability, whereas the results in Figure 7.3 represented the average of 12 devices.

7.9.2 Film morphology of multilayer devices

The morphology of multilayer- unannealed and multilayer-annealed films was studied using AFM, and typical images are shown in Figure 7.15. Holes are still present in both films, but with a more regular, circular shape.

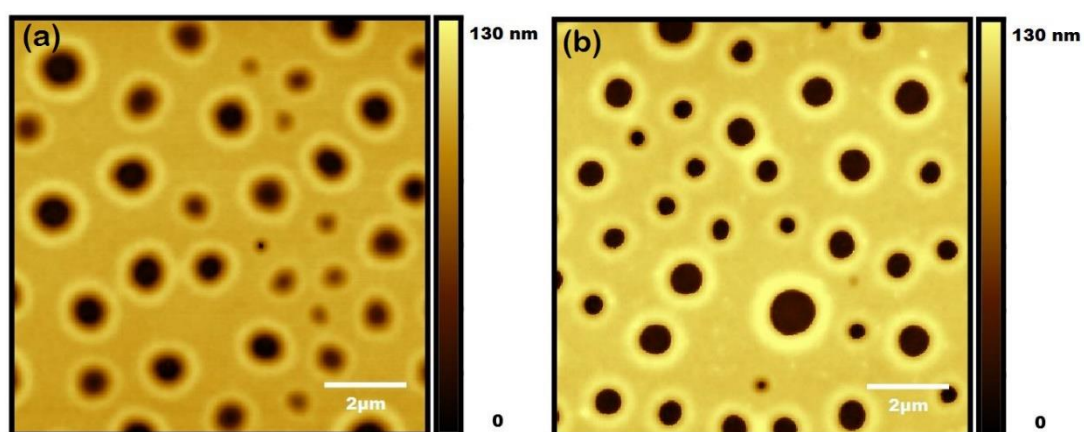


Figure 7.15. AFM topography of (a) multilayer-unannealed film (set 3), and (b) multilayer-annealed film (set 4).

This result shows that annealing had no effect on the holes in multilayer devices. However, it seems that the nature of the substrate had an impact on the shape of the holes. The presence of annealed and unannealed binary blend underlayers led to the formation of more circular holes in the ternary layer when compared with the case of a PEDOT: PSS underlayer (Figure 7.5). This suggests that the high surface energy of the P3HT: PCBM layer may affect the way that the PEG molecules distribute on the substrate. More importantly, when both films were scratched to allow investigation of the PEDOT: PSS active layer interface, circular features were clearly present, as shown in Figure 7.16.

This is similar to the result obtained from the ternary film that is provided in Figure 7.9, suggesting that PEG migrates to the PEDOT: PSS surface.

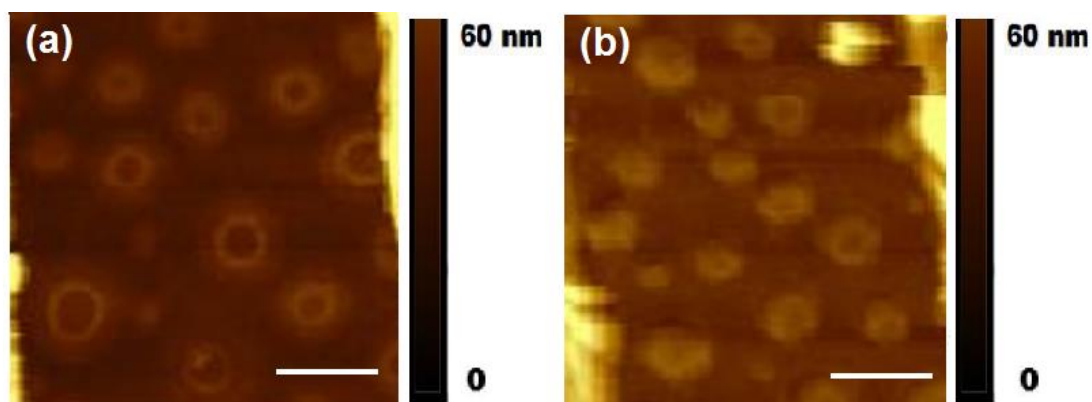


Figure 7.16. AFM images of the PEDOT: PSS layer in (a) multilayer-unannealed film, (b) multilayer-annealed film.

7.10 Degradation of ternary devices using nitrobenzene as a solvent for PEG

The relative solubility of the polymers is another possible reason for holes in the active layer of ternary devices containing PEG and in turn causes low performance. However, the solubility of PEG in DCB is higher than that of P3HT and PCBM; therefore, the P3HT: PCBM layer should solidify before the PEG. Because of this, the PEG molecules would tend to migrate to the top of the active polymer film. This behavior was observed by Chen et al. [5], who found that PEG molecules segregated on the surface of P3HT: PCBM. However, in this study, the opposite behavior is observed. One possible reason for this may be attributed to the high molecular weight of the PEG polymer used in this work ($M_w=108 \text{ kg mol}^{-1}$ vs. $M_w=0.2 \text{ kg mol}^{-1}$ [5]). Therefore, another way to prevent the migration of the PEG molecules into the PEDOT: PSS layer might be to

reduce the solubility of PEG by replacing DCB with nitrobenzene (NB) as the solvent for PEG.

Two sets of eight devices were prepared as described in section 4.6. The first set included devices based on a binary blend film of P3HT:PCBM. The second set was composed of devices based on a ternary blend film containing PEG, which was dissolved in NB instead of DCB before mixing with the P3HT:PCBM solution. All of the devices were stored in 50% RH and lifetime measurements were undertaken over the course of 200 h.

7.10.1 Lifetime measurements

Figure 7.17 reveals that the devices containing PEG from NB solvent have poor initial performance and undergo rapid degradation when compared to binary devices.

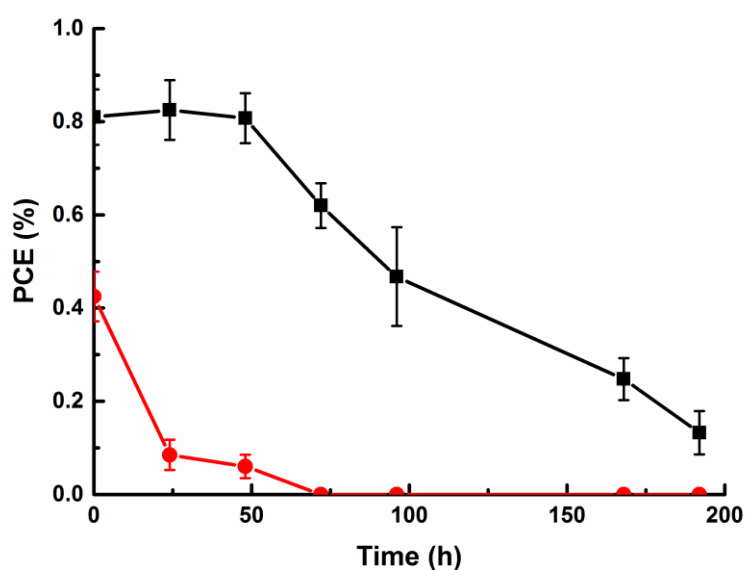


Figure 7.17. The PCE as a function of time for devices based on P3HT:PCBM binary blend film (black squares), and P3HT:PCBM:PEG ternary blend film using mixed solvent (PEG dissolved in NB) (red circles).

7.10.2 Film morphology

An AFM topography image of the morphology of a ternary blend film where NB was used as the solvent for PEG is shown in Figure 7.18 (b). No holes were observed in this case, indicating that the addition of NB to the ternary mixture has prevented their formation. Although the NB appears to help to eliminate the migration of PEG onto the surface of the PEDOT: PSS layer, the resultant morphology does not enhance the performance nor the lifetime of the devices. It appears that the PEG molecules are embedded in the P3HT: PCBM matrix. These may disrupt the P3HT: PCBM network and lower the efficiency of charge transport, causing a significant drop in the device performance. This finding indicates that the PEG molecules formed an unfavorable morphology in all cases, leading to poor performance.

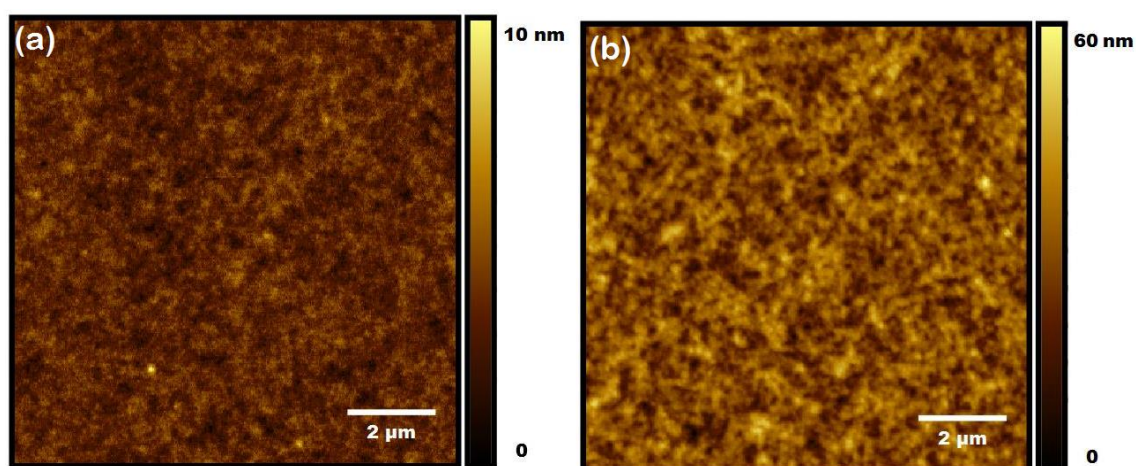


Figure 7.18. AFM topography images of (a) P3HT: PCBM film, (b) P3HT: PCBM: PEG film, spin-coated from mixed solvent.

7.11 Conclusion

This chapter has demonstrated that using an insulating polymer that is less hygroscopic than PMMA does not enhance the lifetime of OPV devices. It was found that binary and ternary devices (containing a-PS molecules) degraded at the same rate in high and low humidity environments. Although PEG polymer slows down the degradation of OPV devices in high and low humidity environments, the device performance was worse. It was inferred that PEG induces an unfavorable morphology, leading to an increase in the series resistance and reduction in the FF, resulting in poor power conversion efficiency. Overall, the addition of PEG molecules worked as a gettering agent but did not produce a significant enhancement in the lifetime of OPVs devices based on P3HT: PCBM.

7.12 References

- [1] "The universal selection source: plastics & elastomers," *SpecialChem*, 2017. [Online]. Available: <https://www.specialchem.com/about-specialchem>. [Accessed: 27-Mar-2017].
- [2] T. A. Ferenczi, C. Müller, D. D. Bradley, P. Smith, J. Nelson, and N. Stingelin, "Organic semiconductor: insulator polymer ternary blends for photovoltaics," *Adv. Mater.*, vol. 23, no. 35, pp. 4093–4097, 2011.
- [3] A. T. Williams, P. Farrar, A. J. Gallant, D. Atkinson, and C. Groves, "Characterisation of charge conduction networks in poly(3-hexylthiophene)/polystyrene blends using noise spectroscopy," *J. Mater. Chem. C*, vol. 2, no. 9, p. 1742, 2014.
- [4] J. Wang and B. Qi, "Fill factor in organic solar cells," *Phys. Chem. Chem. Phys*, vol. 15, no. 23, pp. 8972–8982, 2013.
- [5] F. Chen and S. Chien, "Nanoscale functional interlayers formed through spontaneous vertical phase separation in polymer photovoltaic devices," *J. Mater. Chem.*, vol. 19, pp. 6865–6869, 2009.

CHAPTER 8

PRELIMINARY INVESTIGATION IN THE HOLE TRANSPORT IN BINARY AND TERNARY DEVICES

8.1 Introduction

The charge carrier mobility is a basic parameter that affects the performance of OPVs [1]. Free carriers are generated in the active layer by the dissociation of excitons at the donor/acceptor interface [2]. These carriers can be transported, via hopping, between localized states in the conjugated polymer segments [1]. The transport mechanism can be interrupted by the presence of electronic traps, which enhance the recombination process [3], leading to a reduced carrier mobility. It has been shown that the trap density increases with time, due to the diffusion of water and oxygen into the active layer [4] [5].

In chapter 6, it was demonstrated that the blending of PMMA with P3HT: PCBM slowed down the degradation and increased the lifetime of OPV devices. It was suggested that PMMA might absorb the water from the active layer leading to lower the rate of formation of traps in the active layer and to a reduced carrier recombination rate. Using the space charge limited current (SCLC) model in binary and ternary devices may give an indication of how water and oxygen might interrupt the charge transport. The SCLC model also can provide an idea of how fast the carriers can travel through the active layer by measuring their mobility.

The SCLC technique uses electron-or hole-only devices so that the current associated with only one type of charge carrier (electrons or holes) can be measured. In this chapter, hole only devices were fabricated, and their J-V curves were analyzed with the aim of understanding the behavior of hole transport with time. The hole mobility was also measured in binary and ternary devices containing 14 wt% PMMA.

8.2 Space charge limited current in hole-only devices

In hole-only devices, the electrodes offer a low barrier for hole injection, and the electrons are not injected. By applying forward bias, the free carrier concentration can be increased due to the injected carriers. When the current is dominated by injected charge, the current voltage characteristic becomes quadratic, this is known as space charge limited current (SCLC).

In the absence of traps, SCLC is characterized by the Mott-Gurney equation [6]:

$$J = \frac{9}{8} \mu \epsilon_0 \epsilon_r \frac{V_{\text{int}}^2}{d^3} \quad (8-1)$$

Where ϵ_0 is the permittivity of the vacuum, ϵ_r is the dielectric constant of the material (assumed to be ~ 3) [6], μ is the carrier mobility, d is the thickness of the active layer, and V_{int} is the internal voltage drop across the active layer. The internal voltage can be obtained by subtraction of the built-in voltage (V_{bi}) from the applied voltage (V_{app}),

$V_{\text{int}}=V_{\text{app}}-V_{\text{bi}}$, where V_{bi} arises from the difference in work function of the electrode materials ($V_{\text{bi}} = \phi_{\text{PEDOT: PSS}} - \phi_{\text{Au}}$), which, in this case, is equal to 0.1.

This equation assumes injection of a single-carrier type, no traps, and the carrier mobility being field independent, which simplifies the SCLC model. This model is commonly used for organic semiconductors [7], even though it neglects energetic disorder. The Mott-Gurney equation is used to estimate the mobility by fitting the equation to the experimental data of the dark J-V curve.

Of course, a real device may be expected to display different behavior than the Mott-Gurney idealization. Figure 8.1 shows a more complete theoretical expectation of the current-voltage curve on a log-log scale measured for one-carrier current. It comprises three distinct regions, denoted I, II, III corresponding to ohmic, trap-filling, and trap-filled regions, respectively [7].

In region I, where the voltage is low, the density of injected carriers is lower than the density of intrinsic charge carriers, so that the current follows Ohm's law ($J \propto V$) [8]. As the voltage is increased (region II), the number of injected carriers increases and trap occupancy increases. This region is known as the trap-filling region.

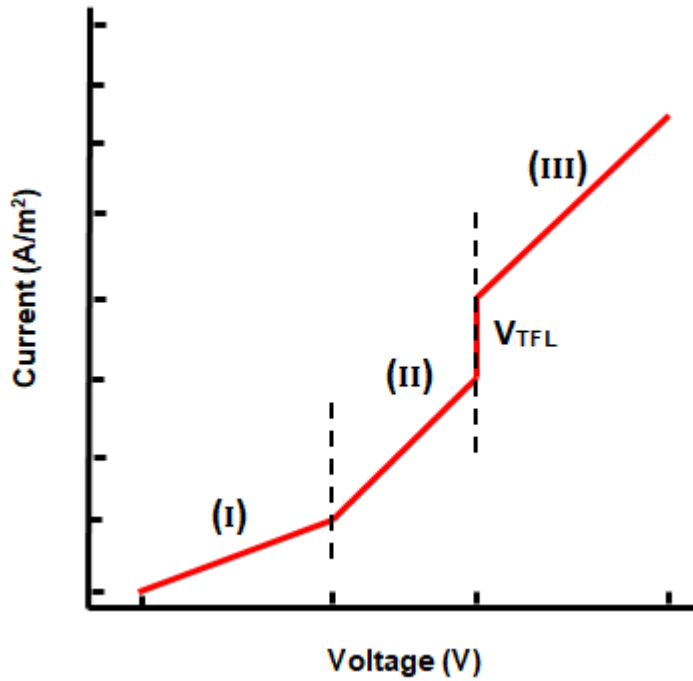


Figure 8.1. Log-log plot of J-V curve for expected single-carrier space charge limited current in a device containing a single set of traps, showing Ohmic (I), trap-filling (II), and trap free SCLC (III) regions.

As the voltage increases further, more holes are injected and fill the trapping sites until reaching the trap-filled limit (V_{TFL}) where the entire population of traps is filled. When this happens, the current undergoes a step change, and then switches to a quadratic behavior, indicating that all subsequent injected charge carriers are free charge carriers and this represents region III. This regime corresponds to trap free space charge limited current where $J \propto V^2$ and can be described by the Mott-Gurney equation.

8.3 Conductivity in binary and ternary devices at different humidity levels

To investigate the behavior of hole current in OPVs, two sets of 12 hole-only devices, of binary and ternary blend films comprising 14 wt% PMMA, were fabricated as illustrated in section 4.3. However, the top electrode (Al) was replaced by Au (100 nm) to suppress electron injection into the PCBM. The devices were stored in 1% and 50% RH and measured as-deposited and after different aging times. Figure 8.2 shows typical dark J-V curves for hole-only devices stored in high and low humidity levels, after aging for 0 h and 360 h.

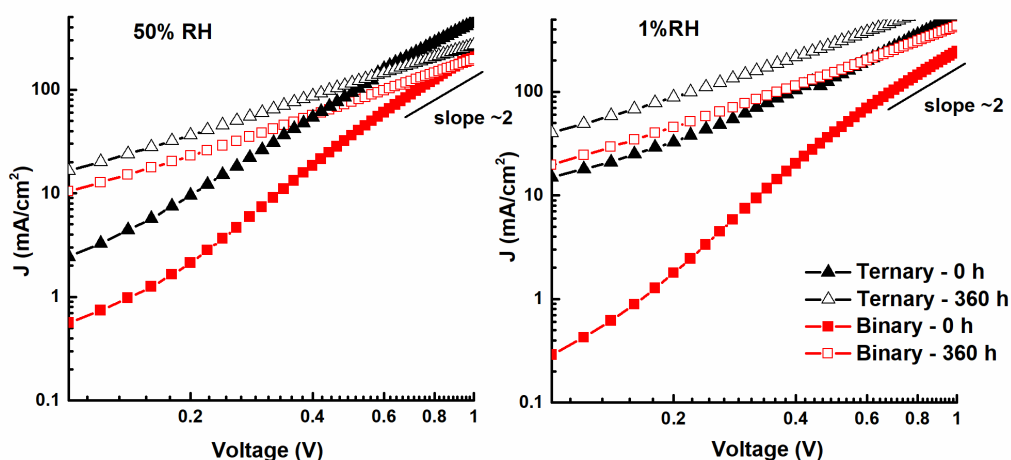


Figure 8.2. Dark J-V curve on log-log scales for the hole-only binary device (red squares) and ternary device (black triangles), stored in 50% RH and 1% RH as-deposited (closed symbols) and after 360 h (open symbols).

It was found that the initial hole current in ternary devices was higher than that in binary devices, which indicates that the addition of PMMA improves the conductivity of SCLC devices. The difference in the initial performance for devices stored in 1% and 50% RH may be related

to a variation in the quality of the thermally evaporated Au anodes. Similar degradation behavior was observed for devices stored in 1% and 50% RH. The hole current increased in both types of devices after they had been aged for 360 h. This result was unexpected because the degradation mechanisms caused a reduction in the photovoltaic performance. Both devices stored in 50% RH exhibited very poor performance after 360 h. The SCLC region was observed with slope ~ 2 for as deposited devices. However, the hole mobility was not calculated because the film thickness of these devices was not measured.

The observed increase in the current with time was surprising, suggesting that further experiments were needed to address the reason for this behavior. First, the experiment was repeated to make sure that process variations during fabrication were not responsible. 12 hole-only binary and other 12 of ternary devices were fabricated using the same processing conditions as the previous experiment. The devices were stored in a 1% RH environment. The tendency of the current to increase with time was similar to the results of the first experiment, as shown in Figure 8.3. This suggests that the observed increase in hole current with time is a repeatable phenomenon.

The measurements in this experiment continued for more than 1300 h. The results show that as the aging time increases, the current increases until reaching an aging time where the current saturates. The binary and ternary devices reached a saturation point at an approximately same time, as shown in Figure 8.3.

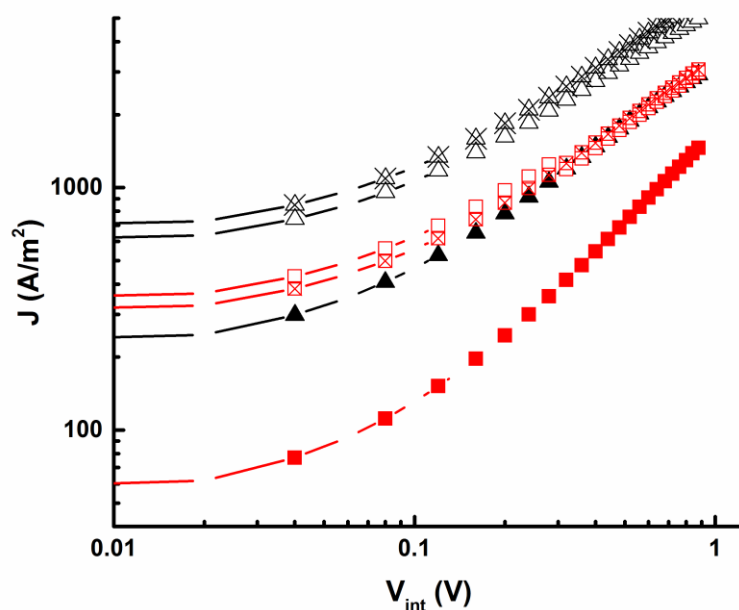


Figure 8.3. Typical dark J-V curves on log-log scales for hole-only binary device (red squares) and ternary device (black triangles), stored in 1% RH at different aging times, as-deposited (closed symbols), after 336 h (crossed symbols), and after 1392 h (open symbols).

However, when the film thicknesses of the devices in Figure 8.3 were measured by AFM, it was found that the binary and ternary active layers were 100 nm and 80 nm, respectively. Therefore, further devices were prepared, with the thickness of the active layer fixed. The results are presented in the next section.

8.4 Hole mobility in binary and ternary devices with fixed film thickness

Here, four sets of four hole-only devices with structure of ITO/PEDOT: PSS/active layer/Au were fabricated. Four different active layers were used as follows: Pure P3HT (22 mg/ml), blend film of P3HT:

PCBM (60 mg/ml), blend film of P3HT: PMMA (60 mg/ml), and ternary blend film of P3HT: PCBM: PMMA (80 mg/ml) at spin speeds of 1500, 1000-1200, 1000, and 950-980 rpm respectively, hence the film thicknesses were adjusted to be in the range 93 ± 2 nm. All the devices were measured and stored in 50% RH for 216 h. The J-V curves for typical devices from each of the four sets are shown in Figure 8.4.

When controlling the film thickness, it was found that the current is less in ternary devices than the binary counterpart. As before, the increase in hole current with time is observed. This result indicates that the behavior of hole transport with time is similar to the previous results shown in Figure 8.2 and Figure 8.3. However, the origin of enhanced hole current with time is not clear. Since the device lifetime is usually related to carrier transport, one would expect that as the degradation increases, the mobility would decrease.

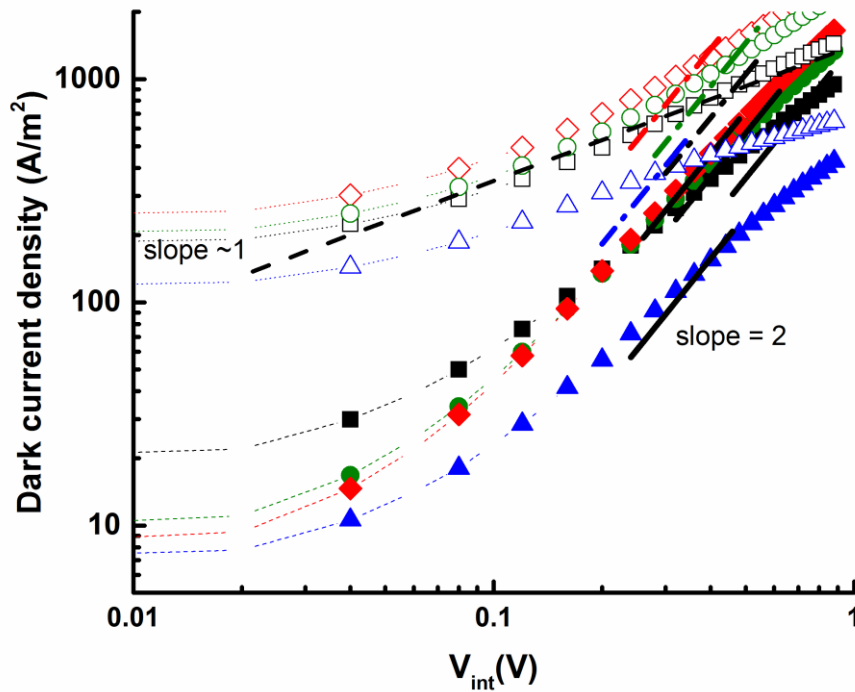


Figure 8.4. Dark current density as a function of internal voltage for typical hole-only devices based on P3HT (closed red diamonds), P3HT: PMMA (closed green circles), P3HT: PCBM (closed black squares), and P3HT: PCBM: PMMA (closed blue triangles). The open symbols relate to devices aged for 216 h. The solid lines represent the fits according to the equation of the SCLC (equation 8-1). The dotted line indicates that the slope of the plot for aged devices is ~ 1 , which represents the Ohmic region.

Assuming trap free transport, the Mott-Gurney equation was applied for the four set of devices shown in Figure 8.4. It was found that the experimental data of the four as-deposited devices were fitted with Mott-Gurney equation at V_{int} ranges between ~ 0.3 V to 0.6 V. It was assumed that these fitting regimes correspond to trap free space charge limited current [8]. The initial hole mobility of as-deposited typical devices was calculated and shown in Table 8.1.

Table 8.1 The initial hole mobility values in devices based on active layers with various compositions.

Blend film of hole-only device	μ_h (cm ² /Vs)
Pure P3HT	7.74×10^{-4}
P3HT: PMMA	6.17×10^{-4}
P3HT: PCBM	3.87×10^{-4}
P3HT: PCBM: PMMA	2.65×10^{-4}

The results of hole mobility of pure P3HT and P3HT: PCBM devices were in agreement with other studies which found that the hole mobility was in the order of 10^{-3} - 10^{-4} cm²/Vs by using SCLC and time-of-flight (TOF) techniques [1][9].

In the case of aged devices, the equation was invalid and was not fitted to the data. All the aged devices exhibited linear relationship over the entire voltage range, corresponding to ohmic region as shown in Figure 8.4. Hence it was not possible to calculate mobility from the Mott-Gurney equation as the J-V curve was not quadratic. An increase in current with time was observed in all the experiments. Two possible reasons for enhanced hole current with time were proposed: the diffusion of metal contact or the ambient environment.

8.5 The effect of the environment

The presence of water and oxygen in ambient environment might cause an increase in doping with time. By returning to the results in

Section 8.3, it was found that hole current increased with time when devices were stored in both high and low humidity (Figure 8.2). To discover whether the humidity has an effect on the hole current, the four sets of devices that had been stored in 50% RH for 216 h (section 8.4) were transferred to a low humidity environment ($\sim 1\%$ RH) and stored there for a further 336 h. It was expected that if the humidity was reduced to a very low level, the hole current might be reversed, i.e., reduced slightly. However, the data show the opposite effect, as illustrated in Figure 8.5.

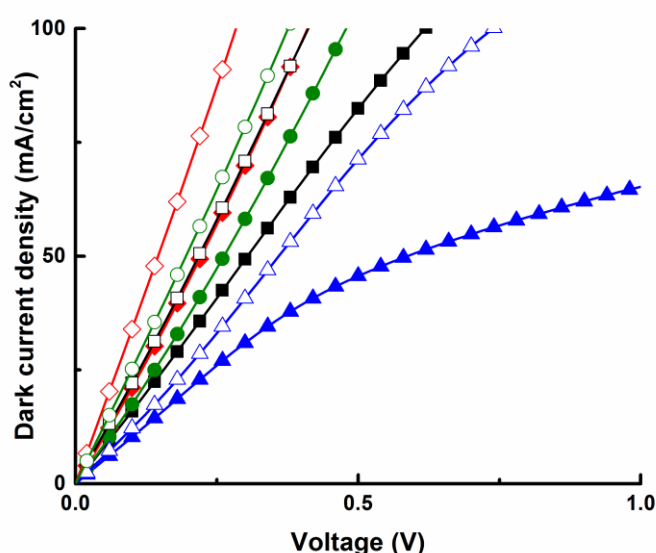


Figure 8.5. J-V curves of aged hole-only devices after storage in 50% RH for 216 h. Devices based on P3HT (closed red diamonds), P3HT: PMMA (closed green circles), P3HT: PCBM (closed black squares), and P3HT: PCBM: PMMA (closed blue triangles). The open symbols relate to aged devices after storage in 1% RH for 336 h.

This indication that the history of the device is important as well as current ambient atmosphere, suggesting some irreversible change is happening in the device. However, there is another factor that should not

be excluded, which is the presence of oxygen. Storing the devices in different humidity levels does not prevent their exposure to oxygen. Doping by oxygen may be one possible reason for the increase in the current with time. Ionized dopants may increase in population as the device is aged [10].

This doping in aged devices might decrease the resistance and/or lead to the formation of deep traps [11], which is an important parameter that Mott and Gurney neglected in their equation. Figure 8.6 shows the dark current in log-linear scale for the four sets of devices. It was found that the series resistance decreased with increasing time which might result from doping by oxygen.

However, from literature, it is not clear how oxygen can affect the carrier conductivity. For example, it was found that oxygen doping of P3HT increased the charge carrier concentration and also increased the density of deeper traps, which in turn reduced the carrier mobility [12][11]. Further, another study made by Abdou et al. [10] found that oxygen doping of P3HT created a charge complex ($\text{P3HT}^+ : \text{O}_2^-$) that increased the number of holes. It seems that oxygen doping changes the electronic properties of the P3HT and changes the concentration of holes, which here, overall, appears to increase hole current with time [11].

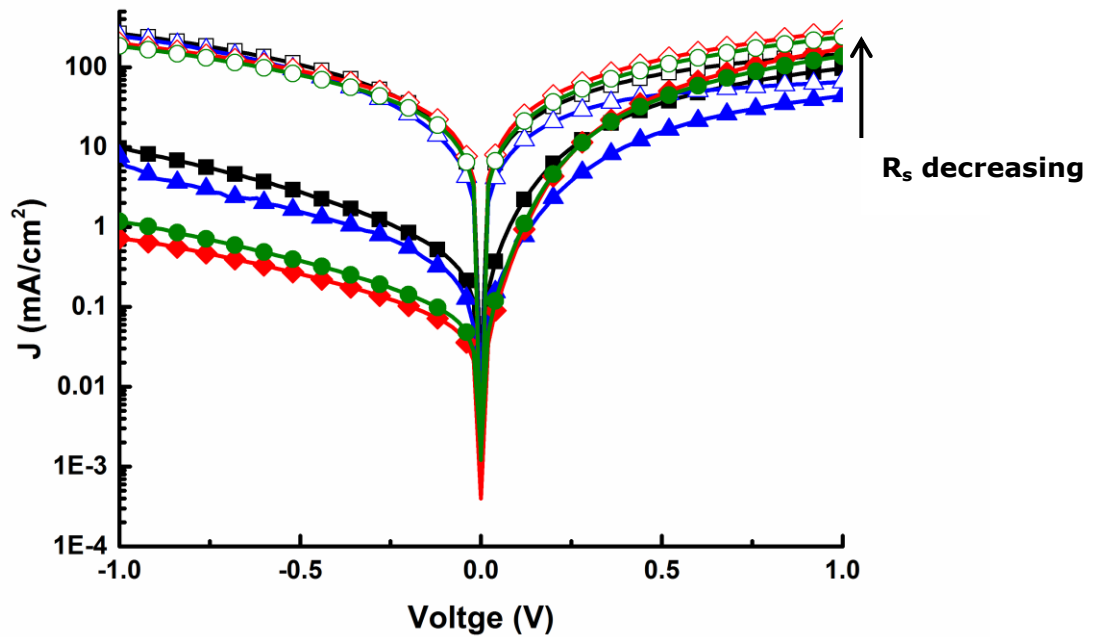


Figure 8.6. Dark J-V curves for typical hole-only devices based on P3HT (closed red diamonds), P3HT: PMMA (closed green circles), P3HT: PCBM (closed black squares), and P3HT: PCBM: PMMA (closed blue triangles) as-deposited. The open symbols relate to devices aged for 216 h in a 50% RH environment.

8.6 The effect of the metal contact on the hole current

The other possible reason for increase in hole current was suggested to be the metal contact, since Au may diffuse into the active layer, leading to an increase in device conductivity with time.

To test this assumption, SEM was used on hole only devices. Figure 8.7 shows a cross section of a P3HT: PCBM device.

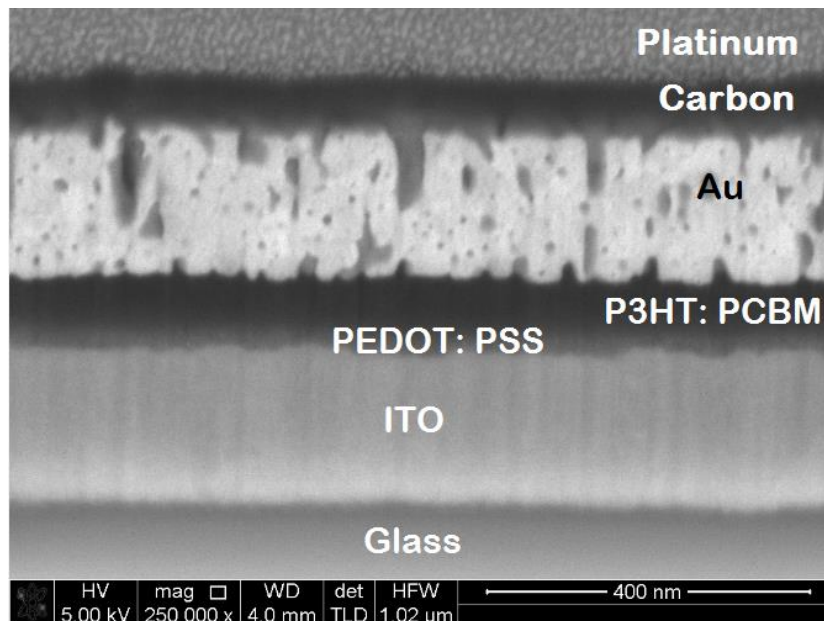


Figure 8.7. SEM cross-sectional view of a P3HT: PCBM device with an Au top contact.

It was observed that the gold film had a porous structure, which was possibly formed during deposition [13]. As the temperature increased during the thermal evaporation, the rate of deposition on the surface of active layer increased and may not have formed a uniform layer. It seems that the growth mode of the gold particles on the surface of the active layer is an island-type growth mode where particles grow vertically, producing a porous structure [13]. Importantly, it was observed that gold had not diffused into the active layer during aging, meaning that the diffusion of Au was not the reason for the strange behavior of the hole current. However, the porous nature of the gold layer may allow water and oxygen to penetrate the device, leading to the increase in the hole current, as discussed in the previous section.

8.6 Conclusion

This chapter shows that the hole current in hole only devices increased with time, up to a saturation value. As the degradation time increased, the trap free SCLC region cannot be observed within the range of voltages investigated. Only Ohmic regions were present for all the aged devices. Therefore, it was not possible to evaluate the mobility values.

It was concluded that the diffusion of the gold contact was not responsible for the observed change in the current with time. The reason for increasing the hole current with time was not clear after different investigations had been made. One possible suggestion to explain the increase in current was the diffusion of oxygen or water into the active layer. The formation of a charge transfer complex with P3HT polymer was predicted to be largely responsible for the generation of charge carriers in the devices.

8.7 References

- [1] F. Laquai, D. Andrienko, R. Mauer, and P. Blom, "Charge carrier transport and photogeneration in P3HT: PCBM photovoltaic blends," *Macromol. Rapid Commun.*, vol. 36, pp. 1001–1025, 2015.
- [2] X. Yang, J. Loos, S. Veenstra, W. Verhees, M. Wienk, J. M. Kroon, M. Michels, and R. Janssen, "Nanoscale morphology of high-performance polymer solar cells," *Nano Lett.*, vol. 5, no. 4, pp. 579–583, 2005.
- [3] G. Horowitz, "Organic thin film transistors: from theory to real devices," *J. Mater. Res.*, vol. 19, no. 7, pp. 1946–1962, 2004.
- [4] M. O. Reese, A. M. Nardes, B. L. Rupert, R. E. Larsen, D. C. Olson, M. T. Lloyd, S. E. Shaheen, D. S. Ginley, G. Rumbles, and N. Kopidakis, "Photoinduced degradation of polymer and polymer-fullerene active layers: experiment and theory," *Adv. Funct. Mater.*, vol. 20, no. 20, pp. 3476–3483, Oct. 2010.
- [5] R. Bauld, L. M. Fleury, M. Van Walsh, and G. Fanchini, "Correlation between density of paramagnetic centers and photovoltaic degradation in polythiophene-fullerene bulk heterojunction solar cells," *Appl. Phys. Lett.*, vol. 101, no. 10, pp. 1–5, 2012.
- [6] Z. B. Wang, M. G. Helander, M. T. Greiner, J. Qiu, and Z. H. Lu, "Carrier mobility of organic semiconductors based on current-voltage characteristics," *J. Appl. Phys.*, vol. 107, no. 3, 2010.

- [7] M. Syed, K. Iqbal, W. Younis, and K. Karimov, "Space charge-limited current model for polymers," in *Conducting Polymers*, F. Yilmaz, Ed. InTech, 2016, pp. 91–117.
- [8] A. Carbone, B. K. Kotowska, and D. Kotowski, "Space-charge-limited current fluctuations in organic semiconductors," *Phys. Rev. Lett.*, vol. 95, no. 23, pp. 2–5, 2005.
- [9] C. Proctor, M. Kuik, and T. Nguyen, "Charge carrier recombination in organic solar cells," *Prog. Polym. Sci.*, vol. 38, no. 12, pp. 1941–1960, 2013.
- [10] M. S. Abdou, F. Orfino, Y. Son, and S. Holdcroft, "Interaction of oxygen with conjugated polymers: charge transfer complex formation with poly(3-alkylthiophenes)," *J. Am. Chem. Soc.*, vol. 119, no. 19, pp. 4518–4524, 1997.
- [11] A. Guerrero, P. P. Boix, L. F. Marchesi, T. Ripolles-Sanchis, E. C. Pereira, and G. Garcia-Belmonte, "Oxygen doping-induced photogeneration loss in P3HT: PCBM solar cells," *Sol. Energy Mater. Sol. Cells*, vol. 100, pp. 185–191, 2012.
- [12] J. Schafferhans, A. Baumann, A. Wagenpfahl, C. Deibel, and D. Vladimir, "Oxygen doping of P3HT: PCBM blends: influence on trap states, charge carrier mobility and solar cell performance," *Org. Electron.*, vol. 11, pp. 1693–1700, 2010.
- [13] Z. H. Liu, N. M. D. Brown, and A. McKinley, "Evaluation of the

growth behaviour of gold film surfaces evaporation-deposited on mica under different conditions," *J. Phys. Condens. Matter*, vol. 9, no. 1, pp. 59–71, 1997.

CHAPTER 9

OPVs LAMINATED WITH INSULATING POLYMERS

9.1 Introduction

The rate of degradation in organic photovoltaic devices may be increased with the diffusion of water and oxygen through the electrodes [1]. These molecules can also diffuse through the PEDOT: PSS and through pinholes in and at the edges of the metal cathode [2][3]. Chapters 6 and 7 showed that the addition of an insulating polymer, such as PMMA or PEG (in some cases), to the P3HT: PCBM blend increased the lifetime of devices, due to their ability to work as a gettering agent for water. The presence of PMMA, at the PEDOT: PSS/active layer interface, was thought to absorb water. In contrast, adding PEG molecules to the active layer led to a significant drop in the efficiency of the device, due to the formation of an unfavorable morphology. Therefore, there are at least two possible obstacles that might prevent enhanced lifetime in these devices. First, the possibility of the diffusion of water and oxygen into the active layer through the cathode, as it has been reported in the literature. This leads to the formation of an insulating layer at the metal/active layer interface, which hinders charge extraction [1][2]. The second obstacle is the unfavorable morphology produced as a result of the addition of an insulating polymer such as PEG.

To overcome these drawbacks, a laminated architecture has been investigated. It was thought that laminating the device with an insulating

polymer may reduce the penetration of water and oxygen into the device and therefore minimize the formation of an insulating layer of metal oxide at the metal/active layer interface. Furthermore, the morphology of the active layer in devices manufactured using this approach is anticipated to be unaffected. This is very important in cases where the use of an insulating polymer, such as PEG, creates an unfavorable morphology, as shown in Chapter 7. This approach may lead to an improvement of both the device efficiency and lifetime. In this Chapter, devices laminated with layers of PMMA or PEG were compared. The effect of the lamination process on device performance and lifetime was studied.

9.2 The effect of the lamination process on device performance

Multiple devices, based on a blend of P3HT: PCBM, were fabricated as described in section 4.3. The lamination process is described in section 4.3.6., and the structure of laminated devices is illustrated schematically in Figure 9.1.

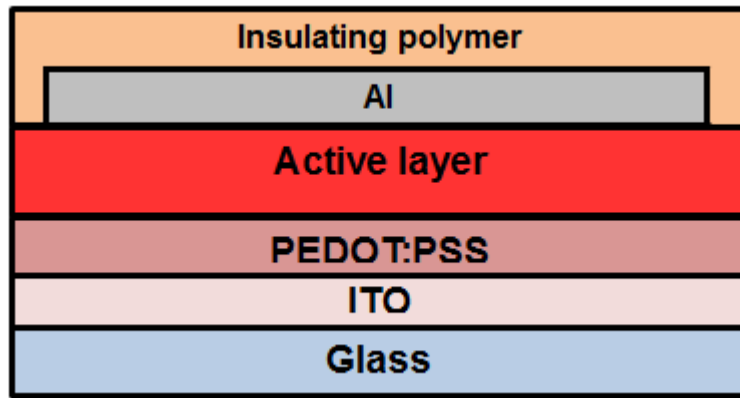


Figure 9.1. Schematic diagram illustrating the structure of laminated device.

It was found that the production of a uniform layer of insulating polymer on the surface of the device was not trivial. Because the lamination in this study was achieved using solution processing. There was a high probability that the insulating polymer would diffuse into the active layer, leading to very poor performance. The problem that was faced at the beginning of these experiments was how to coat the surface of the device with the insulating polymer and minimize the impact on the active layer. Initial experiments used a solution of PEG polymer. The viscosity of the solution was high so that when it was spin cast at 800 rpm, the solution did not spread across the surface of the substrate and became concentrated over the middle of the devices, causing penetration into the active layer. Therefore, multiple different methods were used to laminate 28 devices. Four devices were prepared using each method. The methods and the average efficiencies of the laminated devices are listed in Table 9.1.

Table 9.1 The average PCE obtained using various methods for lamination with PEG polymer.

Method of lamination	PCE (%)
Control-No lamination	0.96 ± 0.04
Painted onto the surface with a brush	0.22 ± 0.06
Spin at 800 rpm	0.06 ± 0.08
Spin at 1000 rpm	0.37 ± 0.02
Spin at 1300 rpm	0.80 ± 0.03
Spin at 1500 rpm	0.36 ± 0.07
Drop solution during spin at 1500 rpm	0.23 ± 0.05
Spin at 1800 rpm	0.17 ± 0.07

It appears that a high spin speed did not produce a uniform layer on the surface of the devices, while a low speed allowed for penetration of the solution into the active layer. It seems that 1300 rpm was the optimum spinning rate for the production of a uniform film. Informed by this finding, three further sets of eight devices were manufactured, as follows: devices laminated with PEG polymer, devices laminated with PMMA polymer and a set of control devices without lamination. A comparison between the performances of these optimized devices is shown in Table 9.2.

Table 9. 2 The average performance of laminated devices.

Device	V_{oc} (V)	J_{sc} (mA/cm ²)	FF (%)	PCE (%)
Control	0.41 ± 0.01	3.9 ± 0.2	52 ± 2	0.85 ± 0.05
Laminated with PMMA	0.41 ± 0.01	3.0 ± 0.4	50 ± 1	0.62 ± 0.09
Laminated with PEG	0.35 ± 0.01	3.8 ± 0.5	50 ± 2	0.67 ± 0.09

The power conversion efficiency of fresh laminated devices was less than that of the control devices by ~20%. It was observed that lamination with PMMA reduced the J_{sc} , while lamination with PEG reduced the V_{oc} although the PCE remained approximately the same. For PMMA devices, a PCE of 0.62% was recorded, whereas devices laminated with PEG showed a PCE of 0.67%. These results demonstrate that this method of lamination caused a slight but not significant reduction in the initial performance when compared with the initial values of control devices.

9.3 Film morphology of the cathode

The surface of the lamination on top of the metal electrode was imaged using AFM. Figure 9.2 shows the surface above the Al for control devices and devices laminated with PMMA and PEG. The roughness values extracted from the topographic images show that the PMMA layer has a low roughness (1.63 nm) compared to the PEG layer (3.58 nm) and the surface of the bare Al (5.96 nm). The phase image of the non-laminated device (Figure 9.3 (b)) shows less phase contrast than PMMA and PEG

layers, while the phase image of the laminated devices with PMMA and PEG (Figure 9.3 (d & f)) reveals the existence of more than one phase on the surface.

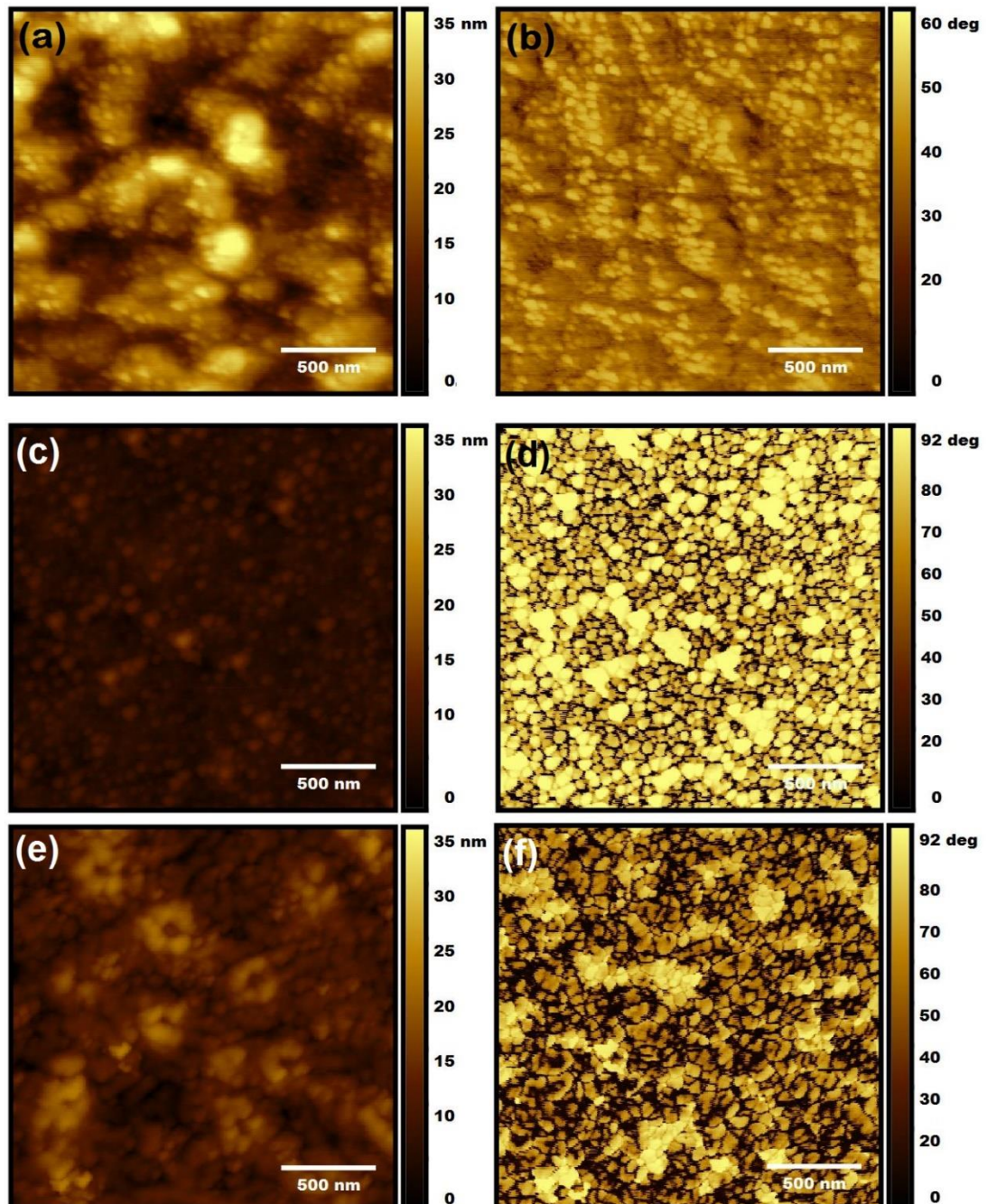


Figure 9.2. AFM topography (left column) and phase images (right column), showing the morphology of the top surface of the device for: ((a) and (b)) a non-laminated device, ((c) and (d)) a device laminated with PMMA, and ((e) and (f)) a device laminated with PEG.

These images are typical of PMMA and PEG [4], suggesting that in both cases, the Al surface had been successfully coated with the insulating polymer. The different phases apparent in the phase images may be attributed to the segregation of low and high molecular weights of the polymers. The distribution of the polymer chains on the surface might form the bright and dark areas [4].

9.4 Effect of lamination on device lifetime

The lamination process did not significantly diminish the electrical properties of the device and similar performance, compared to un-laminated devices. Therefore, all of the 24 devices were stored in a 1% RH environment, and their performance was monitored as a function of time. Figure 9.3 shows a graph of average power conversion efficiency versus time for these devices.

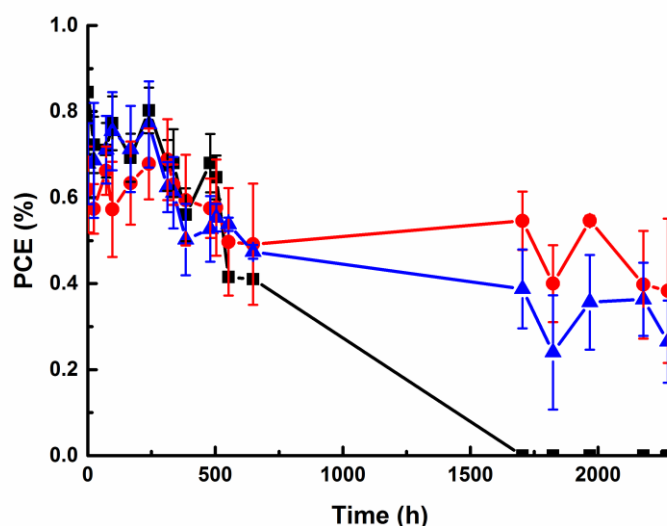


Figure 9.3. Power conversion efficiency as a function of time for control devices (black squares), devices laminated with PMMA (red circles) and devices laminated with PEG (blue triangles).

The data revealed that the lamination process significantly increased the lifetime of the devices (T_{20}) to more than 2000 h, while the control devices did not show any measurable PV behavior after 1500 h. In fact, the lifetime of control devices obtained from previous experiments (Chapter 5, 6, and 7) is usually less than 700 h. Many studies have reported on the diffusion of water and oxygen through the cathode, oxidizing the Al and forming an insulating layer at the interface with the active layer [1] [5]. The improvement in the lifetime of laminated devices may be due to the ability of the insulating polymer to protect the device from the diffusion of water and oxygen and prevent the formation of a thick oxidized layer at the Al/active layer interface.

9.5 Comparison between ternary blend and laminated devices

An enhancement in OPV lifetime was achieved by adding the insulating polymer to the active layer (ternary device) or by adding a layer of insulating polymer to the top of a completed stack (laminated device). However, it is not clear which process leads to maximum lifetime enhancement. A comparison was carried out to quantify the impact of the ternary and lamination processes on device lifetime. Four different sets of 12 devices were fabricated, as described in section 4.3. The sets were categorized as follows: binary (control) devices, ternary devices, laminated devices, and ternary-laminated devices (combination of the ternary and lamination processes). The devices were blended and laminated using PMMA because, in previous experiments, this material

showed better performance than PEG. All of the devices were stored in a 50% RH environment to test their ability to resist water and oxygen.

Figure 9.4 compares the degradation behavior of the average electrical parameters for all four sets of devices, as a function of time.

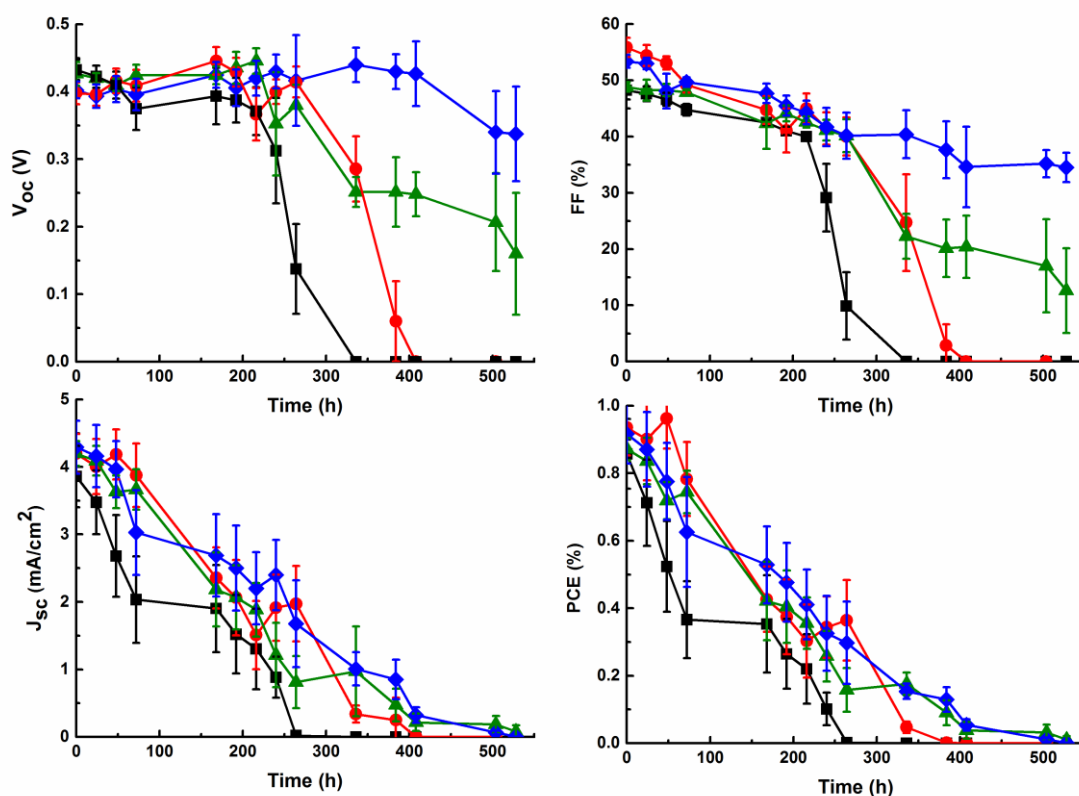


Figure 9.4. The electrical parameters, V_{oc} , FF, J_{sc} and PCE, as a function of time, for binary devices (black squares), ternary devices (red circles), laminated devices (green triangles), and ternary - laminated devices (blue diamonds).

The binary devices exhibited a lifetime (T_{20}) of ~ 220 h compared to ~ 330 h obtained for ternary devices. Furthermore, the lifetime of laminated devices was increased to more than 350 h, while the ternary-laminated devices yielded a lifetime similar to the laminated devices, although their FF and V_{oc} were more stable than laminated devices. The

increase in the lifetime of the laminated and ternary-laminated devices compared to the binary and ternary devices was due to the comparative stability of V_{oc} and FF. This finding suggests that changes at the cathode may be the origin of the degradation in V_{oc} and FF. However, the major reason for degradation in all of the devices was a reduction of J_{sc} .

It appears that the PMMA lamination acts as a protective layer that inhibits the diffusion of oxygen and water into the device through the cathode. The PMMA in ternary devices was found to be at the PEDOT: PSS/active layer interface, perhaps suggesting that the PMMA in ternary blend devices protects the active layer from water diffusing through the PEDOT: PSS. The data presented here suggest that the main cause of degradation is the cathode rather than the PEDOT: PSS. This is in agreement with the conclusions of Voroshazi et al.[1], who reported that oxidation of the cathode is the primary reason for degradation, not the PEDOT: PSS. However, the hygroscopic nature of PEDOT: PSS greatly accelerates cathode oxidation.

9.6 The effect of humidity on the electrical parameters of the ternary and laminated devices

Further understanding of the degradation behavior was obtained by comparing the electrical parameters of aged binary, ternary, and laminated devices in 1% RH and 50% RH. The electrical parameters (V_{oc} , FF, J_{sc}) of laminated and ternary devices based on PMMA were normalized to their initial values.

Figure 9.5 shows the degradation behavior of laminated and ternary devices compared with binary devices in 50% RH and 1% RH.

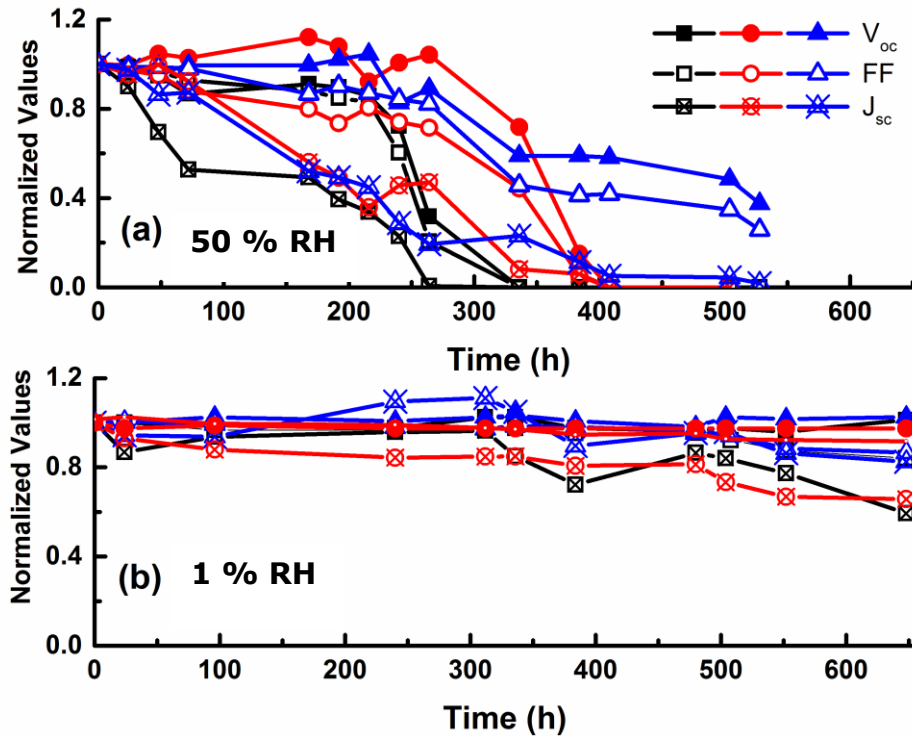


Figure 9.5. Normalized average values of the fill factor, open circuit voltage, and short circuit current for a binary device (black squares), a ternary device (red circles), and a laminated device (blue triangles). (a) Devices stored in 50% RH, and (b) stored in 1% RH.

From Figure 9.5 (a), it is apparent that storage at a humidity level of 50% RH had a significant effect on all of the parameters in binary devices. When PMMA was added to P3HT:PCBM (ternary devices), the FF and V_{oc} decreased slower than in binary devices, while these parameters were more stable in the laminated devices than in binary and ternary devices. This indicates that the protection of the cathode from water and oxygen can improve the stability of V_{oc} and FF. However, J_{sc} continued to

decline, and the same rate of degradation was observed in all of the devices.

At 1% RH, the FF and V_{oc} become more stable in all of the devices (Figure 9.5 (b)), indicating that water is the major reason for the degradation in V_{oc} and FF in these devices. However, for the duration of the experiment, J_{sc} degraded in both ternary and binary devices, while it remained almost unaffected in the laminated devices. This behavior means that reducing the humidity and protecting the cathode could minimize degradation in J_{sc} . This indicates that J_{sc} is not just degraded by the presence of water, but that there is an additional degradation mechanism present. Since the lamination process not only protects the device from the diffusion of water but also from oxygen, this may be the reason for the small degradation of J_{sc} . This finding is consistent with a study by Schafferhans et al. [6], who also observed a decrease in J_{sc} , while FF and V_{oc} remained constant when their P3HT: PCBM devices were exposed to oxygen in the dark. This study concluded that doping by oxygen was the origin of the observed decrease in J_{sc} . The doping increased the probability of the formation of additional traps and consequently, enhanced the chances of recombination [6].

9.7 The effect of humidity on the cathode

Humidity caused a reduction in J_{sc} , as well as FF and V_{oc} . To observe the effect of water on these devices, fresh binary and ternary devices were placed in a very high humidity environment (85% RH). After storage at 85% RH for one hour, the formation of black spots on

the surface of the Al electrode was observed. The black spots were denser on the binary devices than on their ternary counterparts. Optical micrographs of these features on the surface of (a) a binary device and (b) a ternary device were taken in three different areas, and typical images are shown in Figure 9.6. It is important to note that before the devices were placed in the high humidity environment, no dots were observed on either device.

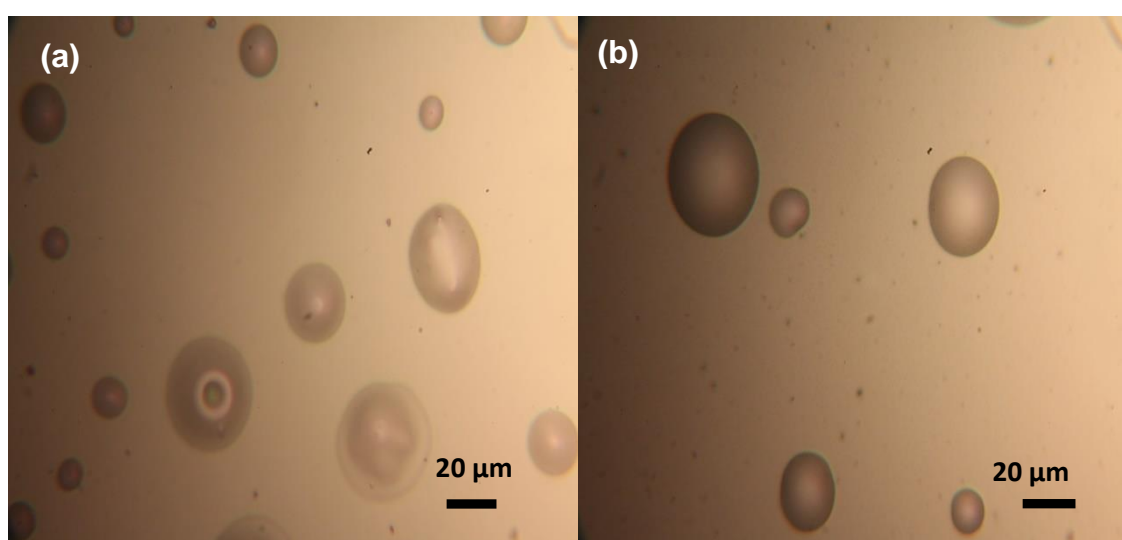
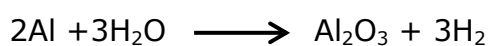


Figure 9.6. Bubbles on the surface of the Al cathode of: (a) a binary device, and (b) a ternary device, as a result of storage in a high humidity environment for 1 hour.

This finding indicates that high humidity accelerates the formation of bubbles and the ternary devices reduce them. Similar types of bubbles were also observed by Luo et al. [7], who demonstrated that the bubbles in the electrode were caused by PEDOT: PSS. They found that no bubbles were formed in the Al electrode without PEDOT: PSS. They suggested that the hygroscopic nature of PEDOT: PSS lead to the absorption of water and oxidation of the organic material, resulting in the creation of

gases such as O₂ and CO₂, which can delaminate the Al electrode, forming bubbles [7][8]. Moreover, water can also diffuse through the cathode to the Al/polymer interface [2] leading to the formation of Al₂O₃, with the evolution of H₂ [9]:



It was concluded from this result that water causes chemical degradation in the active layer and the Al cathode, causing delamination of the metal electrode and leading to reduced efficiency of charge collection and device lifetime. It appears that PMMA in ternary devices reduces the density of bubbles on the Al surface, due to its ability to absorb water diffusing from the PEDOT: PSS layer. Use of the lamination process would reduce the diffusion of water into the device through the metal electrode which could also reduce the formation of the Al₂O₃ layer. Therefore, using a ternary blend active layer with lamination, as illustrated schematically in Figure 9.7, reduces degradation in the FF and V_{oc} which in turn enhances the device lifetime.

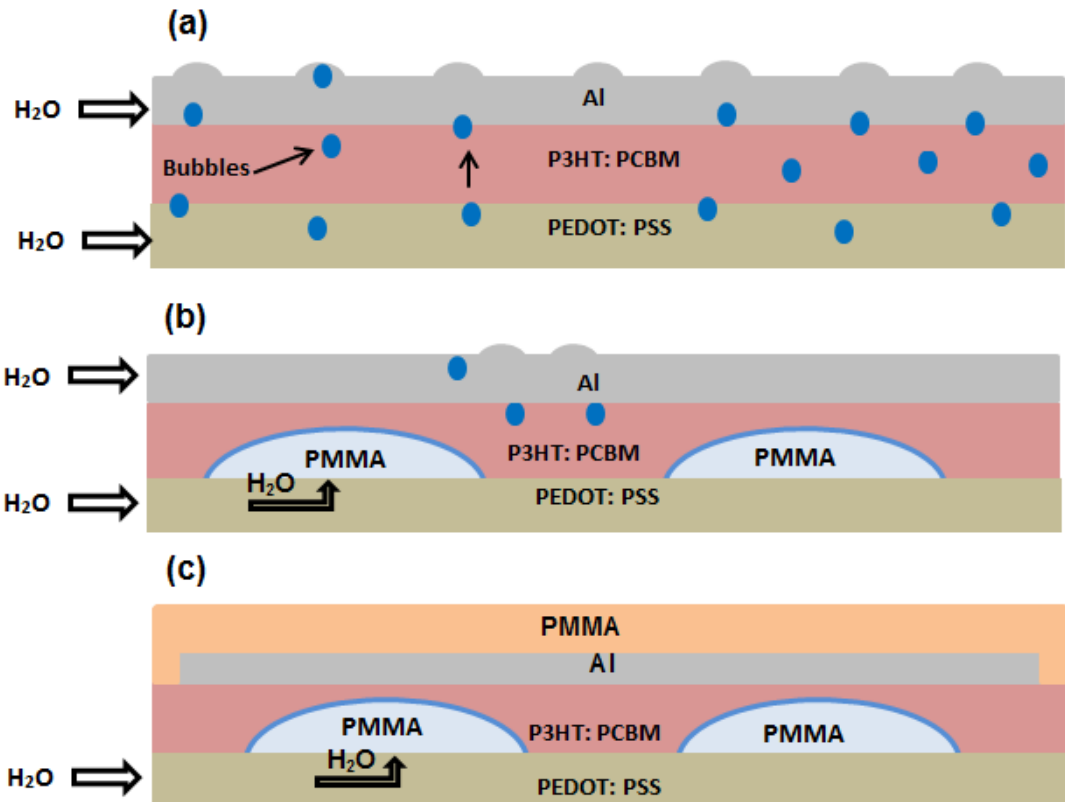


Figure 9.7. Schematic diagram illustrating the effect of gas bubble formation in (a) a binary device, (b) a ternary device, and (c) a dual device.

9.8 Conclusion

This chapter has shown that the lamination process does not significantly diminish the electrical properties of these devices as it causes only a slight reduction in the efficiency. Laminated devices exhibited enhanced lifetime relative to ternary devices, while applying lamination to ternary devices enhanced the electrical parameters (FF and V_{oc}) more than using the two methods separately. In addition, in laminated devices, the FF and V_{oc} decreased more slowly than in ternary devices when they were stored under 50% RH, while in 1% RH the laminated devices were more stable than ternary devices.

It was concluded that water causes chemical degradation, leading to deterioration in the V_{oc} and FF. However, oxygen may cause an electronic degradation in the devices by forming additional traps, leading to a reduction in the J_{sc} . The presence of both water and oxygen caused degradation in all the parameters. Using lamination on a ternary blend device might reduce the diffusion of water and oxygen from both electrodes, enhancing the lifetime of the devices.

9.9 References

- [1] E. Voroshazi, B. Verreet, A. Buri, R. Müller, D. Di Nuzzo, and P. Heremans, "Influence of cathode oxidation via the hole extraction layer in polymer: fullerene solar cells," *Org. Electron.*, vol. 12, no. 5, pp. 736–744, 2011.
- [2] F. C. Krebs, and K. Norman, "Analysis of the failure mechanism for a stable organic photovoltaic during 10000 h of Testing," *Prog. Photovolt Res. Appl.*, vol. 15, pp. 697–712, 2007.
- [3] K. Kawano, R. Pacios, D. Poplavskyy, J. Nelson, D. D. C. Bradley, and J. R. Durrant, "Degradation of organic solar cells due to air exposure," *Sol. Energy Mater. Sol. Cells*, vol. 90, no. 20, pp. 3520–3530, 2006.
- [4] L. Zhang, "Self-assembled intrinsic nanoscale phase separation in polymers," *EPL (Europhysics Lett)*., vol. 93, no. 2, pp. 28002–58002, 2011.
- [5] M. Wang, F. Xie, J. Du, Q. Tang, S. Zheng, Q. Miao, J. Chen, N. Zhao, and J. B. Xu, "Degradation mechanism of organic solar cells with aluminum cathode," *Sol. Energy Mater. Sol. Cells*, vol. 95, no. 12, pp. 3303–3310, 2011.
- [6] J. Schafferhans, A. Baumann, A. Wagenpfahl, C. Deibel, and D. Vladimir, "Oxygen doping of P3HT: PCBM blends: Influence on trap states, charge carrier mobility and solar cell performance," *Org.*

Electron., vol 11, pp. 1693–1700, 2010.

- [7] S. C. Luo, H. H. Chung, E. T. Pashuck, E. P. Douglas, and P. H. Holloway, "Formation of bubbles on electrical contacts to polymer light-emitting diode devices," *Thin Solid Films*, vol. 478, no. 1–2, pp. 326–331, 2005.

- [8] S. Karak, S. Pradhan, and A. Dhar, "The effects of different atmospheric conditions on device stability of organic small-molecule solar cells under constant illumination," *Semicond. Sci. Technol.*, vol. 26, p. 095020, 2011.

- [9] L.-M. Do, M. Oyamada, A. Koike, E.-M. Han, N. Yamamoto, and M. Fujihira, "Morphological change in the degradation of Al electrode surfaces of electroluminescent devices by fluorescence microscopy and AFM," *Thin Solid Films*, vol. 273, no. 1–2, pp. 209–213, 1996.

CHAPTER 10

CONCLUSIONS AND SUGGESTIONS FOR FURTHER WORK

10.1 Conclusions

The continued progress in the power conversion efficiency of OPVs has made them competitive with other thin film PV technologies. Improving the lifetime of OPVs is a serious issue that has to be solved. In particular, the degradation processes are still not fully understood. This thesis has attempted to understand the degradation mechanisms and show methods to increase the lifetime of OPVs based on P3HT: PCBM. These are focused on blending insulating polymers with the active materials and laminating the devices with insulating polymers. The key results of this study are summarized below.

The thesis began by investigating the effect of different environments on the lifetime of OPV devices without further additives. The devices were stored in ambient and inert environments. The results revealed that water and oxygen from the environment are the primary causes of degradation. However, FTIR spectroscopy did not show any visible chemical degradation in P3HT or PCBM.

To slow the degradation resulting from the diffusion of water and oxygen, PMMA was added to P3HT: PCBM. The results showed that the

PMMA not only improved the lifetime but also enhanced the performance of the devices. SEM images illustrated that PMMA forms dome-like shapes underneath the active layer. The results also revealed that PMMA increased the device lifetime as relative humidity decreased. This finding suggested that PMMA acts as a water gettering agent, For example, PMMA slows the process of degradation by absorption of water. To investigate this idea, two different insulating polymers were used in ternary devices. a-PS has less ability to absorb water, and PEG has a greater ability to absorb water than PMMA.

The experiments showed that a-PS did not enhance the lifetime of OPV devices. It was found that binary and ternary devices degraded at the same rate in high and low humidity environments. In contrast, PEG slowed the degradation more than binary and ternary devices containing PMMA. The T_{20} of PEG devices was 192 h vs. 120 h for binary devices while the T_{20} of PMMA devices was 168 h vs. 120 h for binary devices, stored in 50% RH. Although the PEG polymer enhanced the lifetime of the devices more than other polymers, the OPV performance was the lowest. AFM images indicated that PEG induced an unfavorable morphology, leading to an increase in the series resistance and decrease in the FF.

Further analysis for ternary devices containing PMMA was carried out in Chapter 8. The SCLC method was used in an attempt to measure the hole mobility of ternary and binary devices as a function of aging time. The primary results showed that hole current increased with time up to a saturation value in both types of devices. Two possible reasons

were ruled out as the cause of this behaviour, namely the humidity of the environment and the metal contact. The mechanism proposed to explain the increase in hole current was instead oxygen doping. It was suggested that the diffusion of oxygen into the device resulted in the formation of a charge-transfer complex with the P3HT polymer, which may be responsible for the generation of charge carriers in the devices. The trap free SCLC region was not observed within the range of the voltage measured for aged devices, making it inappropriate to estimate the hole mobility.

Finally, laminated devices with insulating polymers of PMMA and PEG were fabricated. The results of Chapter 9 revealed that laminating the devices with insulating polymers has a small detrimental effect on the initial device performance. The lamination process was applied to both binary and ternary devices. It was shown that applying lamination to the ternary devices enhanced the electrical parameters (FF and V_{oc}) more than applying this method to the binary devices. When comparing between the lamination and ternary devices, it was found that the lamination process stabilized the FF and V_{oc} more than the ternary devices in 50% RH, while in 1% RH the lamination process stabilized all the device parameters more than ternary devices.

It was concluded that water caused chemical degradation leading to deterioration in the V_{oc} and FF. However, oxygen may cause electronic degradation in the device by forming additional traps, leading to a reduction in the J_{sc} . It also was observed from Chapter 8, that conductivity has not been affected by water, which suggests that oxygen

may be the reason for changing the electronic properties of OPVs. The presence of both water and oxygen caused degradation in all the parameters. Using lamination on a ternary blend device might reduce the diffusion of water and oxygen from both electrodes, enhancing the lifetime of OPVs.

10.2 Suggestions for further work

Studying the degradation of organic photovoltaics opens up many different issues to explore. A few suggestions for future work are explained below.

(a) Water induced chemical degradation

It has been reported that water could cause chemical degradation inside the active layer and at cathode/ active layer interface [1][2][3]. However, this chemical degradation was not observed in our devices. This may relate to the limitation of FTIR or due to storing the devices in the dark during lifetime measurements. Two further experiments may help to understand the water induced degradation mechanisms. The first study is comparing the degradation between the devices stored in light and dark to investigate whether light accelerates chemical degradation. The second suggestion is to use two different techniques that may give more information about the chemical changes in the OPVs. These techniques are time-of-flight secondary ion mass spectrometry (TOF-SIMS) and X-ray photoelectron spectroscopy (XPS). The first experiment can provide chemical information from all the layers of OPV devices while the second

approach can be used to observe the chemical changes that may occur at the Al/active layer interface [4].

(b) Investigating the effect of morphology on the lifetime of ternary devices

The results of ternary devices containing PEG molecules are promising for enhancing the lifetime of OPVs. However, the unfavorable morphology that PEG produced led to poorer performance. One approach that could alter the morphology is by changing the molecular weight of the polymer. It would be interesting to vary the molecular weight of the insulating polymers and compare the performance and lifetime of different resultant morphologies to identify which morphology gives better performance and longer lifetime.

10.3 References

- [1] K. Norrman, S. A. Gevorgyan, and F. C. Krebs, "Water-induced degradation of polymer solar cells studied by H 2 18 O labeling," *ACS Appl. Mater. Interfaces*, vol. 1, no. 1, pp. 102–112, 2009.
- [2] A. Rivaton, S. Chambon, M. Manceau, J.-L. Gardette, N. Lemaître, and S. Guillerez, "Light-induced degradation of the active layer of polymer-based solar cells," *Polym. Degrad. Stab.*, vol. 95, no. 3, pp. 278–284, 2010.
- [3] M. Jørgensen, K. Norrman, S. A. Gevorgyan, T. Tromholt, B. Andreasen, and F. C. Krebs, "Stability of polymer solar cells," *Adv. Mater.*, vol. 24, no. 5, pp. 580–612, 2012.
- [4] M. Hermenau, M. Riede, K. Leo, S. A. Gevorgyan, F. C. Krebs, and K. Norrman, "Water and oxygen induced degradation of small molecule organic solar cells," *Sol. Energy Mater. Sol. Cells*, vol. 95, no. 5, pp. 1268–1277, 2011.